

THESIS

FLOW FIELD AT OPEN-CHANNEL CONTRACTIONS: INSIGHTS FROM A TWO-
DIMENSIONAL NUMERICAL MODEL

Submitted by

Scott S. Zey

Department of Civil and Environmental Engineering

In partial fulfillment of the requirements

For the Degree of Master of Science

Colorado State University

Fort Collins, Colorado

Fall 2017

Master's Committee:

Advisor: Robert Ettema

Peter A. Nelson

Timothy P. Covino

Copyright by Scott S. Zey 2017

All Rights Reserved

ABSTRACT

FLOW FIELD AT OPEN-CHANNEL CONTRACTIONS: INSIGHTS FROM A TWO-DIMENSIONAL NUMERICAL MODEL

A depth averaged, two-dimensional numerical model was used to investigate the hydraulics of flow passing through open-channel contractions. The investigation focused on the magnitude and location(s) of maximum velocity of flow entering a contraction. The effective flow width at the entrance of the contraction and the maximum lateral velocity at the contraction entrance were also investigated. The responses of these flow characteristics were studied as values of contraction ratio, channel roughness, bed slope, and transition geometry were varied. The numerical model produced significant new insights. The factors affecting the values and distribution of velocity in a contraction include: channel slope, bed roughness, and contraction shape. The magnitude and location of maximum velocity in the contraction varies with contraction ratio. For contraction ratios milder than approximately 0.5 the velocity maximum occurs at two locations, and at one location for tighter contractions. At a contraction ratio of 0.5 lateral velocity reached a maximum and effective flow width a minimum. Channel slope and bed roughness affect the values and distribution of velocity in a contraction, as did contraction shape. These findings have engineering significance for explaining and estimating scour of alluvial channels in contractions, such as at bridge waterways.

ACKNOWLEDGEMENTS

I would like to thank Robert Ettema, William deRosset, and Paul Clopper for their tireless guidance and interest in my studies.

DEDICATION

This work is dedicated to my wife and source of constant support, Jaclyn Zey. Without her, none of this would be possible.

TABLE OF CONTENTS

ABSTRACT.....	II
ACKNOWLEDGEMENTS.....	III
DEDICATION.....	IV
TABLE OF CONTENTS.....	V
LIST OF TABLES.....	VIII
LIST OF FIGURES.....	IX
1. INTRODUCTION.....	1
2. BACKGROUND.....	4
2.1. CONTRACTION HYDRAULICS.....	4
2.2. IMPORTANT PARAMETERS.....	9
2.3. PRIOR LITERATURE.....	13
2.3.1. EXISTING BOOKS.....	13
2.3.2. NUMERICAL MODELS.....	15
3. EXPERIMENTAL PROCEDURE.....	20
3.1. ASSUMPTIONS AND SIMPLIFICATIONS.....	20
3.2. DESCRIPTION OF NUMERICAL MODEL.....	21
3.3. MODEL SETUP.....	22
3.4. MODEL SIMULATION CONFIGURATION.....	23
3.5. EXPERIMENTAL PROGRAM.....	24
3.6. BOUNDARY SENSITIVITY ANALYSIS.....	27
3.7. SIMULATION DURATION SENSITIVITY ANALYSIS.....	28

3.8.	DATA COLLECTION AND ANALYSIS	28
4.	RESULTS FROM THE MODEL.....	33
4.1.	VARIATION IN LOCATION OF PEAK VELOCITY	36
4.1.1.	INFLUENCE OF CONTRACTION RATIO OF PEAK VELOCITY LOCATION 37	
4.1.2.	INFLUENCE OF TRANSITION SHAPE ON VELOCITY LOCATION	38
4.2.	VARIATION IN VELOCITY UNIFORMITY	40
4.2.1.	INFLUENCE OF CONTRACTION RATIO OF VELOCITY UNIFORMITY	41
4.2.2.	INFLUENCE OF BED ROUGHNESS ON VELOCITY UNIFORMITY	44
4.2.3.	INFLUENCE OF SLOPE ON VELOCITY UNIFORMITY	46
4.2.4.	INFLUENCE OF TRANSITION SHAPE ON VELOCITY UNIFORMITY	47
4.3.	VARIATION IN VELOCITY AMPLIFICATION	49
4.3.1.	INFLUENCE OF CONTRACTION RATIO ON VELOCITY AMPLIFICATION 49	
4.3.2.	INFLUENCE OF BED ROUGHNESS ON VELOCITY AMPLIFICATION	51
4.3.3.	INFLUENCE OF SLOPE ON VELOCITY AMPLIFICATION	53
4.3.4.	INFLUENCE OF TRANSITION SHAPE ON VELOCITY AMPLIFICATION..	54
4.4.	VARIATION IN FLOW SEPARATION	55
4.4.1.	INFLUENCE OF CONTRACTION RATIO ON FLOW SEPARATION	56
4.4.2.	INFLUENCE OF BED ROUGHNESS ON FLOW SEPARATION	58
4.4.3.	INFLUENCE OF SLOPE ON FLOW SEPARATION	60
4.4.4.	INFLUENCE OF TRANSITION SHAPE ON FLOW SEPARATION	62
5.	CONCLUSIONS AND RECOMENDATIONS	63

5.1. CONCLUSIONS.....	63
5.2. RECOMMENDATIONS	65
REFERENCES	67
APPENDIX A: SIMULATION RESULTS, DATA SUMMARY TABLE.....	69
APPENDIX B: SIMULATION RESULTS VELOCITY MAGNITUDE PLOTS	70

LIST OF TABLES

Table 1: Independent variables considered when analyzing contraction hydraulics	11
Table 2: Experimental program	25
Table 3: Definitions of Simulation Result Variables	33

LIST OF FIGURES

Figure 1: Layout and basic variables	5
Figure 2: Specific energy diagrams	8
Figure 3: Contraction geometry schematic	10
Figure 4: Calculated instantaneous 3D particle trajectories	16
Figure 5: Representation of coherent structures around abutments (Koken, 2017);	18
Figure 6: Example model mesh.	23
Figure 7: Schematic of the contraction-transition geometries simulated.....	26
Figure 8: Downstream boundary sensitivity analysis	27
Figure 9: Example velocity magnitude results map.....	29
Figure 10: Example of recirculating flow separation vector map,.....	30
Figure 11: Example of non-recirculating flow separation vector map	30
Figure 12: Example depth and velocity centerline profile.....	31
Figure 13: Example depth and longitudinal velocity cross-section	32
Figure 14: Maximum velocity location schematic.....	34
Figure 15: Minimum effective flow width dimension schematic	36
Figure 16: Velocity plots showing changes of maximum velocity location.....	37
Figure 17: Longitudinal location of maximum velocity versus contraction ratio	38
Figure 18: Velocity plots with varying transition shapes	39
Figure 19: Lateral location of maximum velocity versus contraction ratio,with varying transition shape	40
Figure 20: Velocity uniformity, V_{max} / V_{max} versus contraction ratio.....	41

Figure 21: Experiment set 1, velocity plots	43
Figure 22: Coefficient of velocity variation at the cross-section of maximum velocity.....	44
Figure 23: Velocity uniformity versus contraction ratio with varying roughness	45
Figure 24: Velocity uniformity versus contraction ratio with varying slope.....	46
Figure 25: Velocity cross-sections with varying slope at a contraction ratio, W_2/W_1 , of 0.5	47
Figure 26: Velocity uniformity versus contraction ratio with varying transition shape	48
Figure 28: Velocity amplification versus contraction ratio, experiment set 1	50
Figure 29: Velocity amplification vs contraction ratio with varying roughness	52
Figure 30: Velocity amplification versus contraction ratio with varying slope.....	53
Figure 31: Velocity amplification versus contraction ratio with varying transition shape.....	55
Figure 32: Effective flow width versus contraction ratio, for experiment set 1	57
Figure 33: Maximum lateral velocity versus contraction ratio, for experiment set 1	58
Figure 34: Effective flow width versus contraction ratio, with varying roughness.....	59
Figure 35: Maximum lateral velocity versus contraction ratio, with varying roughness	60
Figure 36: Effective flow width versus contraction ratio, with varying slope.....	61
Figure 37: Maximum lateral velocity versus contraction ratio, with varying slope	61
Figure 38: Maximum lateral velocity versus contraction ratio, with varying transition shape	62

LIST OF SYMBOLS

Symbol	Definition
E	Specific energy head (m)
g	Acceleration of gravity (m/s^2)
g	Gravity Acceleration
k	Bed Roughness Height (m)
n	Manning's roughness coefficient
O	Lateral centerline offset (m)
S_0	Bed Slope
S_f	Friction Slope
V	Velocity (m/s)
\bar{V}	Cross-section average velocity
W	Channel width (m)
X	Longitudinal Distance (m)
Y	Flow Depth (m)
α	Angle of contraction transition
ν	Kinematic viscosity of water
ρ	Density of water (kg/m^3)

Subscript	Definition
1	Upstream (un-contracted)
2	Downstream (contracted)
$1'$	Upstream at contraction
$2'$	Downstream at expansion
3	Downstream past expansion
max	Maximum velocity
lat	Maximum lateral velocity
e	Effective

1. INTRODUCTION

This study used a two-dimensional numerical model to gain insights into flow-field characteristics at open-channel contractions, such as at bridge waterways. Velocity amplification and flow separation near the contraction were of primary interest, especially in terms of providing diagnostic insight into contraction scour development at bridge waterways. These flow-field characteristics were determined in response to variations of channel width ratio, transition shape, channel slope, and bed roughness.

Narrowing of an open-channel occurs commonly and for a variety of reasons. A contraction results in a change of flow velocity, a change of flow depth, and an energy loss due to the lateral redirection of a portion of the flow. A one-dimensional (1D) model using the standard-step energy method, along with an assumed energy loss coefficient, provides a relatively simple method of analyzing a contraction. However, a one-dimensional context neglects several significant flow field characteristics of interest regarding flow through a contraction. Notably, for example, it does not give the information required for diagnostically explaining the development of contraction scour or predicting scour depth.

Spatial variation of velocity and, therefore, flow depth can be easily observed at the transition into a simple contraction in a flume or at a bridge or culvert opening. However, the characteristics of the magnitude and location of peak velocity in the contraction are unable to be accounted for with one-dimensional analysis. Without an understanding of how flow is distributed across the channel width, scour is difficult to predict and scour countermeasures must

be designed from observational experience rather than an understanding of contraction flow hydraulics.

Another neglected flow characteristic is flow separation, which usually occurs at the region where the approach channel narrows abruptly. Flow separation presents itself as an area of extreme velocity gradient and associated formation of large-scale turbulence structures often termed separation eddies. Flow outside the area of separation accelerates, while water within the separation area may rotate in a slow-moving, relatively quiescent, wake eddy marked by separation vortices at its boundary within the contracted flow. These pockets of quiescent flow area are common, and can be observed inside the throat of channel contractions either in the lab or the field. These flow separations effectively compound the channel constriction by further narrowing the width of effective flow.

Velocity variation and flow separation are two, often significant, flow field features that cannot be handled with traditional 1D numerical models. While three-dimensional (3D) modeling efforts have sought to resolve these complex flow features (e.g., Chrisohoides et al. 2003; Kara, 2015; Koken 2017), such modeling efforts remain out of reach to the average design engineer. However, two-dimensional (2D) models have recently become a practical design solution, and are commonly used in hydraulic engineering design. 2D models present an opportunity to investigate how the two flow features, flow acceleration and flow separation, vary with changing geometry of a contraction.

A practical reason to investigate contraction hydraulics is in the context of evaluating scour. The current state of contraction scour analysis is based upon Laursen's 1960 and 1963 formulations (FHWA 2012, Laursen 1960, Laursen 1963), which use a 1D formulation of flow through a contraction. These days, 2D numerical models are increasingly capable of illuminating and quantifying the major flow features, about which information is often required for designing bridge waterways.

2. BACKGROUND

This chapter discusses the main aspects of contraction hydraulics associated with flow into and through an open-channel contraction. As most hydraulic formulations treat contraction flows as being one-dimensional, and do not directly determine energy loss as a flow passes through a contraction, dimensional analysis must be used in order to define parameters to describe flow distribution and characteristics in contractions. Accordingly, this chapter includes a section addressing such a dimensional analysis. Also in this chapter is a brief review of prior studies on flow in open-channel contractions. As the extant textbooks cover this topic well, at least in terms of one-dimensional formulations, the review focuses on recent numerical models of flow in open-channel contractions.

2.1. Contraction Hydraulics

Before proceeding, it is useful to briefly describe the hydraulics of flow through an open-channel contraction. The hydraulics involve unsteady open-channel flow and usefully explained using the specific energy diagram and a flow-resistance equation, such as Manning's equation. As flow passes through a contraction and enters a narrower channel, the resulting flow profile depends on the extent to which the contraction chokes the approach flow. The contraction forces the water level to rise at the contraction entrance, creating a backwater water-surface profile extending upstream of the entrance. The magnitude of choking or water-level rise varies from negligible to substantial, depending on the geometry of the contraction and the length of the contracted channel. Figure 1a & b illustrate a plan view of channel contraction and water-surface profile changes in flow to and through the contraction, respectively.

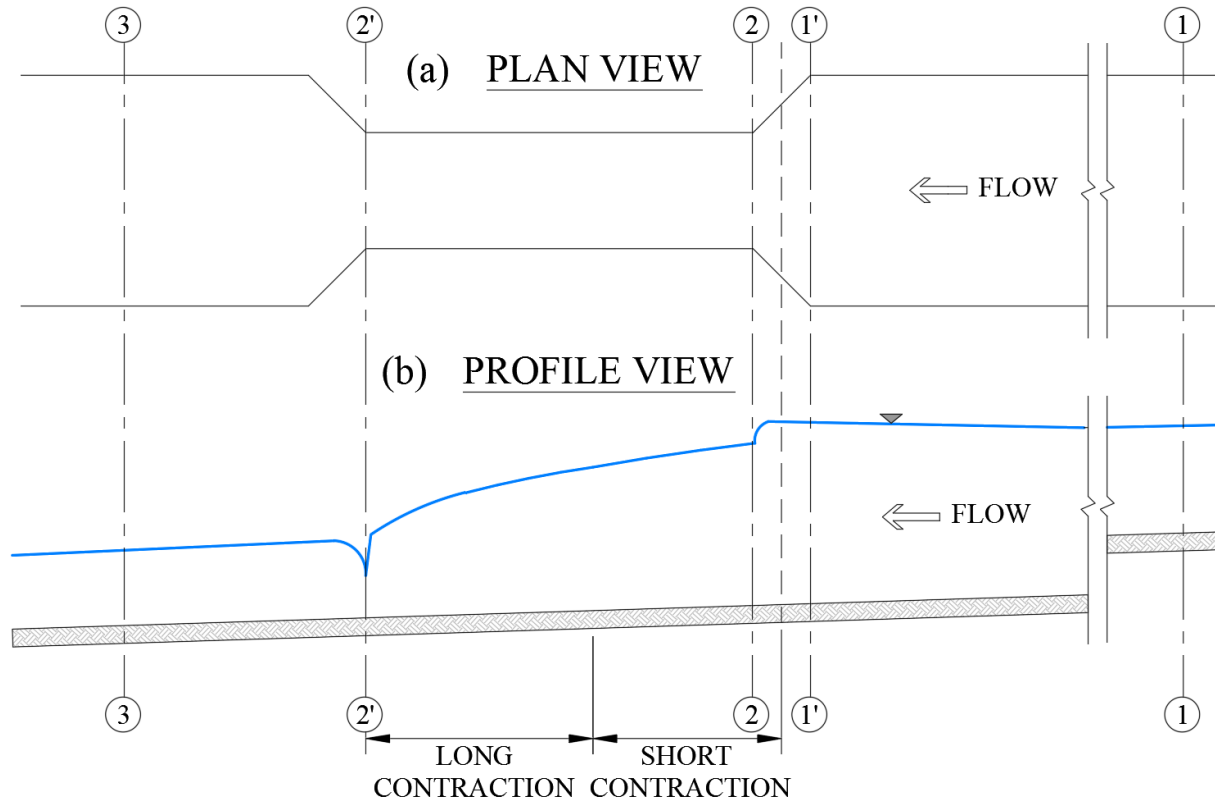


Figure 1: Layout and basic variables associated with flow through a contraction linking two widths of an open-channel. Note that for a very long, narrower channel, the flow depth tends to that channel's normal flow depth.

Also shown in Figure 1a&b are sub-regions often defined as the short-contraction region and the long-contraction region (e.g., Henderson 1966). While the short contraction region is present in all channel contractions, it is possible for both contraction regions to be present in a single contraction. Each region involves distinctive flow processes. Within the short contraction region accelerating velocities, changing flow depths, and large scale turbulence are dominant. However, more predictable gradually varying flow patterns dominate the long contraction region, which is located downstream of the short contraction region.

In Figure 1 the water surface decreases in elevation but increases in depth as it moves downstream from section 1 to section 1'. With a movable boundary, this condition is likely to alter rapidly as the bed begins to erode. The variation of flow depth and velocity through the different reaches of Figure 1 are accompanied by changes in specific energy. Specific energy, E , is defined as

$$E = Y + \frac{V^2}{2g} \quad \text{Eq. 2-1}$$

Values of E are measured vertically from the local invert or bed elevation of a channel.

For sub-critical flow, the usual flow condition at bridge waterways, the flow profiles are calculated from a known flow depth (e.g., normal flow depth) at the downstream end of the reach. However, for the present explanation it is more helpful to start by describing flow approaching the contraction and working downstream. Figure 1 shows the locations of sections 1, 1', 2, 2' and 3 to be considered in Figure 2a&b, which present specific energy diagrams and are useful aids for the following discussion:

- a) When the flow enters the narrower channel with slight choking (due to the additional, local energy loss associated with the contraction), which is normal for mild contractions (Figure 2), the depth of the approach flow, Y_1 , increases to Y'_1 , and the specific energy, E_1 , of the approach-flow increases to E_i . Note that unless the upstream flow is supercritical with an accompanying hydraulic jump, the water surface elevation will continue to decrease in the downstream direction while the flow depth increases. This increase is consumed as head loss as flow passes through the contraction and the rate of head loss due to boundary resistance increases. Flow velocity increases along the

contracted section where the flow is non-uniform and the energy gradient S_f exceeds the bed slope S_o .

- b) The flow depth moves along the path $1 \rightarrow 1' \rightarrow 2 \rightarrow 2'$, attaining specific energy E_2 as shown in Figure 2(a). The flow depth Y_2 cannot be sustained as normal flow, as the Manning's flow-resistance equation indicates; i.e.,

$$V = \frac{1}{n} Y_2^{2/3} S_f^{1/2}$$

- c) If the contraction were long enough, flow depth may eventually revert to normal flow depth, Y_2 as shown in Figure 2a. If the contraction were not long, flow along the contraction is non-uniform and a normal depth does not occur before the channel widens out again.
- d) Eventually, the flow transitions back into the wider channel. As it passes through the channel expansion, specific energy decreases due to the local loss of energy, and then asymptotes to the normal flow depth and associated specific energy at section 3.
- e) Should the contraction substantially choke the approach flow, then the approach flow backs up to attain the necessary magnitude of specific energy to pass through the contraction (Figure 2b). The specific energy at the entrance of the contraction, E_1' , equals E_1 plus the head loss for flow to pass through the contraction, with flow depth following path $1 \rightarrow 1'$ in Figure 2a. The flow passes into the contraction and pass through critical depth before a weak hydraulic jump forms early in the contracted channel. Consequently, specific energy decreases from E_2 to E_2' , as Figure 2b shows.

The proceeding discussion of one-dimensionally formulated contraction hydraulics reveals the non-uniform nature of flow through a contraction. It also indicates the limitations of such

formulations when used to estimate scour depth at contractions. The formulations comprising the basis of the contraction-scour equations recommended in HEC-18 (Arneson et al. 2012), notably, are based upon an idealized uniform flow condition in the contracted channel, which essentially yields such scour depth estimation approaches to be semi-empirical. In other words, they do not actually treat the non-uniform flow conditions associated with short-contraction scour and long contraction scour.

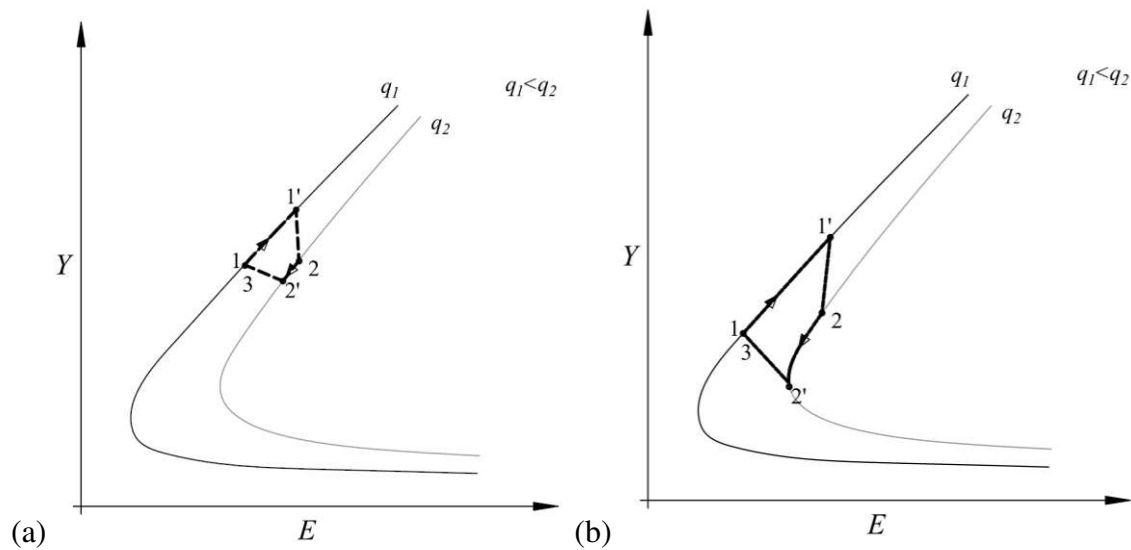


Figure 2: Specific energy diagrams showing change in flow depth as flow passes from a channel with unit discharge q_1 to a narrow channel with unit discharge q_2 where: (a) the contraction does not substantially choke the approach flow ; and, (b) the contraction substantially chokes the approach flow .

Furthermore, the current practices cannot begin to address the extra dimensions of non-uniformity that a 2D or 3D context would introduce. The existing formulations, like Arneson et al. (2012), for scour do not really relate scour depth the magnitude and location of maximum values of flow velocity and turbulence intensity within contractions.

2.2. Important Parameters

While the hydraulics of contraction flow can be solved using the governing equations for open-channel flow (notably the St. Venant equations commonly used to formulate open-channel flow), dimensional analysis provides a simple, and practical framework for identifying experimental variables, and defining the main processes. The following dimensional analysis aims at identifying the main parameters associated with the hydraulic characteristics of a contraction.

The uniform or (hydraulically) normal flow depths of open-channel flow downstream of a contraction is independent of the geometry of the contraction transition. However, flow depth through the short contraction segment is influenced by the geometry of the contraction and involves turbulent structures that may lead to laterally and longitudinally varied flow depth through the short contraction segment. This study provides insights into these flow features, as Chapter 4 elaborates.

For the purpose of this study and the following dimensional analysis, the sides of the open-channel are assumed to be relatively smooth, rectangular, and resistant to erosion. Flow through the channel is defined by a steady flow rate and a constant downstream water surface elevation. The channel bed consists of uniform material which is leveled to form a uniform bed slope. A 45° transition from the wider upstream segment to the narrower downstream segment forms the contraction transition. Figure 3 provides a schematic of the contraction configuration.

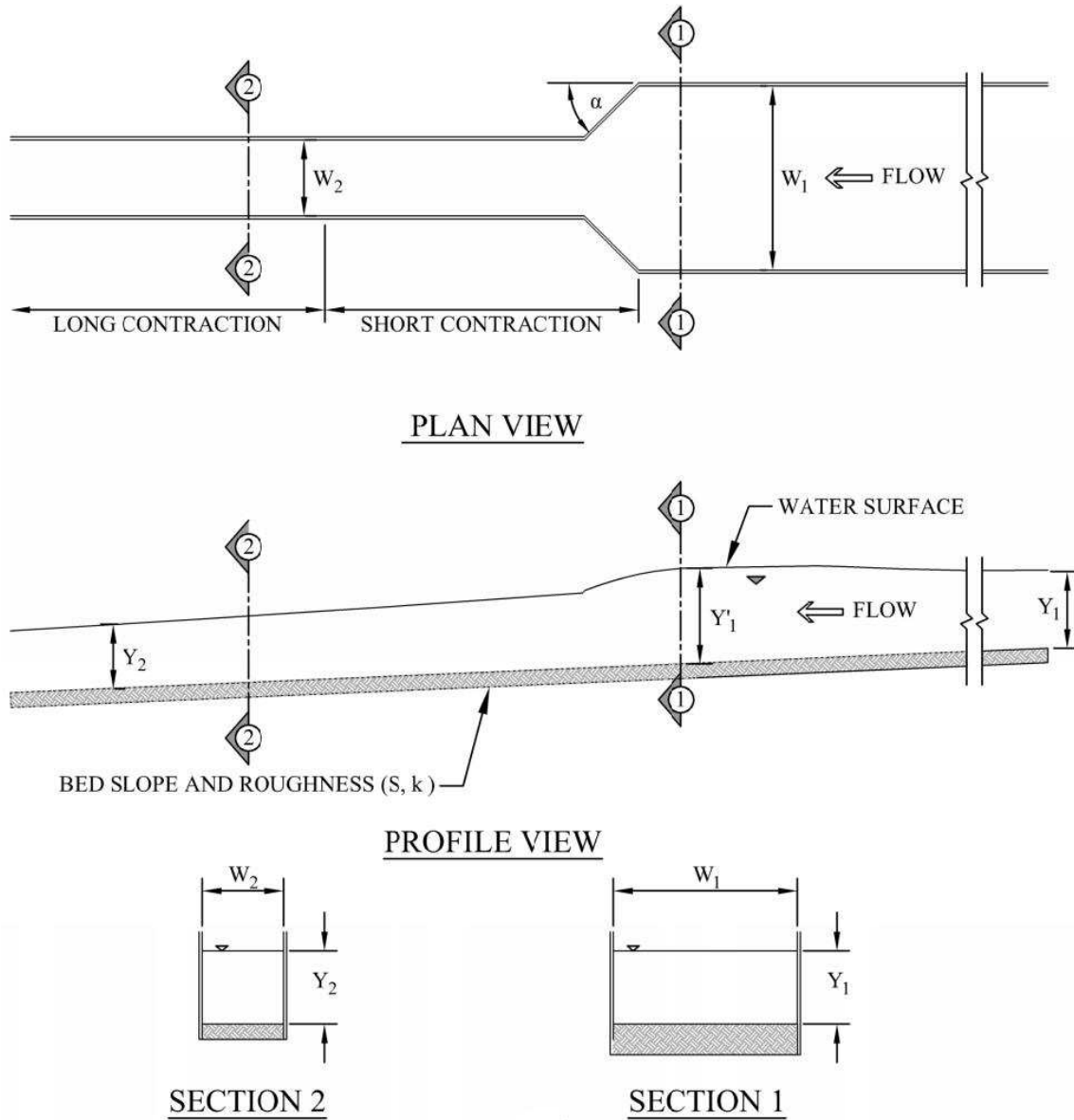


Figure 3: Contraction geometry schematic showing variables used in the dimensional analysis. Note that Y_1 and Y_2 are normal flow depths for sections 1 and 2.

The flow field characteristics of a contraction depend upon geometric, kinematic, and dynamic variables that can be written in terms of non-dimensional parameters that represent the effect of the variables upon the system. Table 1 provides a list of the independent variables considered here. Hydraulically normal flow depth is taken to occur at the downstream end of a long

contraction, assuming subcritical flow conditions, and it is independent of the hydraulic characteristics of flow occurring within the short contraction segment. Meanwhile, the hydraulics of flow within the short contraction affected by the channel characteristics and the downstream flow conditions. The following dimensional analysis considers the hydraulic characteristics within the short contraction, primarily velocity. Also, it includes the normal depth of flow at some distance downstream of the contraction.

Table 1: Independent variables considered when analyzing contraction hydraulics

Symbol	Variable
W_1	Approach (Upstream) Channel Width
W_2	Contracted (Downstream) Channel Width
α	Angle of Contraction Transition
V_2	Contracted Cross-Sectional Averaged Flow Velocity (Downstream)
Y_2	Contracted (Downstream) Normal Depth of Flow
S	Bed Slope
k	Bed Roughness Height
ρ	Density of Water
ν	Kinematic Viscosity of Water
g	Gravity Acceleration

The term “contraction hydraulics” can be broadly used to refer to many spatially varying variables within the short contraction segment. However, the variable of primary concern for the present study is the maximum velocity, V_{max} , within the short contraction and its specific location. It is possible to express V_{max} in terms of a functional relationship for water flow at constant temperature, and thus constant water properties (such as water density and kinematic viscosity), as in Eq. 2-2

$$V_{max} = f_1(W_1, W_2, k, Y_2, V_2, \alpha, g) \quad \text{Eq. 2-2}$$

Eq. 2-2 can be rewritten in non-dimensional terms, with V_{max} normalized with the average velocity associated with normal flow depth in the narrower channel, V_2 ; i.e.,

$$\frac{V_{max}}{V_2} = f_2 \left(\frac{W_2}{W_1}, \frac{W_2}{Y_2}, \frac{k}{Y_2}, \alpha, \frac{V_2}{\sqrt{gY_2}} \right) \quad \text{Eq. 2-3}$$

For fully turbulent open-channel flow, Reynolds number exerts no particular effects, and is not included in Eq. 2-3. Also, the Froude number parameter can be replaced with channel slope, S , because S together with Y_2 and k specify, via the Manning's equation, V_2 ; i.e.,

$$\frac{V_{max}}{V_2} = f_3 \left(\frac{W_2}{W_1}, \frac{W_2}{Y_2}, \frac{k}{Y_2}, \alpha, S \right) \quad \text{Eq. 2-4}$$

As the present study is interested in the maximum local velocity in the narrowest portion of the short contraction compared to cross-average velocity, Eq. 2-5 can be restated as

$$\frac{V_{max}}{\overline{V_{max}}} = f_4 \left(\frac{W_2}{W_1}, \frac{W_2}{Y_2}, \frac{k}{Y_2}, \alpha, S \right) \quad \text{Eq. 2-5}$$

Here $\overline{V_{max}}$ is the cross-section average velocity of flow at the location of maximum velocity within the contraction, also referred to as the neck of the contraction. The new parameter $V_{max} / \overline{V_{max}}$, describes the uniformity of velocity at the neck of the contraction by comparing the maximum local velocity to the cross-section average velocity. A similar functional relationship as Eq. 2-3 can be stated for the effective width, W_e , of flow through the most contracted region of flow through a contraction; i.e.,

$$\frac{W_e}{W_2} = f_5 \left(\frac{W_2}{W_1}, \frac{W_2}{Y_2}, \frac{k}{Y_2}, \alpha, S \right) \quad \text{Eq. 2-6}$$

Note that Eq. 2-2 through Eq. 2-6 could be restated in terms of the normal depth of approach flow, Y_1 , to the contraction; e.g., in terms of V_{max}/V_1 , where V_1 is the velocity associated with the normal depth of the approach flow. However, because most numerical models of sub-critical flow in open-channels begin computations at a downstream boundary of known depth (often the normal flow depth, Y_2), it is convenient for the present study to use the normal depth of flow in the contracted channel.

2.3. Prior Literature

As the topic of open-channel hydraulics is a mature subject, with extensive descriptions of open-channel flow under diverse conditions, it is useful to begin a review of the literature on open-channel flow contractions with a brief synopsis of information contained in widely available textbook on open-channel flow. Subsequently, it is useful to determine the general information developed from 2D and 3D numerical models of open-channel flow situations.

2.3.1. Existing Books

In his classic book, *Open Channel Hydraulics*, Ven Te Chow (Chow, 1959) discusses flow through sudden transitions, notably contractions of channel width. In one section Chow derives a one-dimensional Froude-based conservation of momentum approach before moving on to discuss the conservation of energy based investigations of Formica (Chow, 1959; see also Formica 1955). Ultimately, Chow leaves the issue of sudden subcritical transitions to be handled with a one-dimensional conservation of energy approach complimented by use of head-loss coefficients from the earlier work by Formica (1955).

Henderson's classic book, *Open Channel Flow*, (Henderson 1966) also references the head loss coefficients of Formica's 1955 study and uses a one-dimensional energy approach to solve for velocity and depth through a contraction. Formica performed a series of flume experiments where the hydraulic and energy grade lines were examined as flow was passed through varying contractions and expansions. This work resulted in detailed kinetic energy head loss coefficients for various contraction geometries and flow conditions (such as discussed in Chow, 1959 and Formica 1955).

Sturm, in his 2001 book *Open Channel Hydraulics*, (Sturm, 2001). like Chow and Henderson before him, uses a one-dimensional conservation of energy approach to contraction hydraulics. A unique feature of Sturm's book is that it is an early text referencing the use of 1D numerical models of open-channel flow.

In Chaudhry's 2008 text it is stated that, "*Because of large changes in the flow boundaries in a short distance, acceleration plays a dominant role in the flow through transitions as compared to the shear resistance at the channel boundaries. Therefore, the validity of the assumption of one-dimensional flow becomes questionable.*" (Chaudhry, 2008). However, Chaudhry proceeds to provide detailed instruction of the classical one-dimensional standard step energy mythology with head loss coefficients to compute the hydraulic characteristics of a channel transition. The key point in Chaudhry's book is indeed its forewarning of readers about the approximate nature of 1D treatments of flow through a contraction. While Chow acknowledges the usefulness of applying the conservation-of-momentum principle, and Chaudhry questions the validity of the one-dimensional assumption, classic open-channel text books do little to examine the internal

variability of contraction hydraulics. No textbook at the moment addresses the objectives set for this thesis.

2.3.2. Numerical Models

In recent years, many advances have been made in the realm of numerical modeling. Approaches such as unstructured hybrid mesh numerical methods have been developed to simulate all types of open-channel flow including channel contractions (Lai 2010). Numerical models have leapt beyond flow hydraulics in contractions and included sediment transport and scour in their simulation efforts, such as those by Weise (2002) and Marek and Dittrich (2004) using 2D models, Bihs and Olsen (2007), Lai (2010), and Minh Duc and Rodi (2008) using 3D models. However, none of these studies specifically focus on the hydraulic characteristics of the contraction, instead they examine the suitability and accuracy of the numerical model's ability to predict the flow field at structures that locally contract flow, such as at an abutment, and often include the effect of local scour of an alluvial bed at the structures.

Complex, 3D numerical models have provided many insights into the complex hydraulics around structures and through contractions. However, many of the insights focus upon the location, size, and shape of coherent turbulent structures. For instance, Kara, Stoesser, Sturm, and Mulahasan (2015) identified numerous turbulent structures when they modeled flow overtopping a submerged bridge. Typically, articles presenting the results obtained from 3d numerical models, such as those just mentioned, show rather detailed views of the flow structure involved, but do not indicate how the flow structures vary as the geometry of the structure or contraction vary.

Another strong example of 3D numerical modeling is presented by Chrisohoides et al. (Chrisohoides et al. 2003). They used a computational fluid dynamics (CFD) model that solved the 3D Reynolds-averaged Navier-Stokes equations, closed with a $k-\omega$ turbulence method. This model was used in conjunction with a physical model to study the unsteady vortices upstream of the vertical abutments Figure 4 illustrates the unsteady, three-dimensional and turbulent flow patterns found by the Chrisohoides et al. study. The trajectories of individual fluid particles are shown in Figure 4 as they follow their extremely turbulent path through the flow field upstream of the abutment.

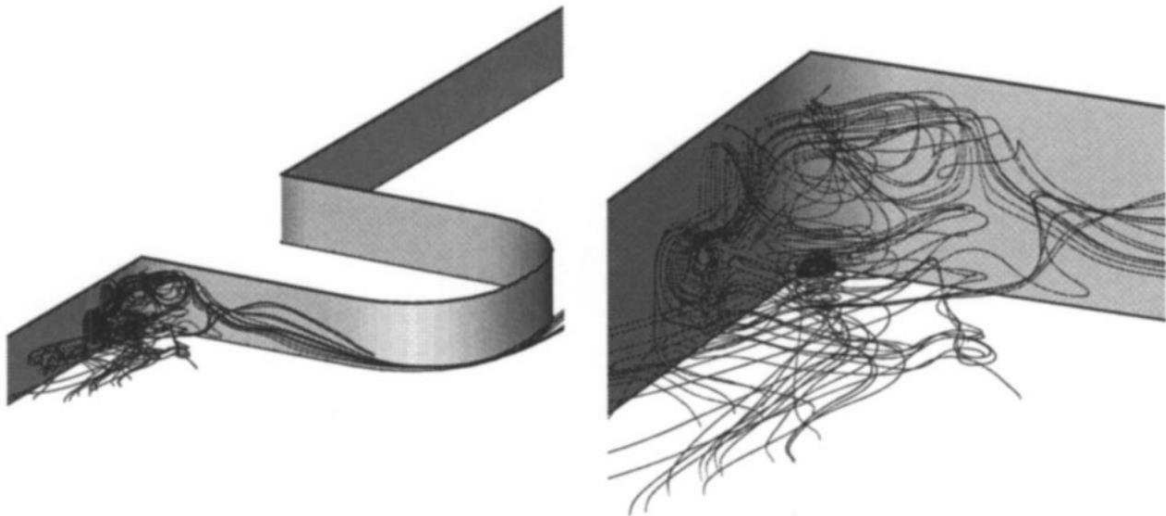


Figure 4: Calculated instantaneous 3D particle trajectories upstream of an abutment (Chrisohoides et al. 2003)

The study by Chrisohoides et al. stresses the continually changing and three-dimensional nature of the turbulent flow around the abutments, providing detailed qualitative descriptions. However, the paper also states that, “*a more quantitative description of the unsteady flow fields, including*

an analysis of the frequencies of the large-scale structures that are present in various regions of the flow, is beyond the scope of this work.” (Chrisohoides et al. 2003). Lacking quantitative data over a range of contraction configurations, it is difficult for a design practitioner to extract applicable information from the Chrisohoides et al. study.

Another numerical study, by Koken (2017) features an analysis of coherent structures in two spill-through abutments. The 3D numerical model used by Koken for this study was a Spalart–Almaras based detached eddy simulation (DES) model without wall functions. The DES model implicitly solved the incompressible 3D Navier–Stokes equations using a fifth order upwind biased method in conjunction with a central second order scheme. The model was bound by non-slip channel boundaries and a rigid lid free-surface. The inlet boundary condition was fed a fluctuating turbulent velocity profile that was generated from a separate large eddy simulation (LES) model to produce realistic flow conditions. Meanwhile, a convective outlet boundary condition configured to allow turbulent vortices to exit the model without causing unphysical oscillations (Koken, 2017).

Simulated flow in Koken’s 3D models was passed through spill-through abutments. Four simulations were run two with a contraction ratio (W_2/W_1) value of 0.55 and two with a W_2/W_1 value of 0.88. One of each contraction ratio was run with a flat bed and one with a deformed bed. Figure 5 shows the modeling results, including the shapes and locations of coherent turbulence structures. Koken points out the locations of corner vortices (CV), horseshoe vortices (HV), mid-flow vortices (MFV), contraction vortices (CTV), and separated shear layers (SSL).

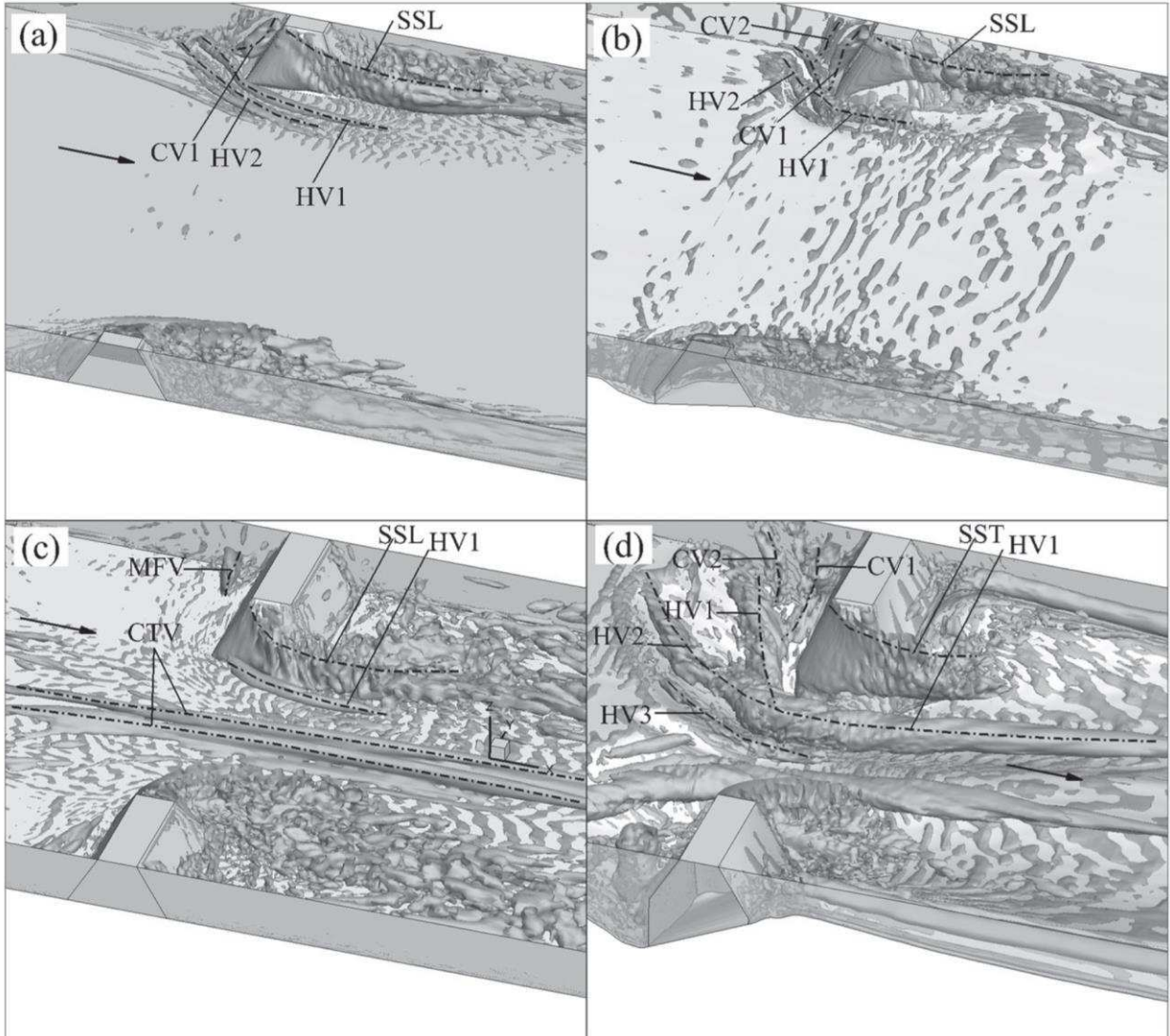


Figure 5: Representation of coherent structures around abutments (Koken, 2017);

(a) $W_2/W_1=0.88$ flatbed , (b) $W_2/W_1=0.88$ deformed bed, (c) $W_2/W_1=0.55$ flatbed, (d) $W_2/W_1=0.55$ deformed bed

Of particular interest are the pair of counter-rotating contraction vortices that appear in the center of the channel, as shown in Figure 5(c) where $W_2/W_1= 0.55$, which are absent from Figure 5a where $W_2/W_1= 0.88$. While these patterns of turbulent flow are interesting, Koken does not offer any quantitative data concerning how these patterns may affect design parameters such as

velocity or bed shear. Also, presumably due to the efforts involved with 3D numerical modeling, Koken was only able to investigate the flow field of two contraction ratios with two bed conditions. Many more simulations would be required to reveal any trends associated with the alternation of hydraulic variables.

While 3D numerical models, suitably used, give many insights into the hydraulic characteristics of contractions in open-channels, they are currently expensive and time-consuming to implement. Each boundary condition, each input, and every parameter must be carefully set and calibrated to produce reliable 3D modeling results. It is not unusual for the results of several numerical or physical models to be used as the input for a 3D numerical model. Such efforts currently exceed the resources available to the average design practitioner.

However, depth-averaged, 2D numerical models have become readily accessible as a method for determining the main features of flow through open-channel contractions. While 2D numerical models lack the ability to resolve some of the complicated flow patterns that 3D methods can compute, they can resolve many of the prevailing flow patterns without requiring the prodigious resources and efforts needed by a 3D model. Therefore, the present study has selected a 2D numerical model as a viable way to obtain insights into the flow field within a contraction.

3. EXPERIMENTAL PROCEDURE

3.1. Assumptions and Simplifications

Channel contractions in natural river systems can be complicated by factors such as continuously changing irregular geometry, non-uniform roughness, channel curvature, loose boundaries, and unsteady flow, just to name a few complexities. Conducting a study to account for all possible variables was not feasible, and is not required for simulation of flow through the contractions of typical of bridge waterways. Therefore, the present study adopted a simplified set of assumptions, so as to readily enable the numerical model used to reveal how the main features of flow in a contraction vary.

The channel geometry is defined as a rigid prismatic rectangular cross-section with relatively smooth sides. The channel width changes at a defined location over a length described by the transition shape. The channel width remains constant upstream and downstream on the contraction. There is no channel expansion. The boundary roughness, k , of the channel is expressed as a Manning's roughness coefficient, n , estimated using Strickler's equation (e.g., see Julien, 2010). As n is taken herein to be a constant, Eq. 2-5 and Eq. 2-6 simplify further as

$$\frac{V_{max}}{\bar{V}_{max}} = f_6 \left(\frac{W_2}{W_1}, \frac{W_2}{Y_2}, n, \alpha, S \right) \quad \text{Eq. 3-1}$$

and

$$\frac{W_e}{W_2} = f_7 \left(\frac{W_2}{W_1}, \frac{W_2}{Y_2}, n, \alpha, S \right) \quad \text{Eq. 3-2}$$

The channel bed is uniformly sloped, with slope S being expressed, via Manning's flow resistance equation, in terms of the variables in Table 1. Flow characteristics are defined in terms of a steady flow rate (in terms of uniform flow, $Q = V_2 Y_2 = V_1 Y_1$) and a constant downstream water surface elevation, Y_2 .

3.2. Description of Numerical Model

The Sedimentation and River Hydraulics – Two-Dimensional model (SRH-2D) is a numerical model developed by the United States Department of Interior, Bureau of Reclamation. The model elements are formed by a flexible mesh consisting of triangular and quadrilateral elements. SRH-2D uses a finite-volume numerical algorithm to solve depth-averaged, St. Venant dynamic wave equations for open-channel flow. (Lai, 2008).

The default turbulence model used in SRH-2D is the Zero-Equation or parabolic model, which is widely used (e.g., Rodi, 1993). Using the parabolic model, the depth-averaged eddy viscosity, ν_e , is calculated as

$$\nu_e = \alpha V_* h \quad \text{Eq. 3-3}$$

Here, V_* is friction velocity, and h is flow depth. The use of Eq. (3-3) sets the turbulence coefficient, α , at a value of between 0.3 and 1 (Rodi, 1993).

For the series of numerical simulations done for the present study, Aqueveo's SMS 12.2.8 interface was used to assist in implementing the SRH model. This interface provides a means to graphically define and edit the input data the numerical model uses for its calculations.

3.3. Model Setup

Each simulation required four layers of information including a mesh, monitor points, boundary conditions, and materials. The mesh provided geometry and node locations for the ensuing calculations. The mesh was comprised of quadrilateral and triangular elements. The element spacing is 0.0305m (0.1ft) on average over most the model. However, immediately downstream of the contraction the mesh spacing was decreased to 0.0061m (0.02ft) along the flume walls and 0.0152m (0.05ft) along the centerline. Upstream and downstream of this dense mesh region transitions were created between the dense and less dense mesh regions. Along the full length of the mesh boundary a consistent element width of 0.0061m (0.02ft) was used. After the mesh was created, the elevation of every mesh node was interpolated from a planar elevation dataset, and used to define the bed slope. Figure 6 provides an example of how the mesh is structured.

Each simulation utilized three monitoring points. These points record the flow characteristics at a finite location for each calculation time step. One point was located near the upstream boundary, one near the downstream boundary, and one just downstream of the short contraction segment.

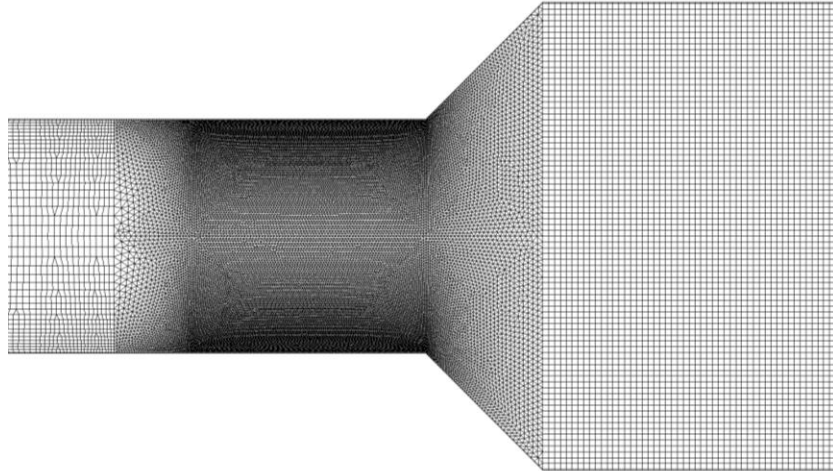


Figure 6: Example model mesh. Note the finer mesh in locations where velocity gradients were anticipated to be relatively large.

Three major boundary control components were used for each simulation. First, an inlet boundary control was placed near the upstream edge of the mesh. This line provided a constant inflow to the model. Next, near the downstream edge of the mesh, an exit boundary control was placed. This line defined the water surface elevation as flow exited the model. In all simulations, this boundary was defined as the normal depth, as calculated from the one-dimensional Manning's equation. Finally, the edges of the mesh were bound by a no-slip wall boundary condition.

3.4. Model Simulation Configuration

The simulations were executed with a 0.05 second time-step for durations of 0.25 hour, with a reporting interval of 0.01 hour. All simulations were started with an initial water-surface elevation equal to the downstream normal depth, Y_2 . The parabolic turbulence parameter was set to 0.3 to achieve the most realistic turbulence simulations per the recommendation of Federal

Highway Administration Technical Resource Center expert, Scott Hogan (personal communication).

3.5. Experimental Program

The program of numerical experiments was designed to reveal how the flow field (maximum velocity and flow separation) responded to changes in contraction ratio, bed roughness, slope, and transition shape. Table 2 shows the planned experiments and the major parameters of each.

The first experiment set was designed to identify the primary relationship between flow characteristics and contraction ratio. As such, experiment set 1 involved 13 different contraction ratios, all with the same flow rate, slope, bed roughness, and transition shape.

Experiment sets two and three differ from experiment set 1 by having an altered Manning's roughness coefficient. Meanwhile, experiment sets 4 and 5 provide slope variations to set 1. The purpose of experiment sets 2 through 6 was to show how flow characteristics differ from experiment set 1 when slope and roughness are changed. As such, each of these sets has only three simulations, each with a different contraction ratio.

To see how transition shape affects contraction flow characteristics, two additional experiments sets were created. Experiment set 6 featured identical test parameters to experiment set 1, except for the transition shape, which is a 45° half-bevel. This meant that half of the change in channel width is accomplished with 45° wall segment while the remainder is formed by a 90° wall.

Meanwhile, experiment set 7 is identical to experiment set 6, except these simulations featured a

45° full-bevel transition shape, where all the channel width change is accomplished with 45° wall segments. Figure 7 shows a schematic for each of the three contraction transition geometries.

Table 2: Experimental program

Set Number	Transition Shape	W_2 (m)	W_2/W_1	Slope	n	Q (cms)	D.S. W.S.E. (m)
1	Abrupt	0.30	0.125	0.0003	0.025	0.142	2.45
	Abrupt	0.49	0.2	0.0003	0.025	0.142	1.21
	Abrupt	0.61	0.25	0.0003	0.025	0.142	0.90
	Abrupt	0.73	0.3	0.0003	0.025	0.142	0.72
	Abrupt	0.91	0.375	0.0003	0.025	0.142	0.56
	Abrupt	0.98	0.4	0.0003	0.025	0.142	0.52
	Abrupt	1.22	0.5	0.0003	0.025	0.142	0.42
	Abrupt	1.46	0.6	0.0003	0.025	0.142	0.36
	Abrupt	1.52	0.625	0.0003	0.025	0.142	0.35
	Abrupt	1.71	0.7	0.0003	0.025	0.142	0.32
	Abrupt	1.83	0.75	0.0003	0.025	0.142	0.30
	Abrupt	1.95	0.8	0.0003	0.025	0.142	0.29
	Abrupt	2.19	0.9	0.0003	0.025	0.142	0.26
2	Abrupt	0.61	0.25	0.0003	0.015	0.142	0.59
	Abrupt	1.22	0.5	0.0003	0.015	0.142	0.30
	Abrupt	1.83	0.75	0.0003	0.015	0.142	0.22
3	Abrupt	0.61	0.25	0.0003	0.035	0.142	1.20
	Abrupt	1.22	0.5	0.0003	0.035	0.142	0.54
	Abrupt	1.83	0.75	0.0003	0.035	0.142	0.38
4	Abrupt	0.61	0.25	0.00065	0.025	0.142	0.65
	Abrupt	1.22	0.5	0.00065	0.025	0.142	0.32
	Abrupt	1.83	0.75	0.00065	0.025	0.142	0.233
5	Abrupt	0.61	0.25	0.001	0.025	0.142	0.55
	Abrupt	1.22	0.5	0.001	0.025	0.142	0.28
	Abrupt	1.83	0.75	0.001	0.025	0.142	0.20
6	45° Half Bevel	0.61	0.25	0.0003	0.025	0.142	0.90
	45° Half Bevel	0.91	0.375	0.0003	0.025	0.142	0.56
	45° Half Bevel	1.22	0.5	0.0003	0.025	0.142	0.42
	45° Half Bevel	1.52	0.625	0.0003	0.025	0.142	0.35
	45° Half Bevel	1.83	0.75	0.0003	0.025	0.142	0.30
7	45° Full Bevel	0.61	0.25	0.0003	0.025	0.142	0.90
	45° Full Bevel	0.91	0.375	0.0003	0.025	0.142	0.56
	45° Full Bevel	1.22	0.5	0.0003	0.025	0.142	0.42
	45° Full Bevel	1.52	0.625	0.0003	0.025	0.142	0.35
	45° Full Bevel	1.83	0.75	0.0003	0.025	0.142	0.30

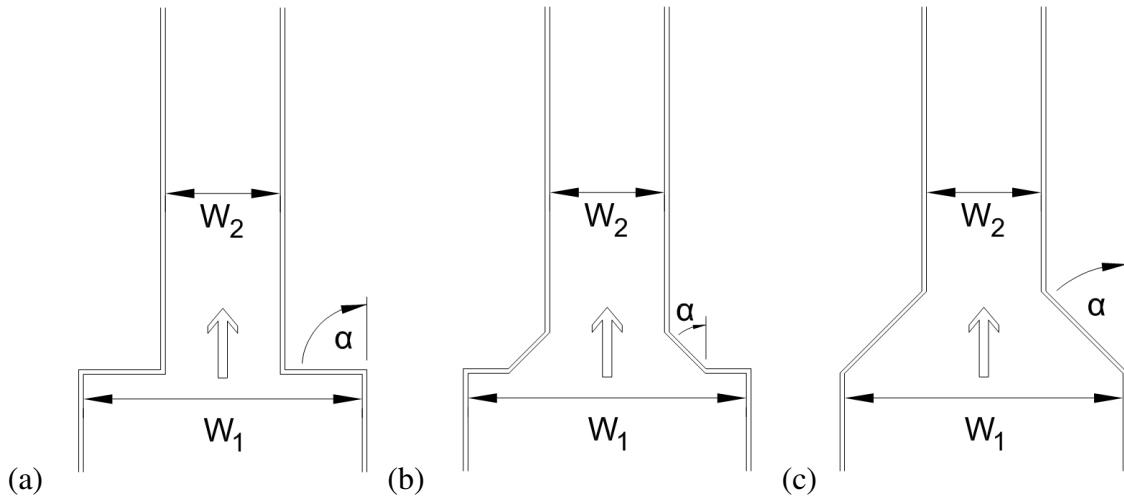


Figure 7: Schematic of the contraction-transition geometries simulated: (a) abrupt; (b) 45° half-bevel; and, (c) 45° full-bevel.

All simulations have been formulated on the basis of an idealized contraction. The parameters of an idealized contraction include:

- 1) Prismatic rectangular channel;
- 2) Uniform channel slope;
- 3) Uniform channel roughness;
- 4) Inflow is steady; and,
- 5) Downstream boundary flow depth is equal to normal depth.

The selected flow rate yields a width to flow depth ratio in the uncontracted channel under hydraulically normal depth conditions ranges between 10 and 15, which is not dissimilar to the condition found in natural waterways. However, it is worth nothing that the contracted channel normal flow depth condition enforced at the downstream boundary results in significantly lower width to depth ratios. In all cases, the flow conditions are subcritical with Froude values well below one.

3.6. Boundary Sensitivity Analysis

To insure the accuracy of the modeling results, it was deemed prudent to conduct a brief investigation into the sensitivity of the model to the downstream boundary condition. If the boundary condition had been placed too close to the area of interest, it may have had an undue influence on the results. To test for this condition, a simulation in which the downstream boundary condition was moved 3.048m (10ft) further downstream was conducted. The centerline velocity and depth profile results were then compared. Figure 8 shows a comparison of the velocity and depth profiles. The simulation used for the base-line condition had an abrupt contraction with a width ratio of 50%, a flow of 0.142 cms (5cfs), a Manning's resistance coefficient of $n = 0.015$, and a slope of $S = 0.0003$. The results show an overall increase in average velocity of 0.16% and an overall decrease in average flow depth of 0.08%. Based upon these results, it was concluded that the results are not significantly sensitive to the downstream boundary condition location, as it was placed during the simulations.

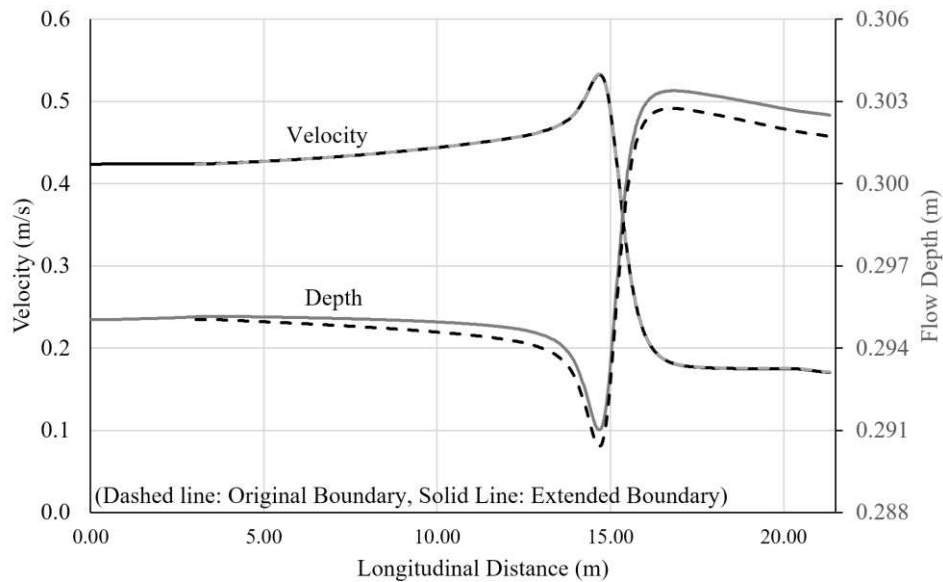


Figure 8: Downstream boundary sensitivity analysis, a comparison between the velocity and depth profiles two simulations, in which one simulation's boundary has been moved.

3.7. Simulation Duration Sensitivity Analysis

As additional assurance regarding the accuracy of modeling results, a brief investigation was conducted into the sensitivity of the model to the simulation duration. If the duration of the model simulation is too short, then steady flow conditions may not have been fully established. To test for this condition, a node near the area of peak velocity was selected in each simulation. The velocity magnitude at this node for the last simulation time step was noted and then compared to the previous time step. If the velocity at this node showed a change greater than 0.0003 m/s (0.001ft/s) then the simulation duration was considered too brief. Ultimately, 0.25 hours was used as the duration for all the simulations. This duration was more than sufficient to produce steady and consistent results.

3.8. Data Collection and Analysis

SRH-2D yields values for depth, water surface elevation, bed elevation, velocity magnitude, velocity vector, and shear stress at every node location for every reported time-step. This output can be presented in a plan view format as contour lines, colored maps, or read directly from individual nodes. Alternatively, output can also be presented as a profile that can be viewed or exported as a table of values along a line. Data was collected directly from the nodes as well as from profiles for the present study.

Upon completion of a model simulation, the results were analyzed and data of interest were recorded. First, the plan view of the mesh was analyzed. The velocity map was used to record the location and magnitude of the maximum velocity within the short contraction region. Figure 9

shows the velocity magnitude results map for one of the simulations; units are m/s. Flow direction is from the wider to the narrower open-channel.

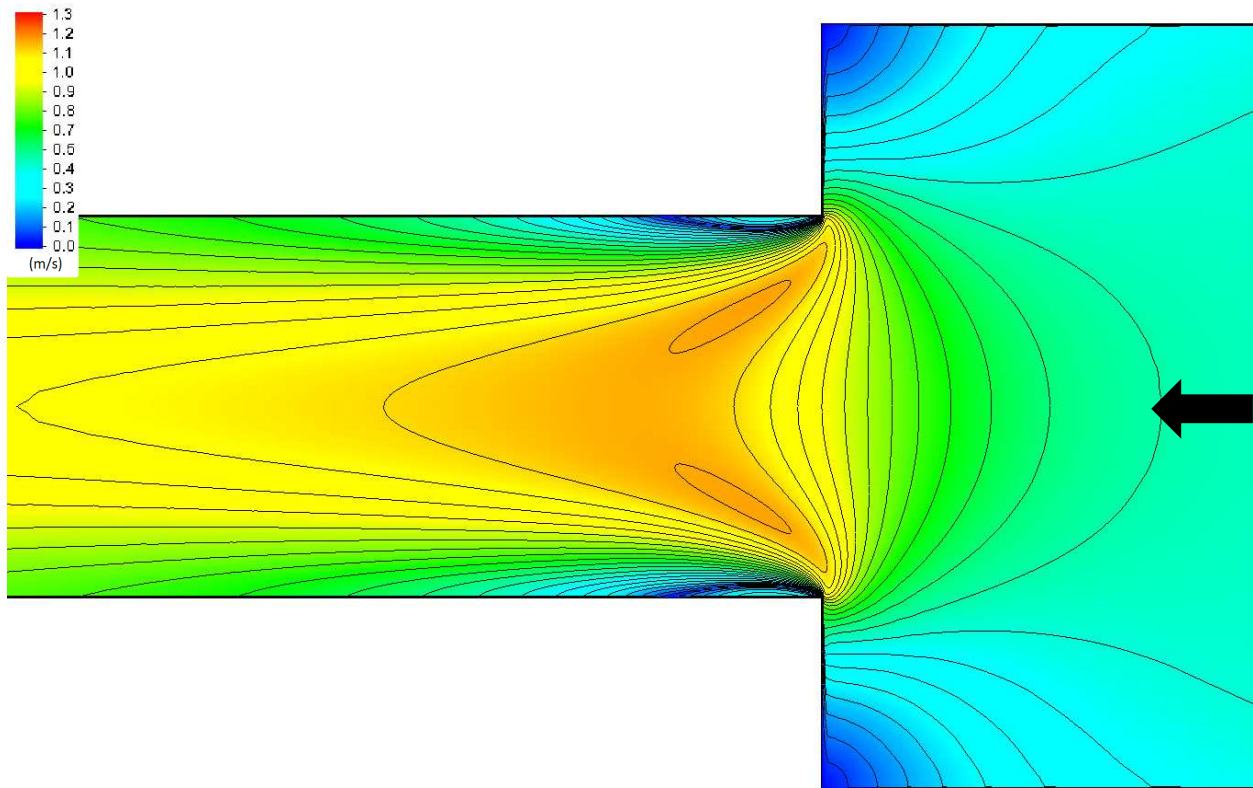


Figure 9: Example velocity magnitude results map. Note the location of velocity maximum and the two regions of flow separation in the contraction.

The velocity vector map was used to identify the areas of flow separation, and the width of flow separation regions were recorded at their widest. The edge of the flow separation region was discerned within the results as the dividing line between downstream and upstream velocity vectors. Figure 10 gives an example of the velocity vector map from a simulation in the area of flow separation, note the recirculating vortex. In cases where no upstream velocity vectors were found the width of flow separation was recorded as zero. Figure 11 shows a flow field where the

velocity vectors are distorted around an area of low velocity, but the field lacks any upstream or recirculating motion. However, it is worth noting that all velocity map results show areas of lower downstream velocity just downstream of the contraction transitions.

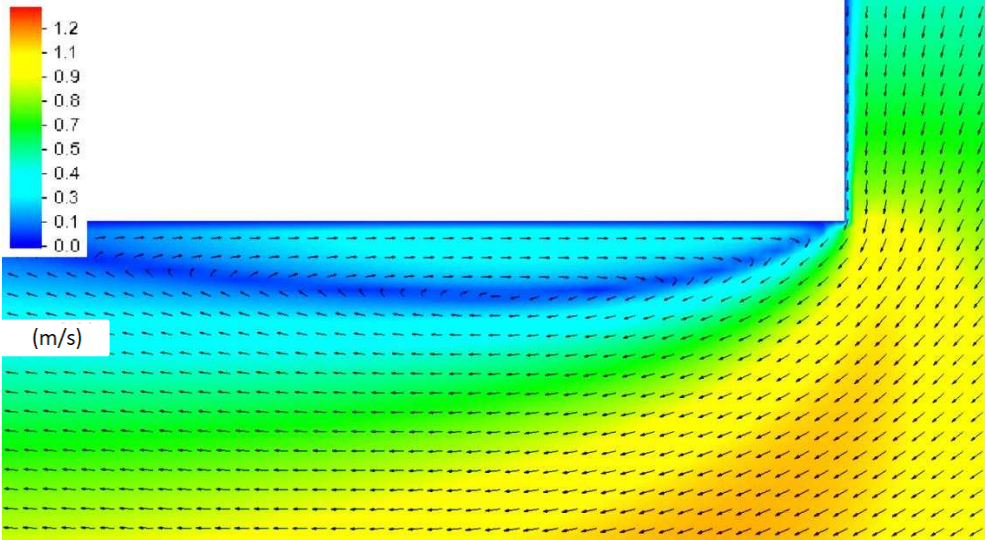


Figure 10: Example of recirculating flow separation vector map, showing half the channel

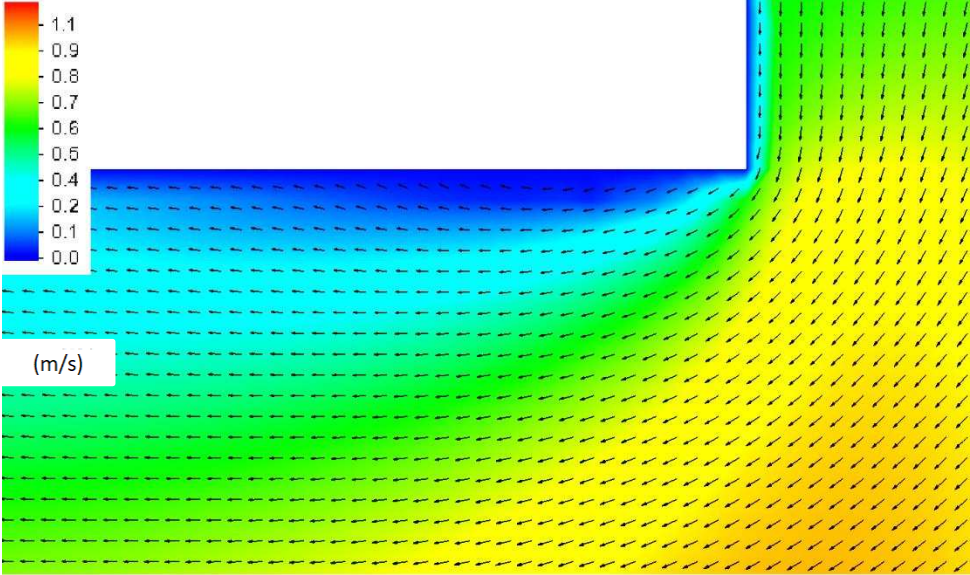


Figure 11: Example of non-recirculating flow separation vector map showing half the channel

In addition to the plan view results, a centerline profile showing depth and velocity was produced for each simulation. This profile was used to ascertain the maximum centerline velocity and its location. The profile also illuminates the short contraction velocity amplification. To be noted, in some cases the maximum velocity in the contraction exceeds the maximum centerline velocity, and the centerline velocity is a poor indicator of the cross-section average velocity.

Figure 12 shows a typical depth and velocity centerline profile from a simulation as an example.

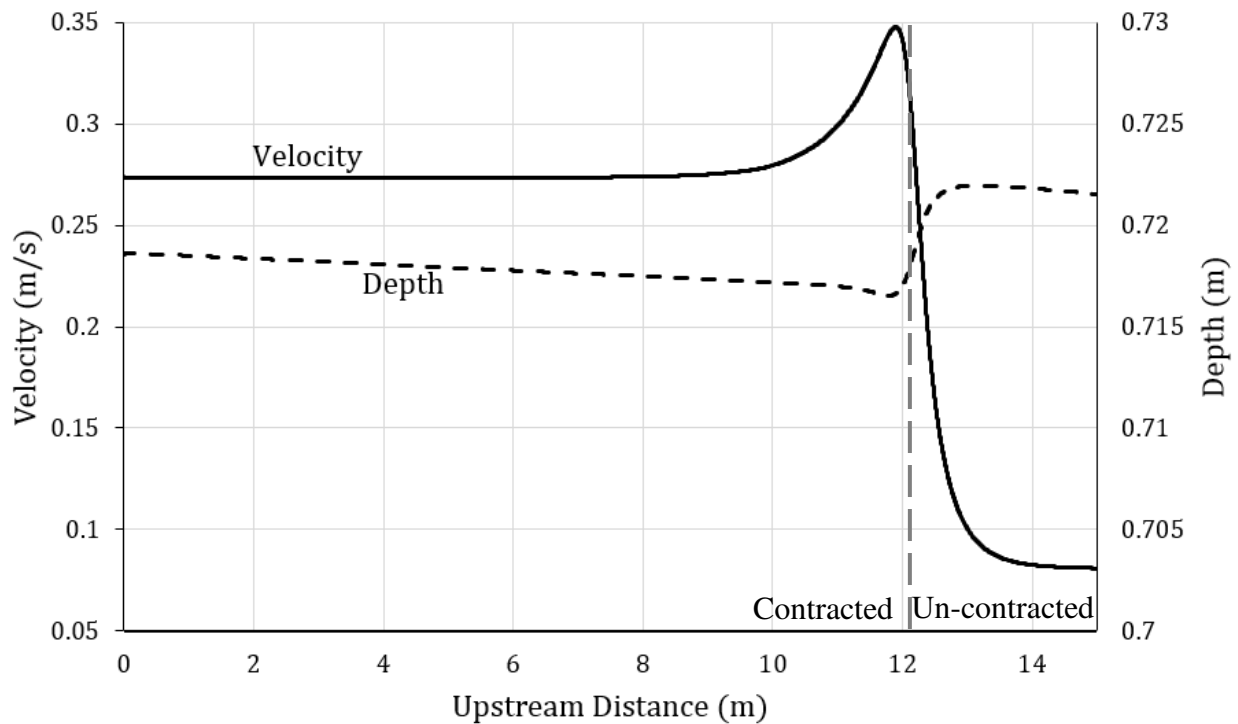


Figure 12: Example depth and velocity centerline profile

A final set of data was also collected by processing the velocity vector results into longitudinal and lateral scalar datasets. At the location of maximum velocity, a depth and longitudinal velocity cross-section was produced. This cross-section provided a means to calculate a total flow area and thus a cross-sectional averaged velocity. If desired, additional information such as

the kinematic energy correction factor can be computed from this dataset. Figure 13 is a cross-section plot of the flow depth and longitudinal velocity at the location of maximum contraction velocity.

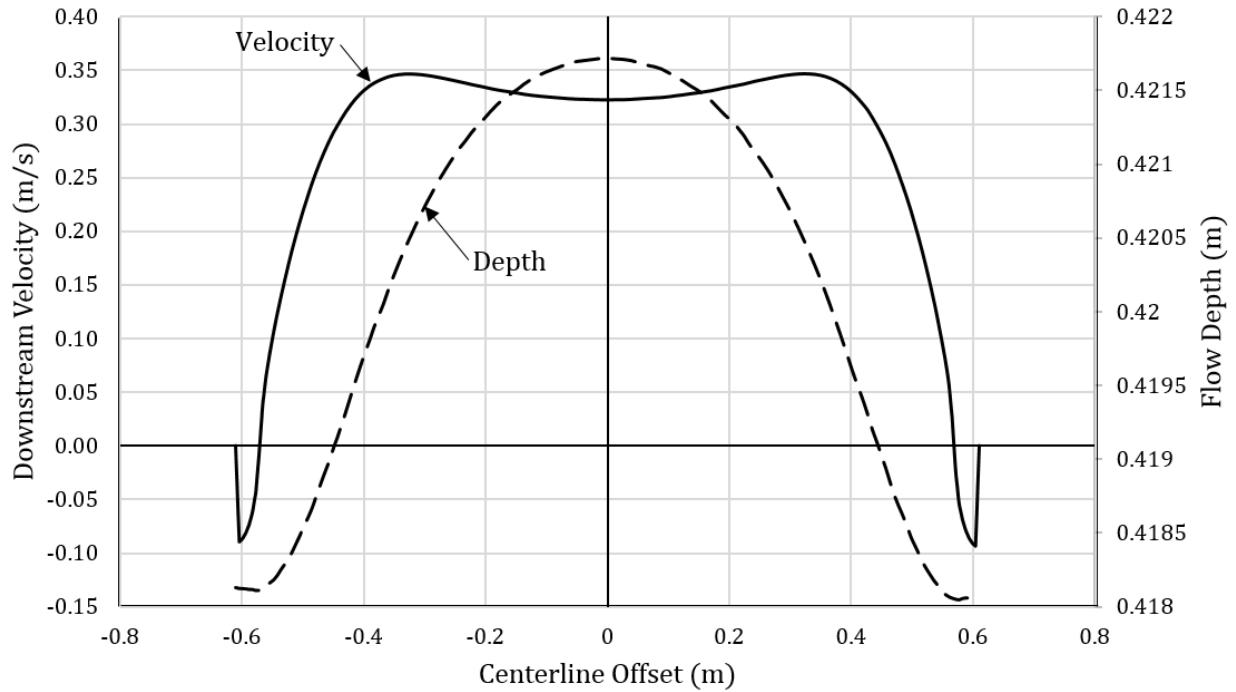


Figure 13: Example depth and longitudinal velocity cross-section

4. RESULTS FROM THE MODEL

As the objective of this study was to examine, by means of a 2D numerical model, the flow-field characteristics of a channel contraction, the variables of primary interest were the key characteristics of the flow field; i.e., the maximum velocity of flow, and the magnitude of the width dimensions of flow separation regions within the contraction. Accordingly, the main objective of these experiments was determining how these variables changed as contraction ratio and transition shape were altered. Also investigated were the flow-field influences of changes in channel slope and roughness.

In order to study these variables, specific and consistent measurements were defined. Table 3 summarizes these measurement variables.

Table 3: Definitions of Simulation Result Variables

Variable	Description
V_{max}	Maximum Velocity
\overline{V}_{max}	The cross-section average velocity at the location of V_{max}
X_{max}	Longitudinal location of maximum velocity, as measured from beginning of contraction
O_{max}	Lateral location of maximum velocity, as measured from centerline
V_{lat}	Maximum Lateral Velocity
X_{lat}	Longitudinal location of maximum lateral velocity, as measured from beginning of contraction
O_{lat}	Lateral location of maximum lateral velocity, as measured from centerline
W_e	Minimum effective Flow Width, as measured from edge to edge of flow separation

The V_{max} was recorded from the node with the highest velocity magnitude. The location of V_{max} was recorded as the longitudinal distance (X_{max}) downstream from the beginning of the contraction transition and the lateral offset distance (O_{max}) from the flume centerline. In all cases the maximum velocity was symmetrical from one side of the flume to the other. Therefore, if an O_{max} value of zero is given, the maximum velocity was located on the flume centerline, otherwise the reader may correctly assume that the maximum velocity occurred in two locations which are symmetrically located about the centerline as indicated by O_{max} and X_{max} . Figure 14 provides a schematic that shows the maximum velocity location measurement methodology in detail.

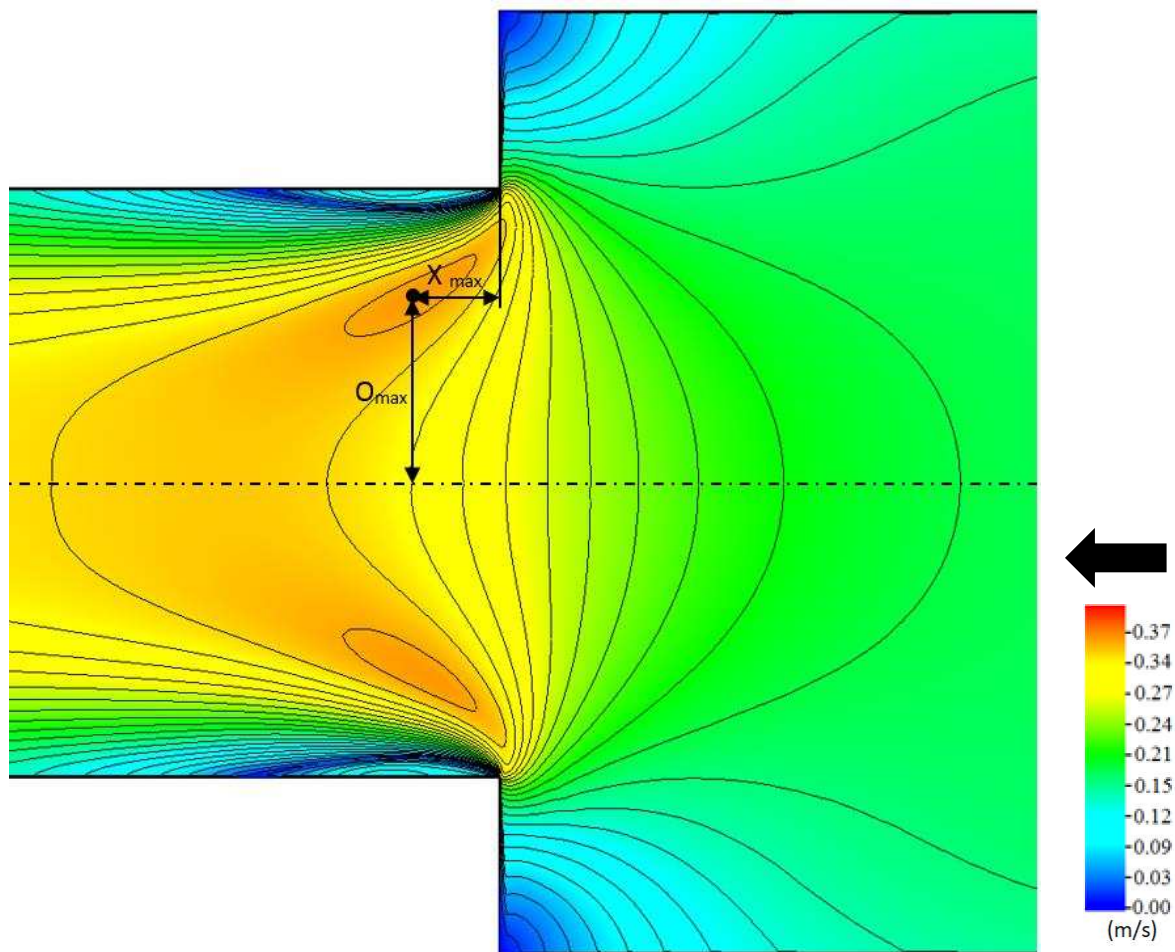


Figure 14: Maximum velocity location schematic

The next set of results pertains to the maximum lateral velocity observed (V_{lat}). In this case, only the lateral component of the velocity vector is considered. The longitudinal (X_{lat}) and the lateral offset (O_{lat}) location measurements follow the same protocol as the corresponding maximum velocity measurements and are also symmetrical. It bears noting that X_{lat} is measured in the downstream direction and negative values indicate that the location of maximum lateral velocity occurs upstream of the beginning of the channel contraction transition. The methodology shown in Figure 14 for the location measurement of maximum velocity is consistent with the methodology used to measure maximum lateral velocity.

A third set of measurements has been designed to describe the scale of flow separation. The narrowest effective flow width, W_e , is the measurement from edge to edge of flow separation. The edge of each flow separation region is defined by a narrow band of zero velocity flow with upstream velocity on the opposite side, as shown in Figure 15. The longitudinal distance, X_e , from the beginning of contraction to the point of narrowest effective flow is also recorded. In some simulation results, quantifiable flow separation was not observed due to the lack of upstream flow. However, a definitive distortion of velocity is observable in the results. In these cases, W_e equals W_2 .

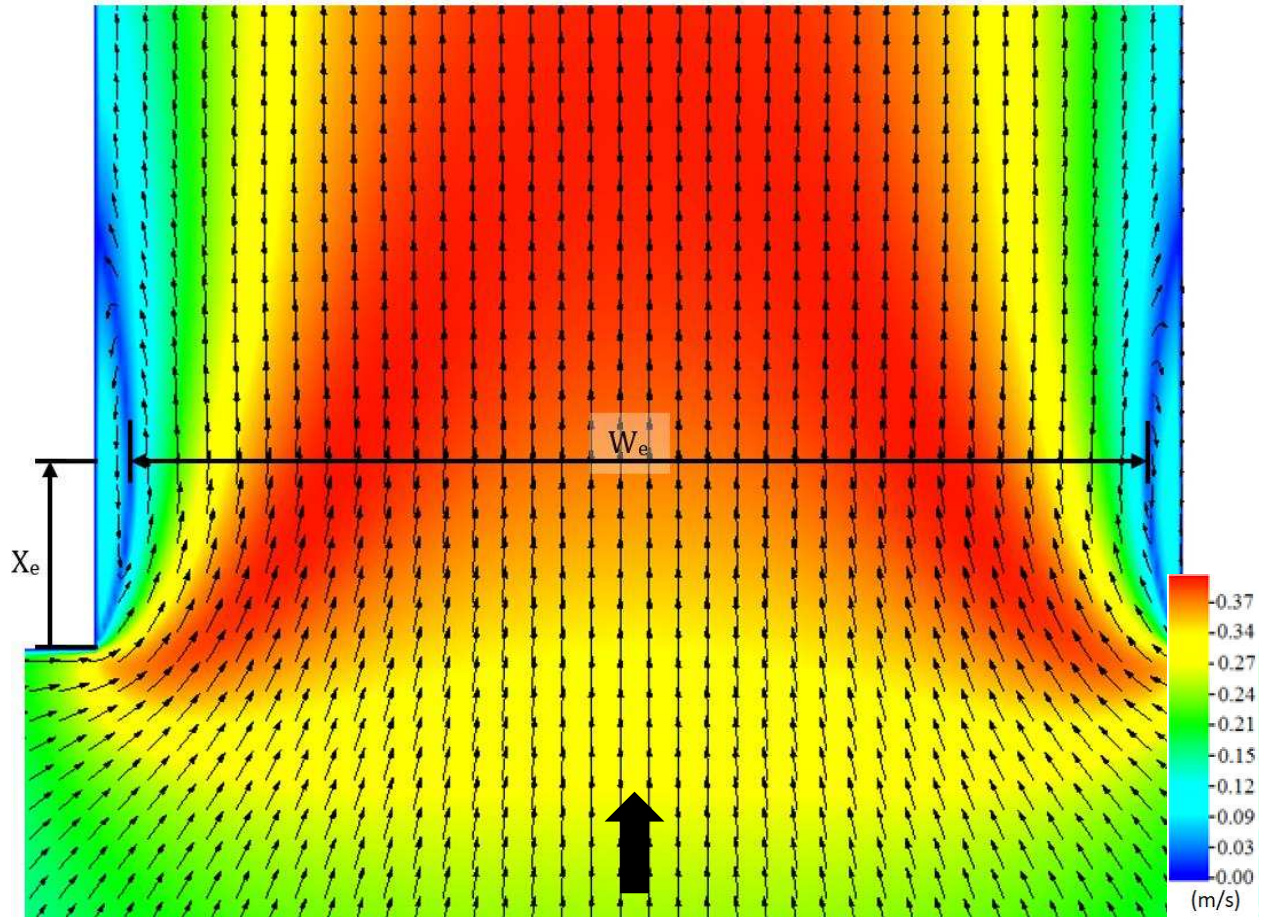


Figure 15: Minimum effective flow width dimension schematic

4.1. Variation in Location of Peak Velocity

It is not surprising that velocity amplification and uniformity vary with W_2/W_1 , transition shape, channel roughness, and slope. However, before asking how and why these characteristics change, it is useful to observe where maximum velocity occurs.

4.1.1. Influence of Contraction Ratio of Peak Velocity Location

As W_2/W_1 changes, the location of the peak velocity also changes. In experiment set 1 (see Table 2), the location of maximum velocity was symmetrically mirrored about the flume centerline for $W_2/W_1 \geq 0.5$. However, when $W_2/W_1 \leq 0.4$, the maximum velocity occurred directly on the flow's centerline. Meanwhile, the single location of peak velocity moved further downstream from the transition as W_2/W_1 increased from 0.125 to 0.4. However, this single spot of peak velocity split into two spots when $W_2/W_1 \approx 0.5$, the location of peak velocity moved significantly upstream, and continued to do so as W_2/W_1 was further increased. Figure 16 provides a series of velocity plots that demonstrate the migration of maximum velocity location, while Figure 17 shows a quantitative analysis of the same relationship.

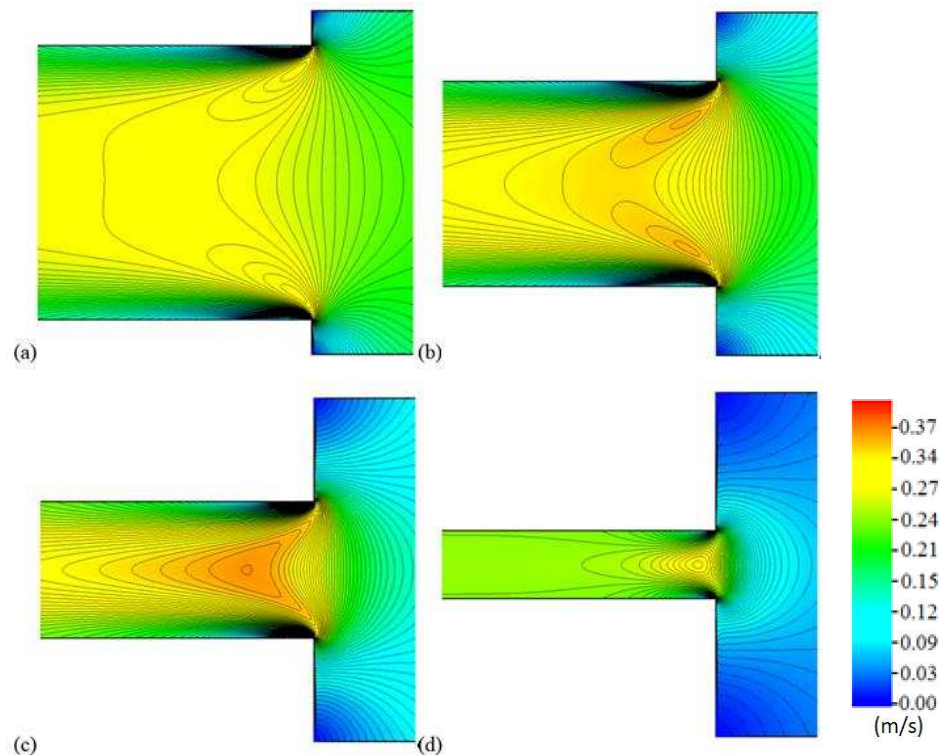


Figure 16: Velocity plots showing changes of maximum velocity location in experiment set

1: (a) $W_2/W_1 = 0.8$; (b) $W_2/W_1 = 0.6$; (c) $W_2/W_1 = 0.4$; and, (d) $W_2/W_1 = 0.2$

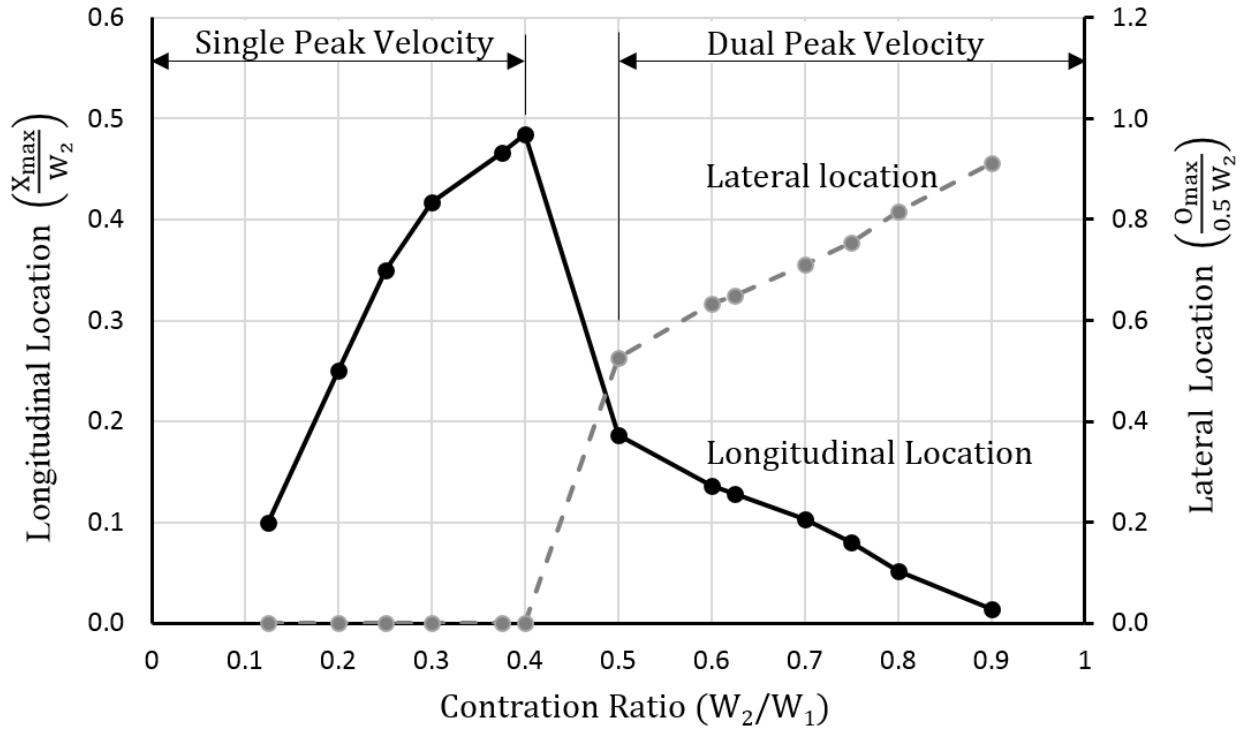


Figure 17: Longitudinal location of maximum velocity versus contraction ratio for experiment set 1

The patterns of peak velocity match a previously observed pattern in turbulent coherent structures. *“It is found that in the small contraction ratio [$W_2/W_1=0.88$] coherent structures forming around the abutments are very similar to the ones observed for isolated abutments. In the large contraction ratio [$W_2/W_1=0.55$], at flatbed conditions, which represent the initiation of the scour, two counter rotating contraction vortices form at the center of the channel close to the channel bed, elongated in the flow direction.”* (Koken, 2017)

4.1.2. Influence of Transition Shape on Velocity Location

Contraction ratio, W_2/W_1 , is not the only factor determining where the peak velocity occurs. Transition shape can completely change where the peak velocities are located. Abrupt

contractions result in maximum velocities that are located along the centerline or offset from the centerline by 50 to 85 percent of the distance to the boundary. However, 45° full and half-bevel transition shapes resulted in peak velocities that were located precisely on the corners of the channel transition, for at all but the most severe contraction ratios. Notice how the locations of highest velocity cling to the corners of the beveled transition shapes in parts (a) and (b) in Figure 18 while the highest velocity regions in the abrupt transition results, part (c) Figure 18, are located almost half way between the centerline and the channel edge.

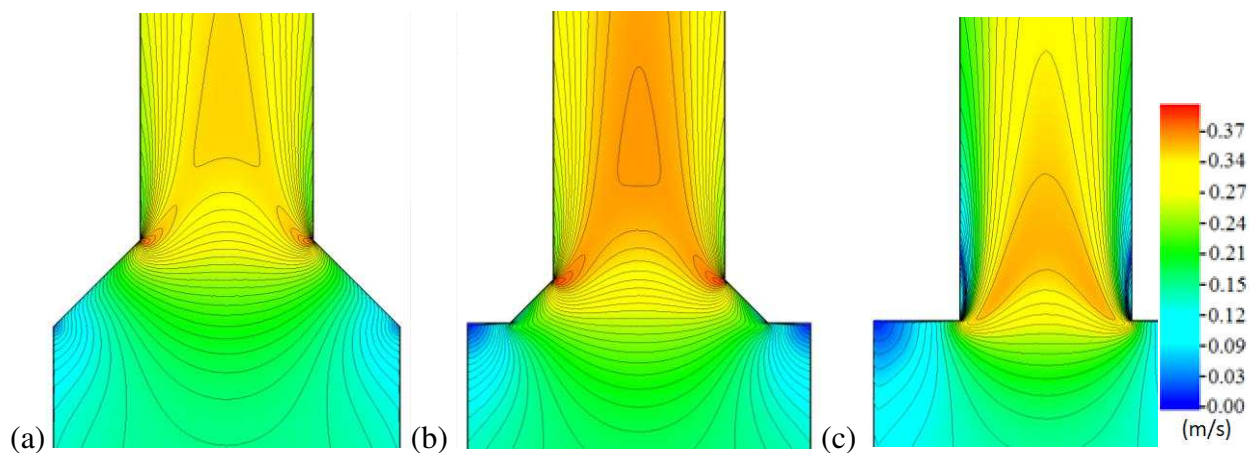


Figure 18: Velocity plots with varying transition shapes, $W_2/W_1=0.5$: (a) 45° full bevel; (b) 45° half bevel; and, (c) abrupt

The location of maximum velocity in a short contraction with a bevel transition shape is readily predictable because the contraction geometry guides flow into the contraction. Except for the simulations where $W_2/W_1 = 0.25$, all simulations with a beveled transition shape resulted in a maximum velocity located both longitudinally and laterally at the transition corners. In the case of simulations with a $W_2/W_1 = 0.25$, the peak velocity location is controlled primarily by W_2/W_1 while the significance of the transition shape is reduced. Figure 19 graphs the lateral location of maximum velocity against W_2/W_1 with varying transition shape.

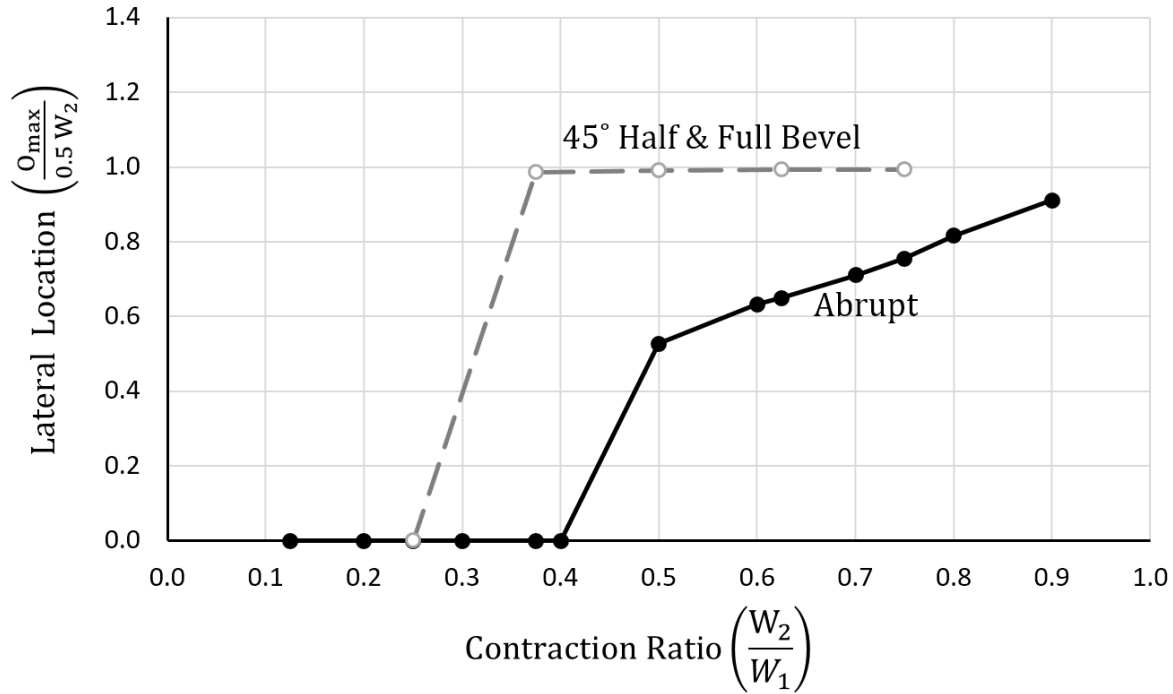


Figure 19: Lateral location of maximum velocity versus contraction ratio, with varying transition shape

Having observed that some values of W_2/W_1 produce a peak velocity at a single location while others produce the same peak velocity in two locations, one might ask if this pattern is linked to flow distribution within the short contraction.

4.2. Variation in Velocity Uniformity

Figure 16 shows that velocity is not uniformly distributed across the channel within a short contraction. Velocity uniformity parameter, $V_{max} / \overline{V_{max}}$ is intended to provide a measure of how much the peak velocity differs from the cross-section average velocity at the same location.

Velocity uniformity is calculated by dividing the maximum velocity by the cross-section average velocity.

4.2.1. Influence of Contraction Ratio of Velocity Uniformity

Though $V_{max} / \overline{V_{max}}$ would seem likely to be proportionally related to W_2/W_1 , the variation in peak velocity location indicates that the $V_{max} / \overline{V_{max}}$ varies with W_2/W_1 . This relationship is shown by Figure 20.

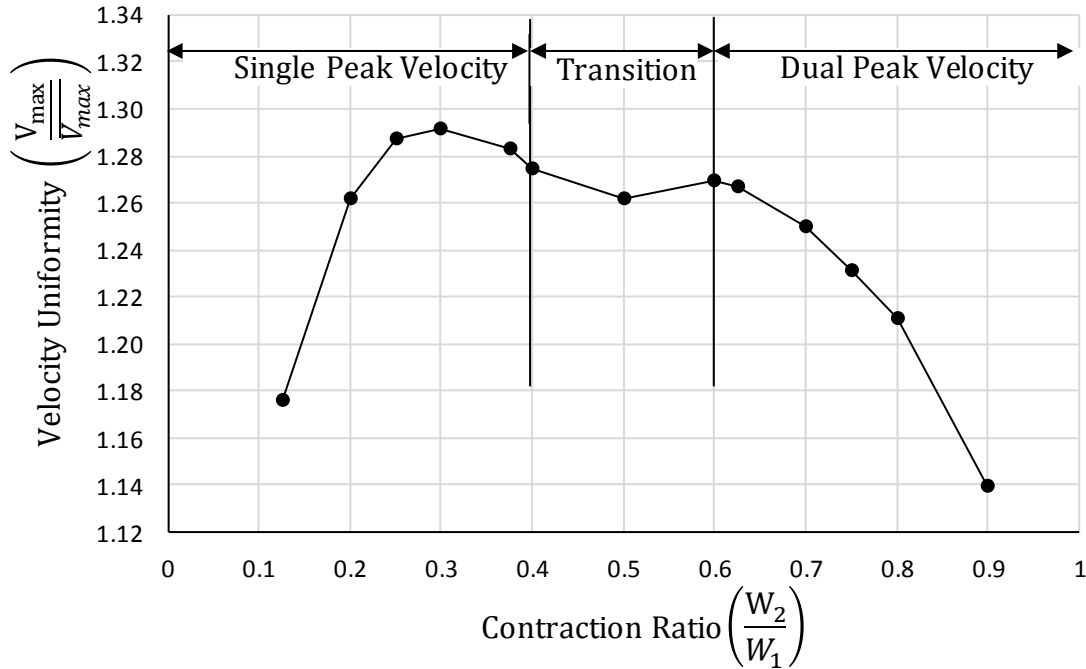


Figure 20: Velocity uniformity, $V_{max} / \overline{V_{max}}$ versus contraction ratio

The parameter $V_{max} / \overline{V_{max}}$ increases as W_2/W_1 increases from 0.125 to 0.3. As the severity of the contraction eases the amount of flow redirection is reduced slightly, thus increasing the velocity in the center of the contraction and pushing the peak velocity further downstream, along the centerline. Meanwhile, the majority of the flow is still redirected around the abrupt transitions corners, causing slower velocities near the channel boundaries.

As W_2/W_1 increases from 0.3 to 0.5, $V_{max} / \overline{V_{max}}$ decreases slightly before increasing again between 0.5 and 0.6. Within this zone of moderate W_2/W_1 values the single pocket of peak velocity splits into two. For experiment set 1 (see Table 2), the lowest value of W_2/W_1 to feature dual peak velocity location is 0.5. However, it is reasonable to suspect that the experiments with W_2/W_1 of 0.4 and 0.375 are also subject to the momentum characteristics that result in dual peak velocities locations even if to a lesser extent. Figure 21 reinforces this theory. Contraction ratios of $W_2/W_1 = 0.5, 0.4,$ and 0.375 are shown respectively in parts (b), (c), and (d) of Figure 21. Please note that the area of highest velocity, shown in red, creates a “^” shaped pattern in parts (b), (c), and (d) of Figure 21, thus leading this author to name this range of W_2/W_1 as a transition range. It is this pattern of velocity distribution that causes the minor decrease in $V_{max} / \overline{V_{max}}$.

Meanwhile, when $W_2/W_1 = 0.6$, shown in part (a) of Figure 21, demonstrates that the locations of peak velocity are clearly split. On the other side of the transition zone, a W_2/W_1 of 0.3, shown in part (e) of Figure 21, indicates that the location of peak velocity is clearly in the center of the channel, and does not extend upstream in a “^” configuration.

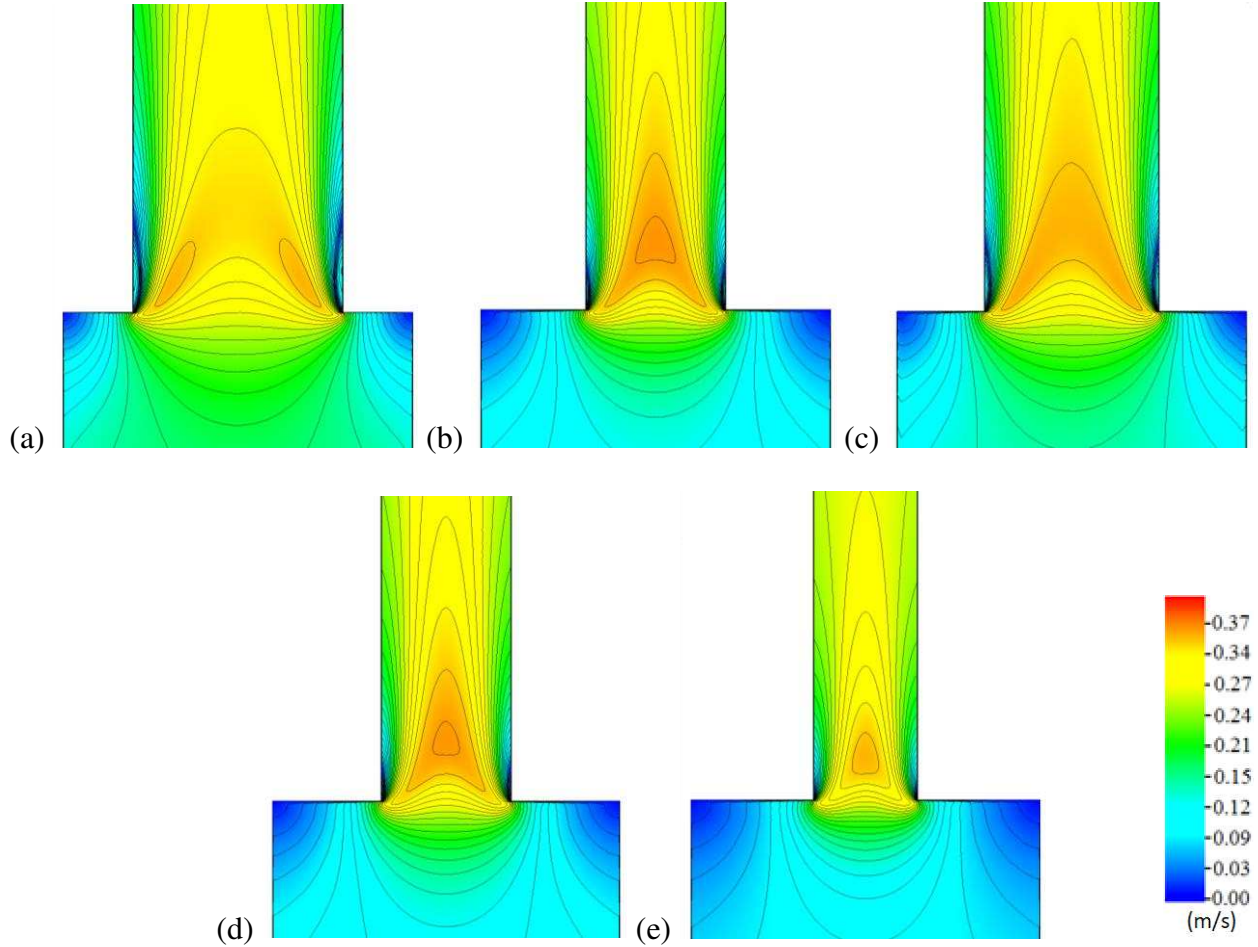


Figure 21: Experiment set 1, velocity plots: (a) $W_2/W_1=0.6$,(b) $W_2/W_1=0.5$; (c) $W_2/W_1=0.4$; (d) $W_2/W_1=0.375$; and, (e) $W_2/W_1=0.3$

Additionally, $V_{max} / \overline{V_{max}}$ decreases steeply between the W_2/W_1 of 0.6 and 0.9, where it reaches a minimum. This decrease in $V_{max} / \overline{V_{max}}$ corresponds to a decrease in the severity of contraction. Whereas $V_{max} / \overline{V_{max}}$ provides a useful proxy for understanding how the peak velocity relates to the cross-section average velocity, it does not provide sufficiently full insight of the velocity distribution. To obtain a more complete insight, examining the cross-section percent standard deviation in velocity at the location of maximum velocity can be helpful, as shown in Figure 22.

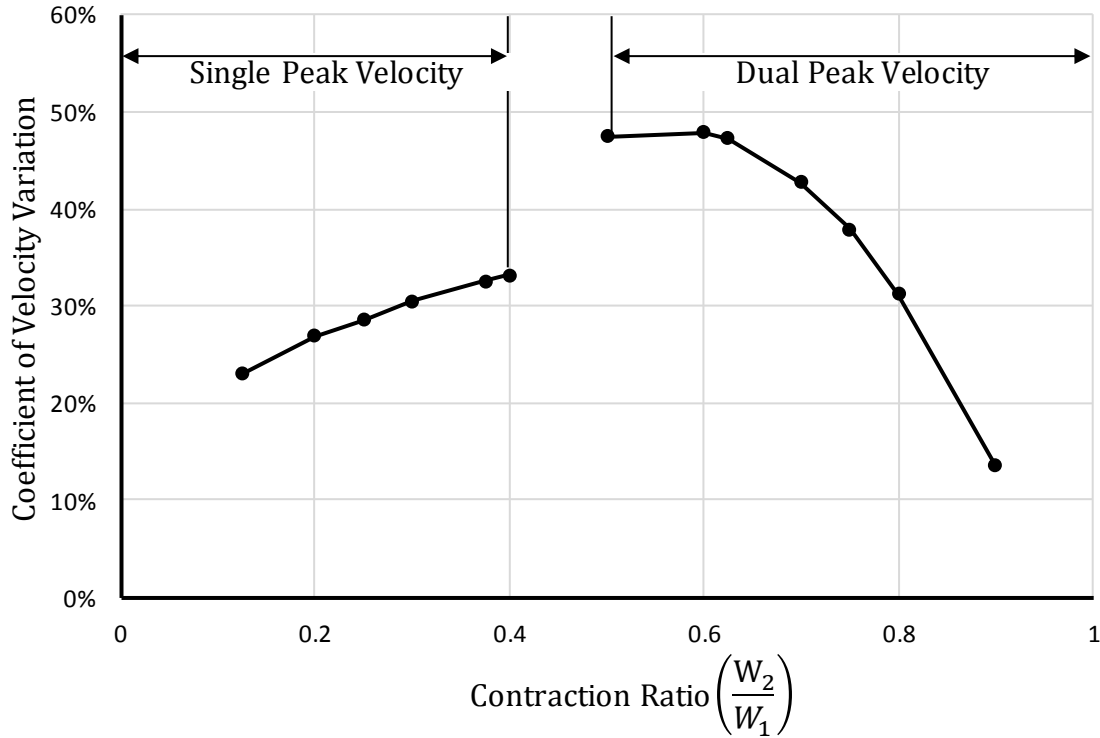


Figure 22: Coefficient of velocity variation at the cross-section of maximum velocity for experiment set 1

Figure 22 shows that the coefficient of velocity variation with W_2/W_1 up until a $W_2/W_1=0.4$. Then the trend shows a discontinuity at velocity location separation point between the $W_2/W_1=0.4$ and 0.5. As W_2/W_1 continues to increase, the coefficient of velocity variation in the region of greatest contraction of flow decreases.

4.2.2. Influence of Bed Roughness on Velocity Uniformity

How much the peak velocity differs from the average velocity is not only dependent upon W_2/W_1 . Bed roughness, expressed here as Manning's n , also plays a significant role. Figure 23 shows that decreasing the bed roughness results in higher values of $\sigma_{V_{max}} / \overline{V_{max}}$, while increasing

the bed roughness results in a lower values of $V_{max} / \overline{V_{max}}$. Both the increase and decrease in $V_{max} / \overline{V_{max}}$ can be attributed to the effect of bed roughness on lateral advection. A rougher surface increases bed shear stress, which then causes an increase in lateral advection, as shown in the advective terms of the St. Venant equations.

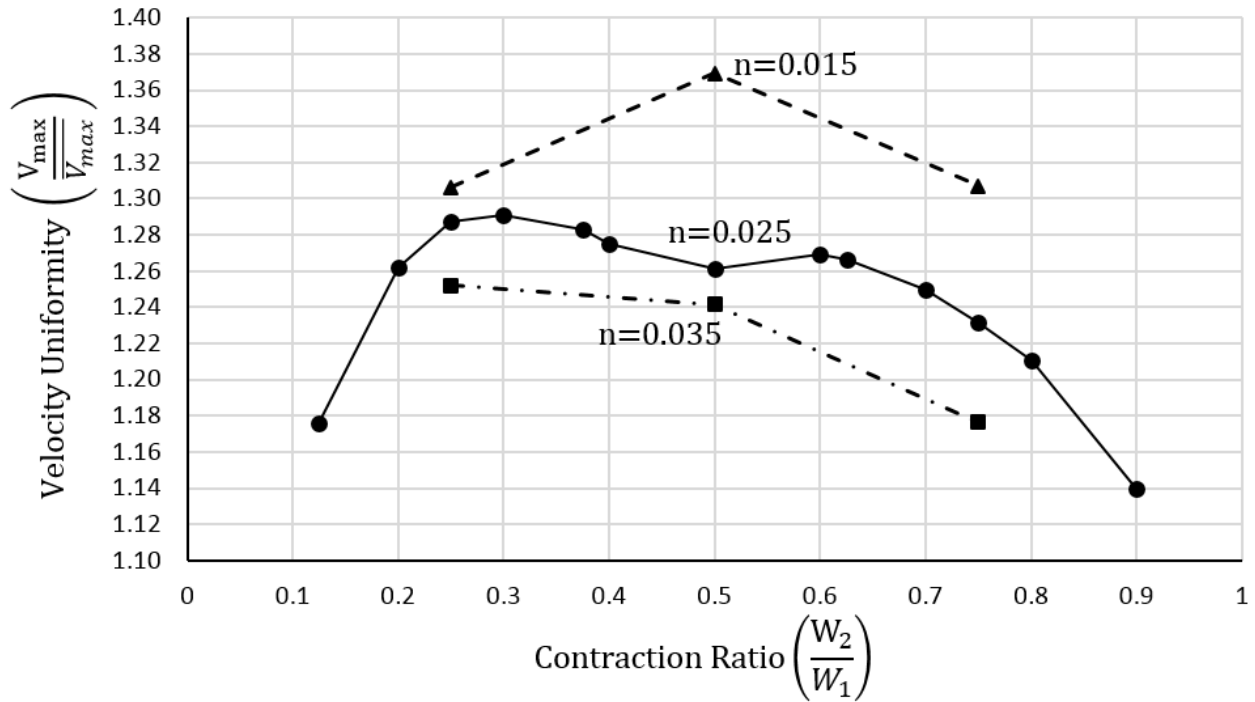


Figure 23: Velocity uniformity versus contraction ratio with varying roughness

In Figure 23, one may also notice that the influence of bed roughness has a slightly larger influence on velocity uniformity at larger contraction ratios than at smaller W_2/W_1 . It can be argued that the influence of bed roughness is somewhat diminished at smaller contraction ratios because the channel geometry plays a relatively larger role in velocity distribution when the contraction is more severe.

4.2.3. Influence of Slope on Velocity Uniformity

How much the peak velocity differs from the average velocity is not only dependent upon W_2/W_1 and n . Channel slope, S , also plays a significant role. Figure 24 shows that increasing the channel slope results in higher values of $V_{max} / \overline{V_{max}}$.

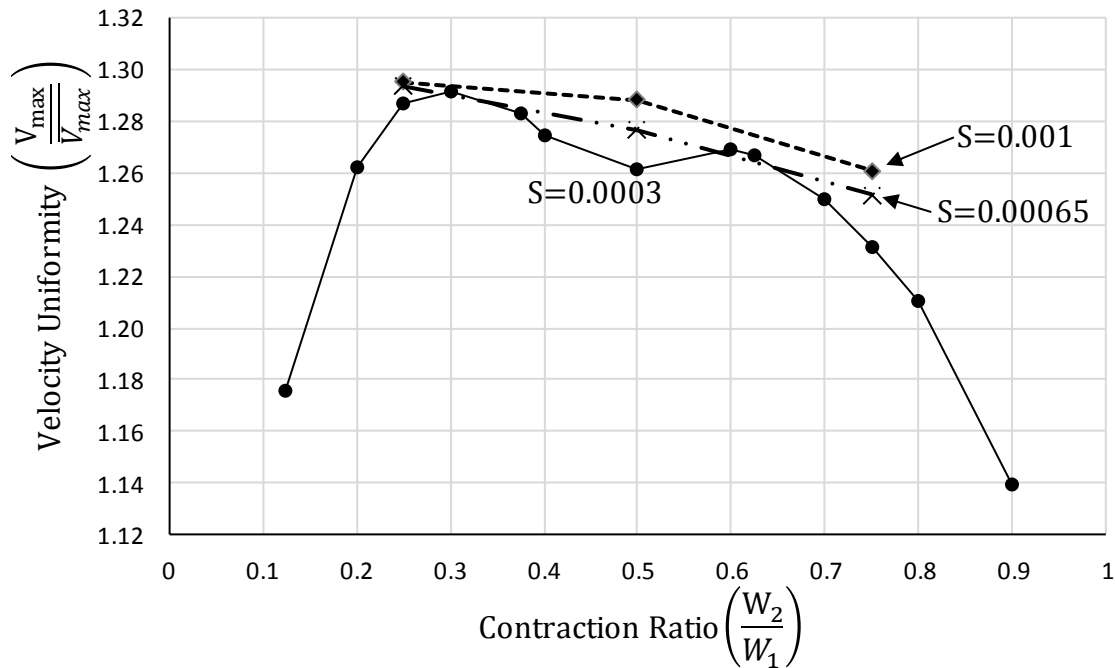


Figure 24: Velocity uniformity versus contraction ratio with varying slope

$V_{max} / \overline{V_{max}}$ increases as slope increases due to an increase in maximum velocity that is not directly proportional to an increase in the cross-section averaged velocity. Figure 25 provides velocity cross-sections with three different slopes, all of which have an identical contraction ratio of 0.5, bed roughness of 0.025, and abrupt transition shapes. The negative, upstream directed, velocities intensify as the slope steepens. The intensification is a result of the increased kinetic energy in the system. However, it also results in a disproportionately lower cross-section average velocity, thereby producing a lower value for $V_{max} / \overline{V_{max}}$.

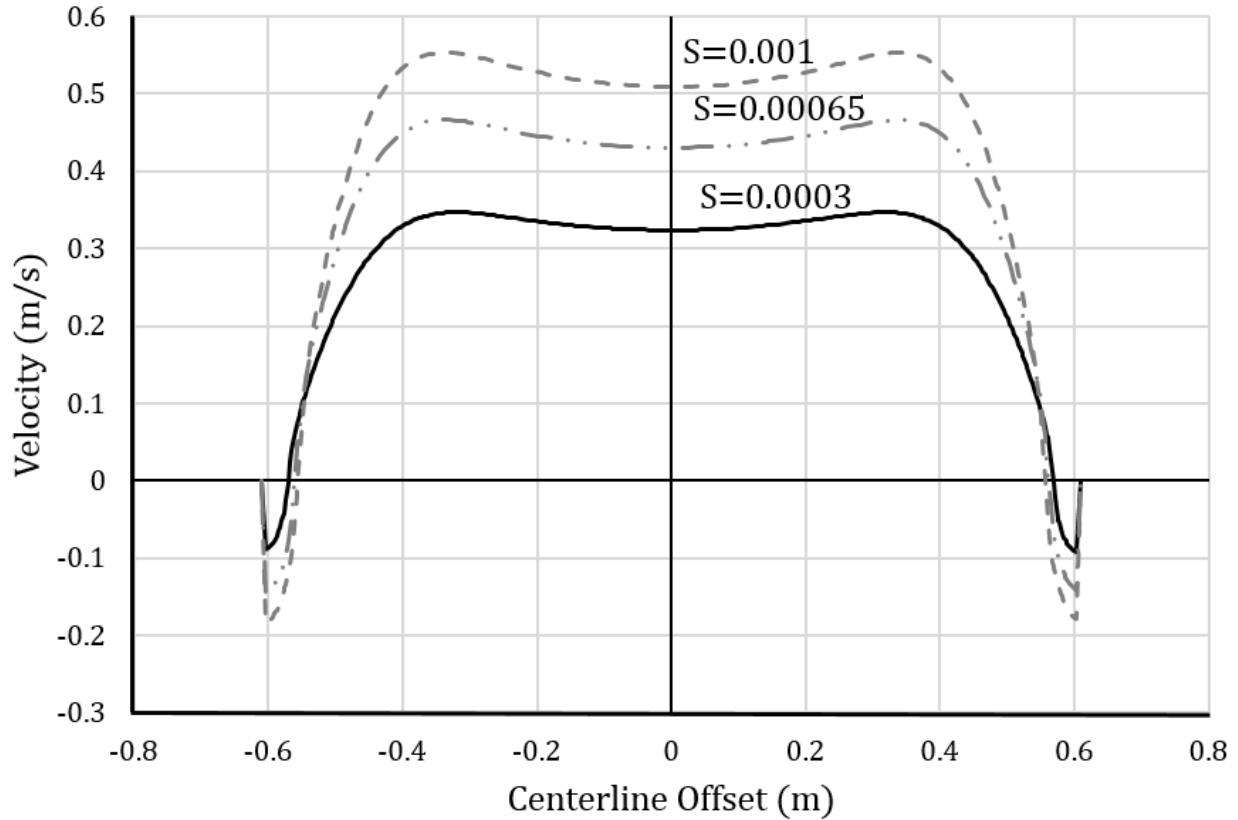


Figure 25: Velocity cross-sections with varying slope at a contraction ratio, W_2/W_1 , of 0.5

4.2.4. Influence of Transition Shape on Velocity Uniformity

How much the peak velocity differs from the average velocity is not only dependent upon W_2/W_1 , n , and S . Transition shape also plays a significant role. Figure 26 show how changing the shape of the transition affects velocity uniformity. It is unsurprising that both beveled transition shapes result in much lower values of $V_{max} / \overline{V_{max}}$ at lower contraction ratios. However, this trend did not extend to simulations where $W_2/W_1 > 0.5$, thus indicating that transition shape plays a greater role in velocity uniformity when the change in channel width is more severe.

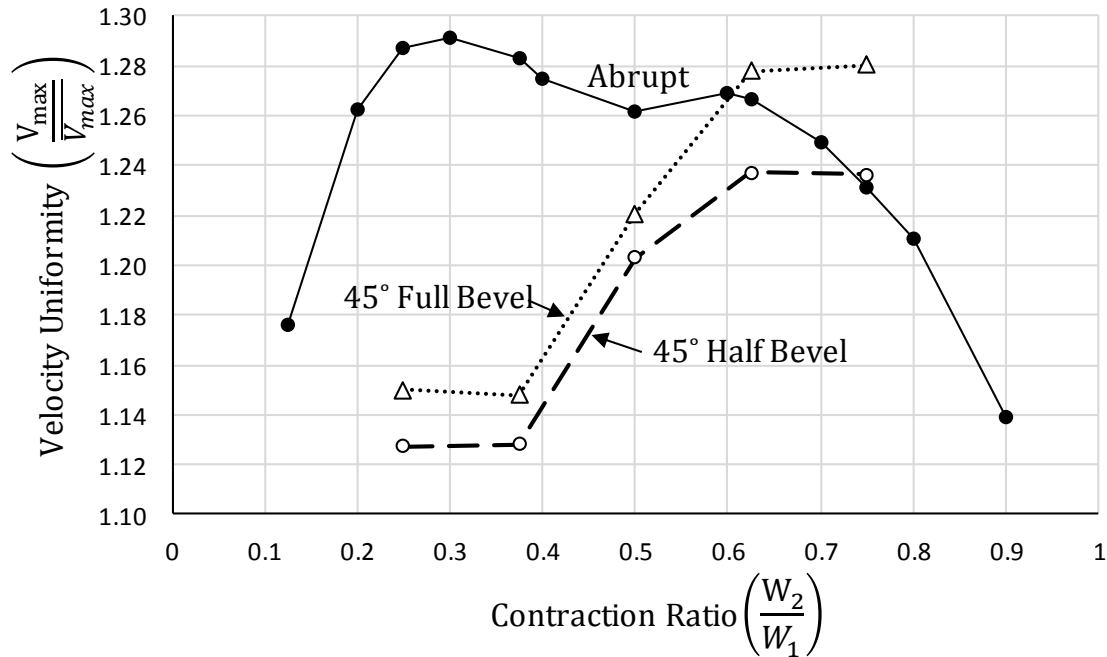


Figure 26: Velocity uniformity versus contraction ratio with varying transition shape

It is also noteworthy that the 45° half-bevel shape consistently produces more uniform velocities than the 45° full-bevel shape. Upon closer examination, one will find that the velocity distributions are almost identical, with the exception that the 45° half-bevel shape produces a slightly lower maximum velocity. The abrupt and full bevel transition shapes have two flow inflection points, one at the un-contracted boundary which directs flow towards the channel center and another at the contracted channel edge where flow is directed downstream. However, the half-bevel transition shape has three inflection points. It is thought that spreading the angular acceleration of flow redirection over three inflection points may be the cause for this slightly lower peak velocity, and therefore the lower $V_{max} / \overline{V_{max}}$ values.

4.3. Variation in Velocity Amplification

When examining velocity within the contraction it is useful to define the term velocity amplification, $\overline{V_{max}} / V_1$. This term compares the cross-section average velocity at the location of maximum velocity within the contracted section to the cross-section averaged velocity of the uncontracted channel at normal depth, as calculated with one-dimensional assumptions. Also, this term provides a suitable reference for how much the velocity has been increased by the contraction from a hydraulically normal depth condition. However, it is important to remember that in all simulations the flow is subcritical; therefore, the downstream hydraulic conditions control the flow characteristics in the contraction. It is also worth noting that the downstream control in each simulation is set to normal depth.

4.3.1. Influence of Contraction Ratio on Velocity Amplification

Experiment set 1 is a good data set to examine how velocity amplification varies with slope. Figure 27 shows that velocity amplification can vary significantly with W_2/W_1 , but reaches a maximum in the vicinity of a W_2/W_1 of 0.4 within the selected experiment set.

Conservation of momentum, as necessitated by the geometry of the contraction, is the driving force behind $\overline{V_{max}} / V_1$. Flow is redirected towards the center of the channel by the constriction, however momentum does not allow this flow to turn abruptly. This lateral momentum effect results in areas of higher unit discharge and therefore higher velocities.

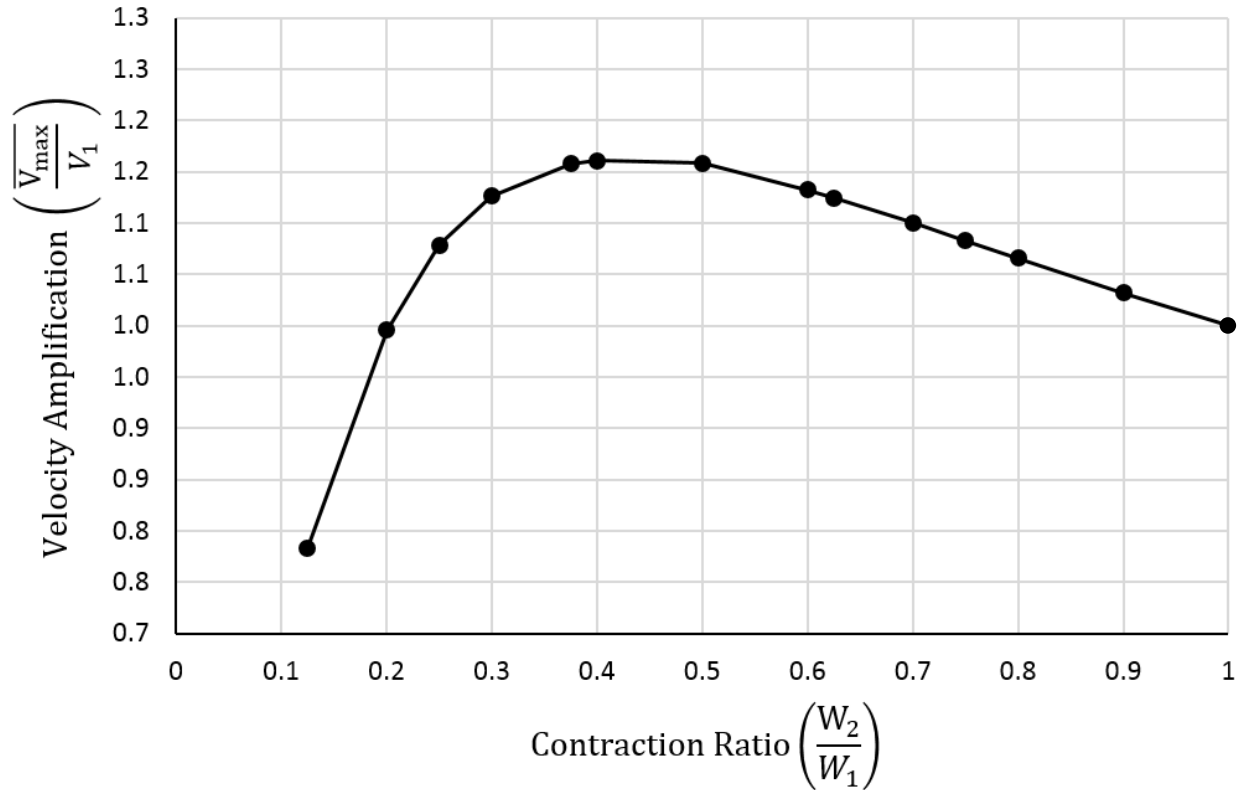


Figure 27: Velocity amplification versus contraction ratio, experiment set 1

Momentum is the product of the velocity and the mass flow rate. As such, one should expect maximum velocity amplification at a W_2/W_1 value where the laterally re-directed mass flow reaches a co-maximum with the conservation of velocity. As W_2/W_1 increases the amount of laterally redirected flow increases, however this redirection of flow is offset by a backwater effect and correspondingly lower velocities. Under the conditions used in the experiments, it is reasonable to expect for this maximization of momentum to occur within the middle range of contraction ratios.

Velocity amplification increased as W_2/W_1 increased from 0.125 to 0.4. As the severity of the contraction eased from a ratio of 0.125, the amount of flow redirection was reduced, thus alleviating backwater effects and increasing velocity.

As the contraction ratio increased from 0.4 to 0.9 the velocity amplification decreased gradually. Within the experiment set selected for Figure 27, the single location of peak velocity splits into two, and as the contraction became less severe, so too did the velocity amplification.

4.3.2. Influence of Bed Roughness on Velocity Amplification

Contraction ratio, W_2/W_1 , does not act alone to produce the effects of velocity amplification. Bed roughness also affects the degree of velocity amplification. However, it is not surprising that, as show in Figure 28, smoother channels resulted in more velocity amplification, while rougher channels resulted in less. This result can be attributed to the effect of roughness upon the momentum and energy expenditure necessary to redirect flow through the contraction transition.

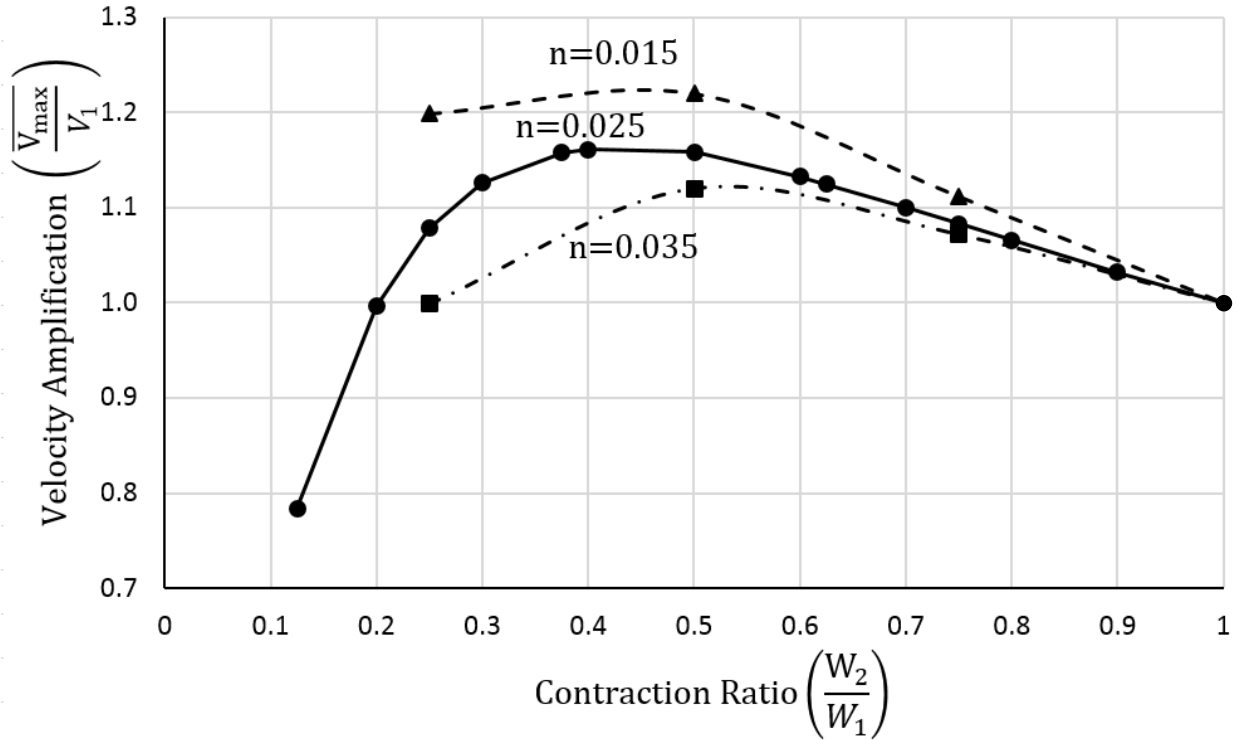


Figure 28: Velocity amplification vs contraction ratio with varying roughness

A simplified way of understanding this relationship can be expressed in the form of the simplified one-dimensional conservation of momentum St. Venant equation, shown in Eq. 4-1.

$$\frac{\delta V}{\delta t} + V \frac{\delta V}{\delta x} + g \frac{\delta h}{\delta x} = g(S_0 - S_f) \quad \text{Eq. 4-1}$$

The friction slope, S_f , is a function of bed roughness. As S_f increases, a corresponding decrease must occur on the left side of Eq. 4-1. In this case, as the downstream flow depth is fixed, the decrease is seen in the form of velocity.

4.3.3. Influence of Slope on Velocity Amplification

Contraction ratio, W_2/W_1 , and Manning's roughness coefficient, n , do not act alone to produce the effects of velocity amplification. Channel slope, S , also affects the degree of velocity amplification. However, it is not surprising that, as show in Figure 29, steeper channels result in higher $\overline{V_{max}}/V_1$ values, while less steep channels result in lower $\overline{V_{max}}/V_1$ values.

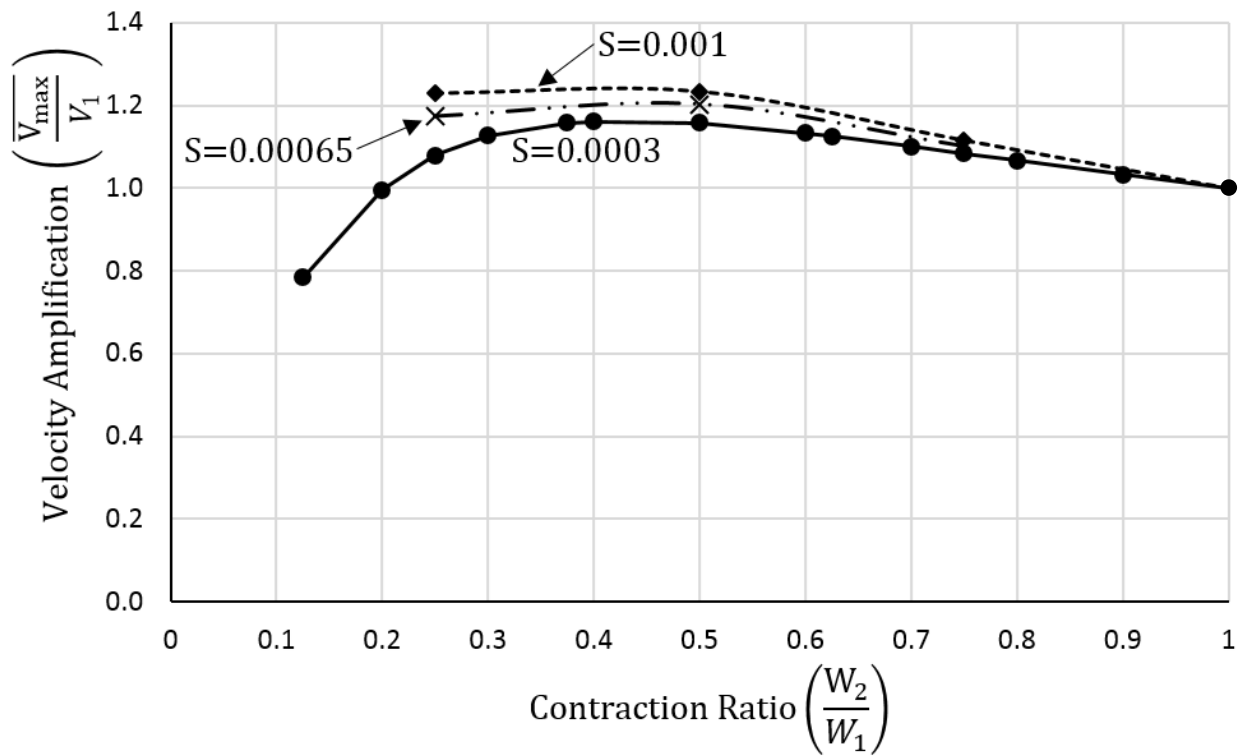


Figure 29: Velocity amplification versus contraction ratio with varying slope

The effect of slope, shown in Figure 29, could be largely due to the relative change in hydraulic radius. When a channel contracts there is a significant change in hydraulic radius. If the flow depth is taken to be identical in the contracted reach as in the un-contracted reach, the ratio of hydraulic radii, expressed as R_2/R_1 , is always less than one, indicating that there is a relative

increase in wetted perimeter per unit of flow area. If the slope of the channel is steepened, while all other variables are held constant, the flow depth will be decreased. A steeper slope results in a shallower normal depth of flow and, therefore, a smaller hydraulic radius. However, the ratio of hydraulic radii between the contracted and uncontracted sections in a steeper channel increases, reflecting a lesser degree of change in wetted perimeter per unit area.

A simplified way of understanding this relationship can be expressed in the form of the simplified one-dimensional conservation of momentum St. Venant equation, shown in Eq. 4-1. As the channel slope increases, a corresponding increase must occur on the left side of the equation. In this case, as the downstream flow depth is fixed, therefore the increase is seen in the form of velocity.

4.3.4. Influence of Transition Shape on Velocity Amplification

Having examined the influence of contraction ratio, roughness, and slope one must also acknowledge the influence of contraction transition shape. Figure 30 shows how velocity amplification varies with transition shape. Both the 45° full-bevel and the 45° half-bevel transition shapes resulted in slightly lower velocity amplification values. This shows that a more gradual transition shape results in lower values of velocity amplification by distributing flow redirection.

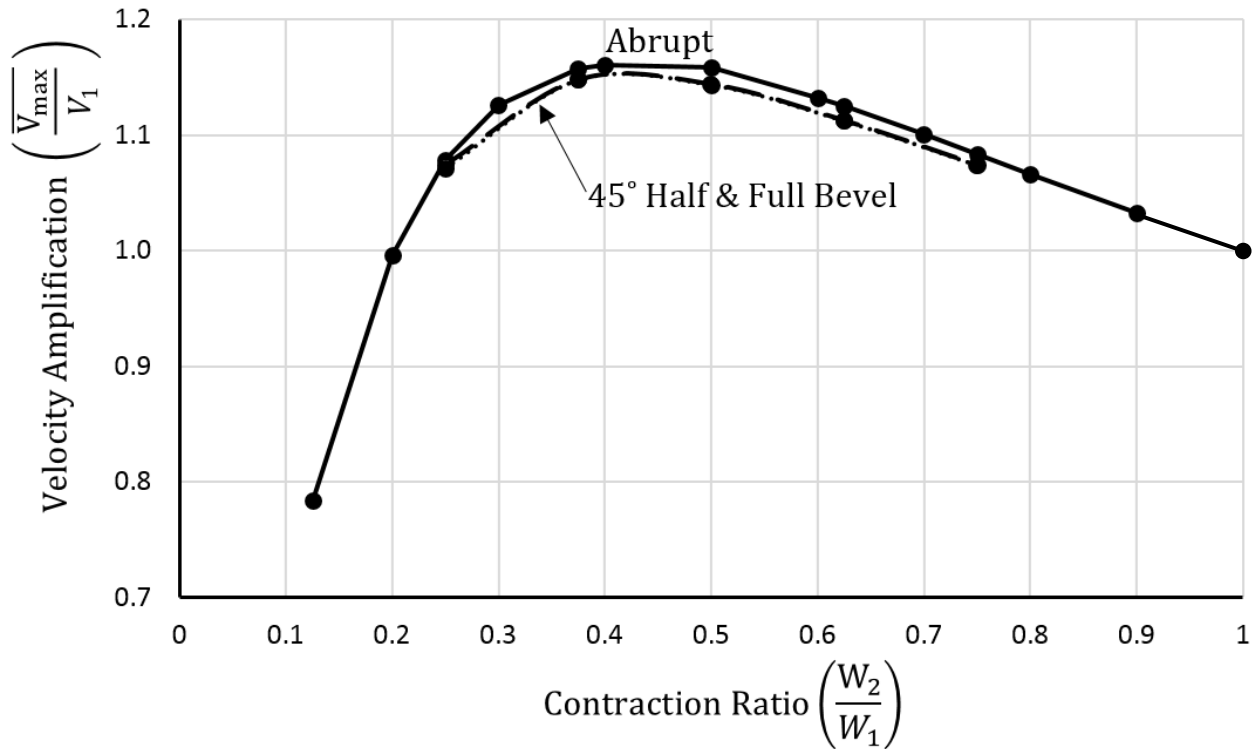


Figure 30: Velocity amplification versus contraction ratio with varying transition shape

One may notice that the full and half bevel shapes have nearly identical results. The difference between the two data sets of values is on average 0.0002 ± 0.00023 m/s, with the 45° half-bevel transition shape showing slightly higher cross-section average velocity values. This trend indicates that, while a beveled transition shape reduces velocity amplification, there is little difference between a full and a half bevel.

4.4. Variation in Flow Separation

Flow separation presents itself as an area of relatively steep gradient of velocity. Flow outside the area of separation races by while water inside moves downstream slowly, stagnates, or even moves upstream. In all simulation results flow separation presented itself in the form of velocity

field distortion. However, in many cases the region of separation was readily identified by velocities of zero within the channel and upstream velocities located on wall-ward side (e.g. a recirculating vortex). In these cases, the effective flow width could be measured as illustrated in Figure 15.

The root cause of flow separation is the conservation of lateral momentum resulting from the channel width contraction. Lateral momentum cannot be instantly re-directed downstream, rather some distance is required. As such, maximum lateral velocity may serve as a suitable proxy for lateral momentum and therefore flow separation. In all simulations, the maximum lateral velocity was recorded at the boundary inflection points of the contraction transition, immediately upstream of the contraction. The magnitude of lateral velocity entering the contraction serves as an indicator of velocity field distortion, because it directly influences the rotational speed of the flow-separation vortex within the contraction entrance

4.4.1. Influence of Contraction Ratio on Flow Separation

Flow separation varies greatly with W_2/W_1 , as shown in experiment set 1. When the $W_2/W_1 \geq 0.9$, although velocity field distortion is observable, no measurable flow separation was present in the simulation results. Likewise, when $W_2/W_1 \leq 0.3$, the velocity field distortion was evident, but no measurable flow separation seemed to occur. When $0.3 \geq W_2/W_1 \geq 0.9$, flow separation can be easily measured from the line dividing upstream from downstream velocities as shown in Figure 15. The effective flow widths resulting from these measurements are plotted in Figure 31.

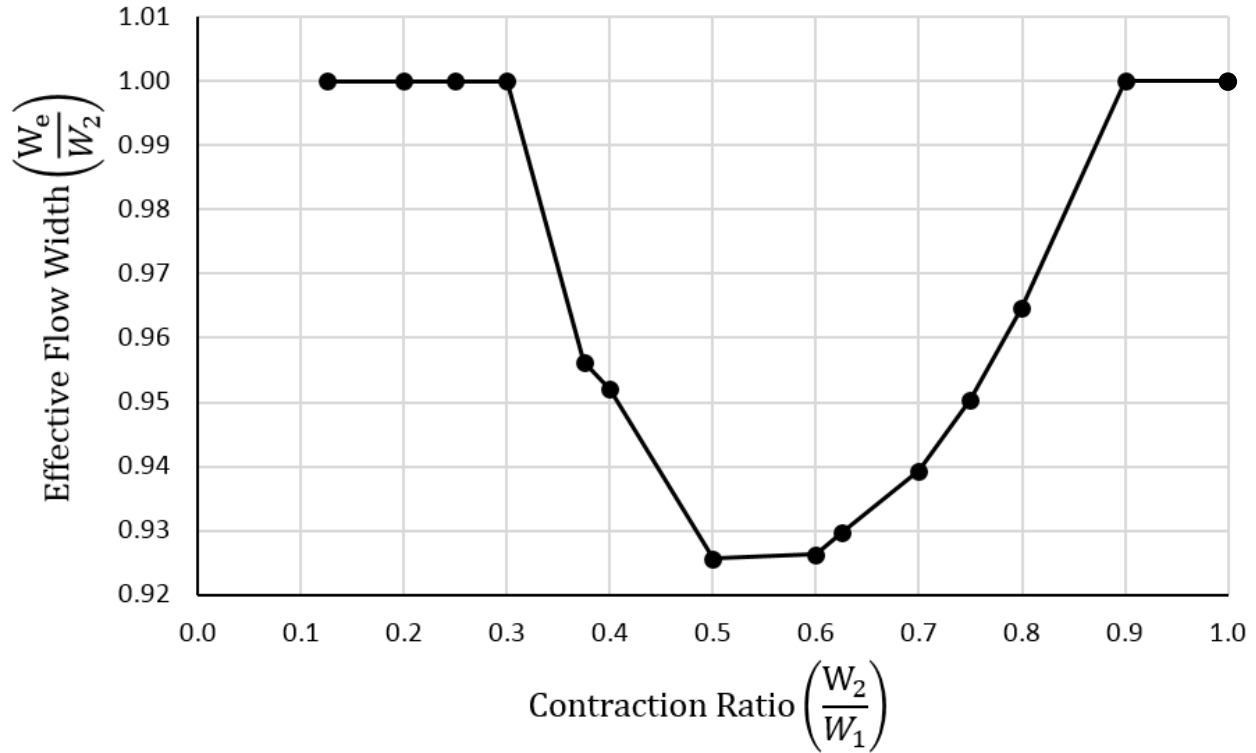


Figure 31: Effective flow width versus contraction ratio, for experiment set 1

As stated previously, conservation of lateral momentum, as necessitated by the geometry of the contraction, is the driving force behind flow separation. Momentum is the product of the velocity and the mass flow rate. As such, one should expect maximum lateral velocities at a contraction ratio where the laterally re-directed mass flow reaches a co-maximum with velocity. As the contraction ratio increases the amount of laterally redirected flow increases, however this redirection of flow is countered by a backwater effect and correspondingly lower velocities. Under the conditions used in the experiments, it is reasonable to expect for this maximization of transferred momentum to occur within the middle range of contraction ratios.

As shown in Figure 31, effective flow width reaches a minimum, while flow separation reaches a maximum, when $W_2/W_1=0.5$. Lateral velocity follows the same pattern and also reaches a maximum when $W_2/W_1=0.5$, as shown by Figure 32.

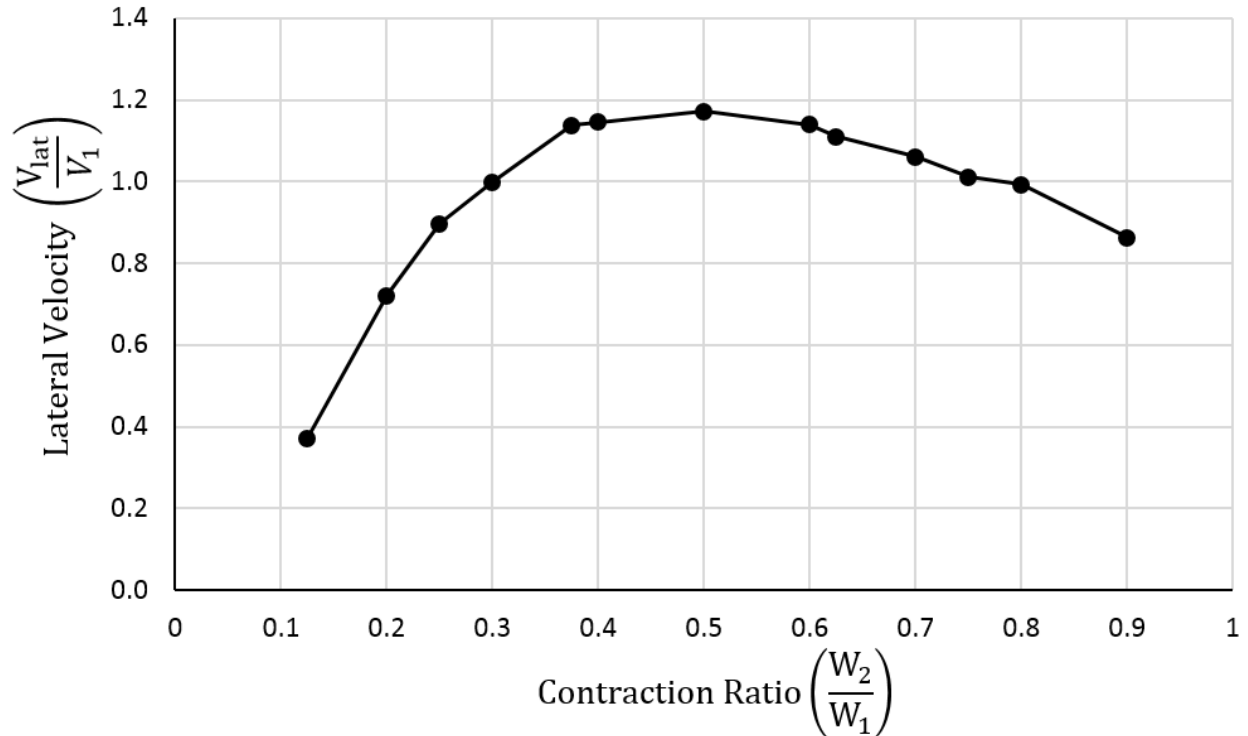


Figure 32: Maximum lateral velocity versus contraction ratio, for experiment set 1

4.4.2. Influence of Bed Roughness on Flow Separation

Based upon experiment sets one, two, and three, using three different Manning's n roughness values, roughness does not significantly change the contraction ratio at which effective flow width is at a minimum or lateral velocity is at a maximum. However, as with velocity amplification, roughness does change the magnitude of flow separation and lateral velocity.

Figure 33 shows how a change in bed roughness shifts the effective flow width versus contraction ratio curve, while Figure 34 shows how the maximum lateral velocity relationship is affected.

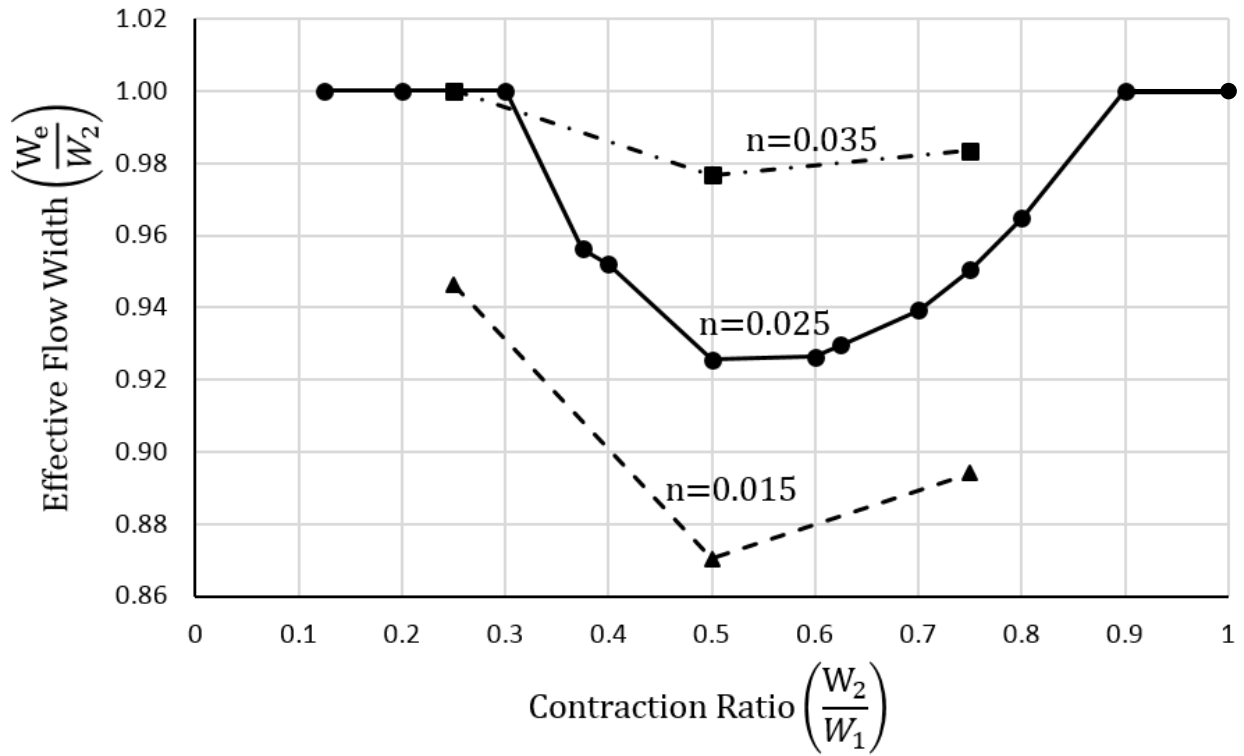


Figure 33: Effective flow width versus contraction ratio, with varying roughness

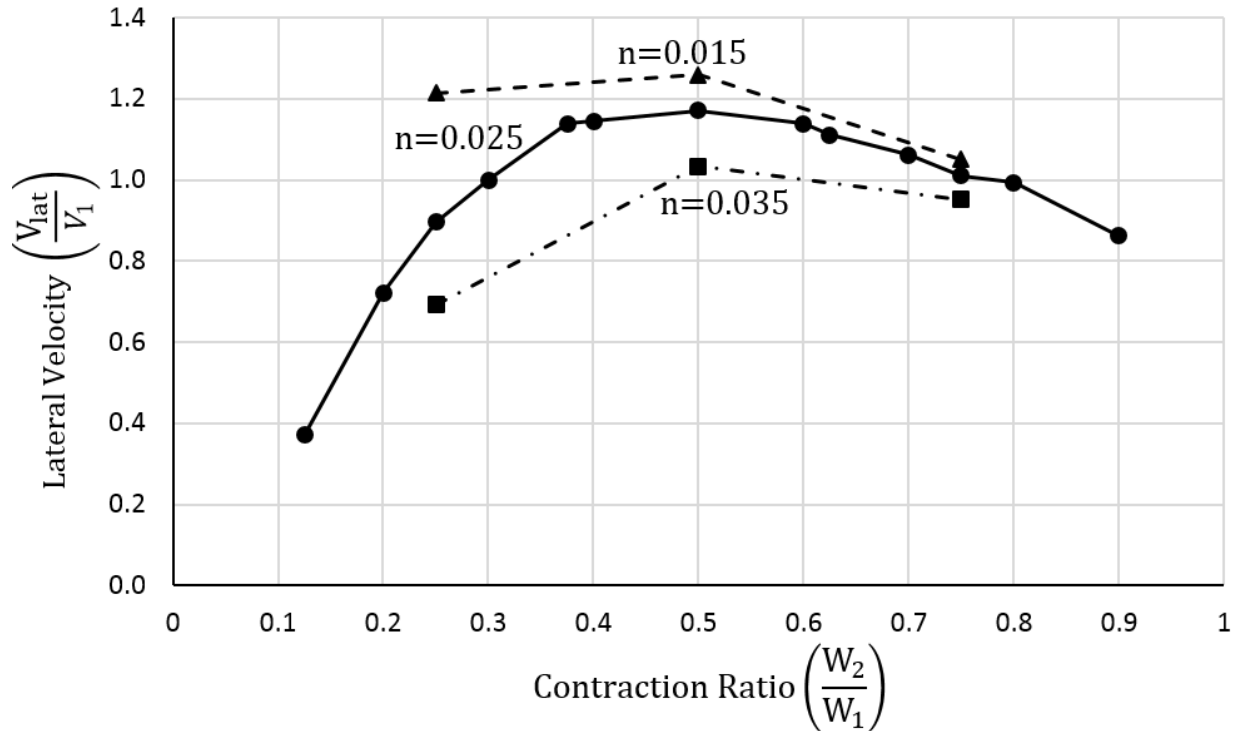


Figure 34: Maximum lateral velocity versus contraction ratio, with varying roughness

4.4.3. Influence of Slope on Flow Separation

Based upon experiment sets one, four, and five, using three different slope values, slope does not significantly change the contraction ratio at which effective flow width is at a minimum or lateral velocity is at a maximum. However, as with velocity amplification, slope does significantly change the magnitude of flow separation and lateral velocity. Figure 35 shows how a change in bed roughness shifts the effective flow width versus contraction ratio curve, while Figure 36 shows how the maximum lateral velocity relationship is affected.

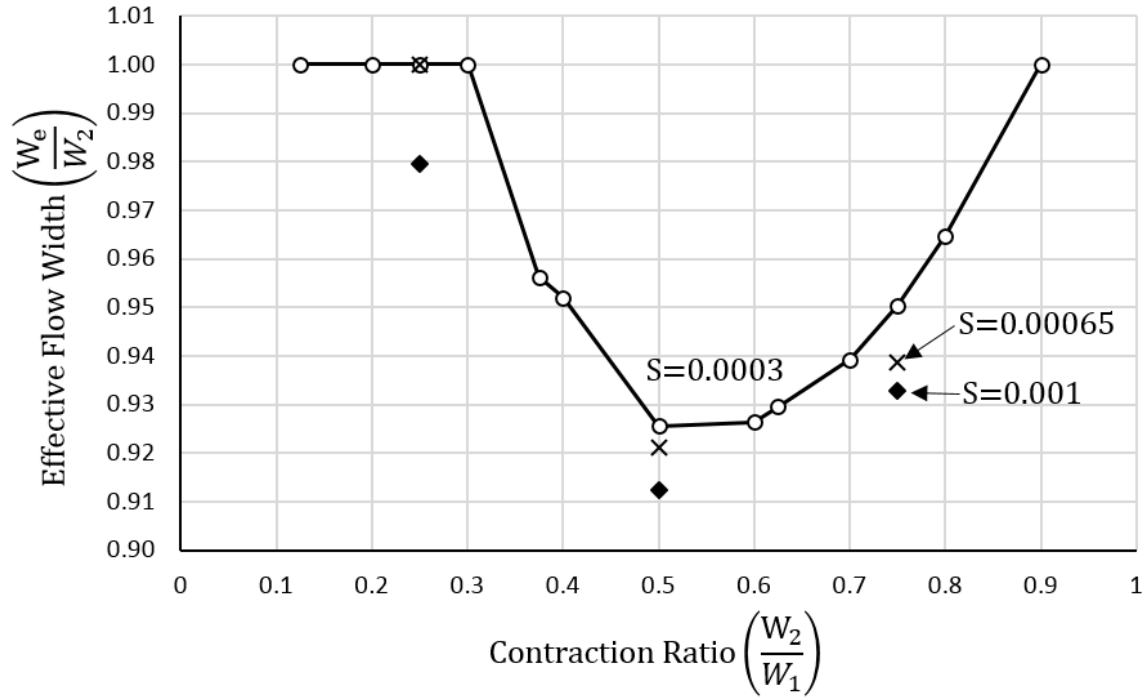


Figure 35: Effective flow width versus contraction ratio, with varying slope

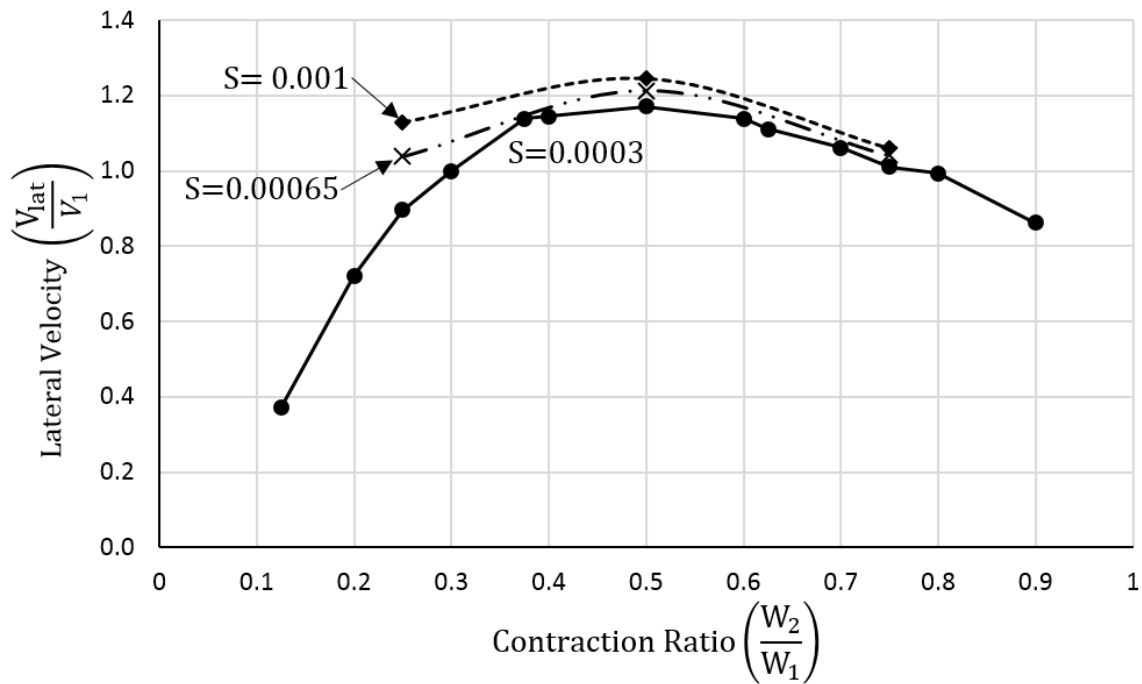


Figure 36: Maximum lateral velocity versus contraction ratio, with varying slope

4.4.4. Influence of Transition Shape on Flow Separation

Based upon experiment sets one, six, and seven, using one abrupt transition and two types of beveled transitions, transition shape changes the contraction ratio at which effective flow width is at a minimum or lateral velocity is at a maximum. In general, the 45° full-bevel and the 45° half-bevel transition shapes yielded lower maximum lateral velocities than the abrupt transition did, with the 45° half-bevel yielding slightly lower values than the 45° full-bevel. Figure 37 plots the observed maximum lateral velocities.

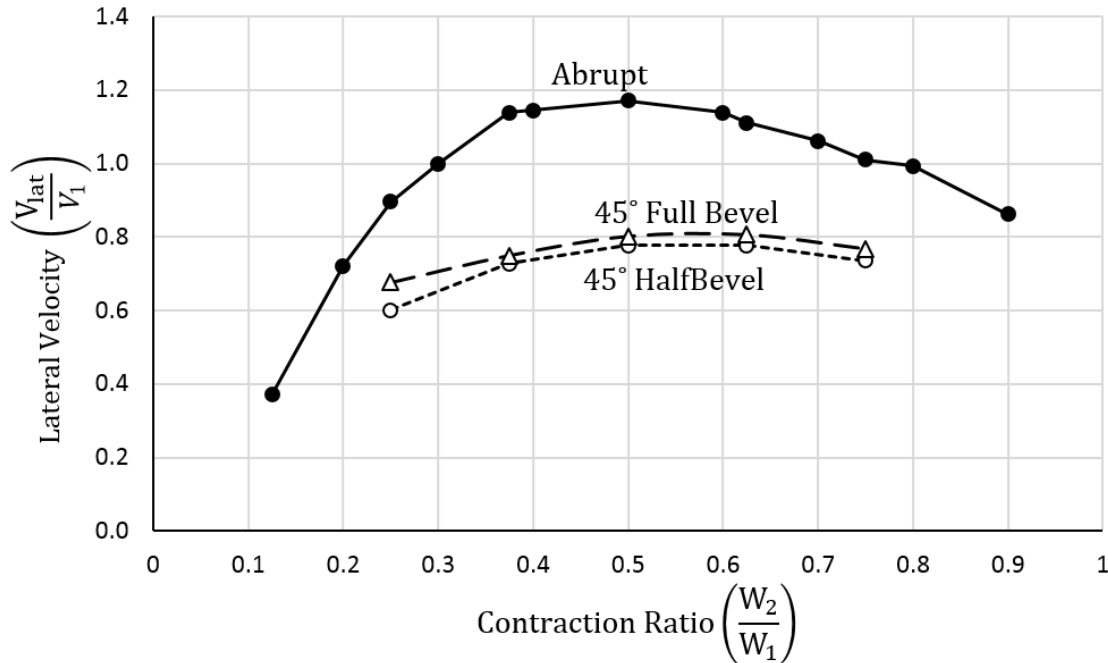


Figure 37: Maximum lateral velocity versus contraction ratio, with varying transition shape

The lower lateral velocity values shown in the experiment sets with bevel transition shapes may be explained by acknowledging the more gradual nature of flow re-direction. It is worth noting that none of the simulations with a bevel shaped transition had measurable flow separation.

However, velocity field distortion was still observable.

5. CONCLUSIONS AND RECOMENDATIONS

This study used a two-dimensional (2D) numerical model, SRH-2D, to investigate flow field characteristics associated with flow through open-channel contractions. The location, distribution, and relative magnitude of maximum velocity in a short contraction were examined. Each of the parameters studied is the result of the conservation of momentum as flow passes through the contraction. As such, the contraction ratio, W_2/W_1 , channel roughness, k , channel slope, S , and transition shape influence on how momentum is transferred through a contraction.

5.1. Conclusions

The following main conclusions resulted from this study:

- 1) The location of maximum velocity within the contraction varies with W_2/W_1 , and transition shape:
 - a) For abrupt transition contractions, the location of maximum velocity is symmetrically mirrored about the flume centerline for $W_2/W_1 \gtrsim 0.5$. However, when $W_2/W_1 \lesssim 0.5$, the maximum velocity occurs directly on the flume centerline; and,
 - b) For 45° full and half bevel transitions shapes where $W_2/W_1 \gtrsim 0.25$, the peak velocities are located precisely on the corners of the channel transition. When $W_2/W_1 \lesssim 0.25$ a single location of peak velocity occurred on the channel centerline.
- 2) Velocity uniformity, $V_{max} / \overline{V_{max}}$, varies with contraction ratio, W_2/W_1 , Slope, S , Manning's Roughness, n , and transition shape:

- a) For abrupt transitions, $V_{max} / \overline{V_{max}}$ reaches a maximum when $0.3 \lesssim W_2/W_1 \lesssim 0.6$ with variation within the velocity location transition range. Likewise, for abrupt transitions, the coefficient of velocity variation reached a maximum when $W_2/W_1 \cong 0.5$;
- b) An increase in Manning's roughness, n , resulted in a decrease in, $V_{max} / \overline{V_{max}}$;
- c) An increase in slope, S , resulted in an increase in, $V_{max} / \overline{V_{max}}$; and,
- d) 45° Full and half bevel transition shapes resulted in lower values of $V_{max} / \overline{V_{max}}$ than abrupt contractions when $W_2/W_1 \lesssim 0.5$. A 45° half-bevel transition shape resulted consistently lower values of $V_{max} / \overline{V_{max}}$ than a 45° full bevel transition shape.
- 3) Velocity amplification, $\overline{V_{max}} / V_1$ varies with contraction ratio, W_2/W_1 , Slope, S , Manning's Roughness, n , and transition shape:
- a) For all transition shapes studied, $\overline{V_{max}} / V_1$ reaches a maximum when $W_2/W_1 \cong 0.4$;
- b) An increase in Manning's roughness, n , resulted in a decrease in $\overline{V_{max}} / V_1$;
- c) An increase in slope, S , results in an increase in $\overline{V_{max}} / V_1$; and,
- d) Both 45° full and half-bevel transition shapes resulted in lower values of $\overline{V_{max}} / V_1$ than abrupt contractions, with very little difference between 45° full and half-bevel transition shapes.
- 4) Flow separation, as measured by minimum effective flow width, W_e/W_2 , and maximum later velocity, V_{lat}/V_1 , varies with contraction ratio, W_2/W_1 , Slope, S , Manning's Roughness, n , and transition shape:
- a) For abrupt transitions, effective flow width, W_e/W_2 , reaches a minimum and lateral velocity, V_{lat}/V_1 , reached a maximum when $W_2/W_1 \cong 0.5$. Meanwhile when $W_2/W_1 \lesssim 0.3$ or $W_2/W_1 \gtrsim 0.9$, despite visible velocity field distortion, no measurable flow separation was produced, therefore $W_e/W_2=100\%$;

- b) An increase in Manning's roughness, n , results in an increase in W_e/W_2 and a decrease in V_{lat}/V_1 ;
- c) An increase in slope, S , results in a decrease in W_e/W_2 and a an increase in V_{lat}/V_1 ; and,
- d) Both 45° full and half-bevel transition shapes produced results with no measurable flow separation. However, 45° full and half bevel transition shapes produced consistently lower values of V_{lat}/V_1 than abrupt contraction shapes, with a maximum value of V_{lat}/V_1 when $W_2/W_1 \cong 0.625$

This study shows that the flow field within a contraction is complex and dependent upon all of the physical and hydraulic conditions prevailing in the contraction itself. Ultimately, the unique combination of these conditions affect the process through which flow momentum is transferred to flow passing through the contraction, thus resulting in the observed flow field.

The insights this study presents using the leading 2D numerical model, SRH-2D, applied to approach flows of aspect ratios (width to depth ratios) comparable to many natural open channels, aids engineering practitioners. The results indicate how each contraction parameter, mentioned in Eqs. (2.4) - (2.6), influences contraction flow fields in open channels. While these insights can be useful, it is important to remember that the results of this study are foremost a parametric comparison, not a set of predictive results. From an application point of view, this fact means that a practitioner can expect to alter the magnitudes of flow-field features by adjusting the contraction parameters in a manner similar as done for this study. For instance, the results will differ if the flow rate, or downstream depth were altered. Both of these factors will have a significant influence on the transfer of momentum into and through the contraction.

Additionally, as is well-known in numerical modeling, the resolution and configuration of the mesh of the numerical model will also change the flow field simulation results. These alterations will be most apparent when examining flow turbulence. The mesh resolution must be sufficient to resolve the 2D turbulence structures. The practitioner must balance the importance of modeling turbulent flow patterns with the practical limitations of mesh resolution and computational time.

5.2. Recommendations

The insights drawn from the present 2D numerical model are useful for explaining how scour develops in open-channel contractions. However, these insights are limited to the flow characteristics of a rigid flat-bed system. Therefore, it is recommended that future studies consider:

1. Using this study's findings to help explain how contraction scour develops in a contraction formed with an erodible bed; and,
2. Once equilibrium contraction scour has developed, determine how the flow field is affected.

We continue to learn more about the hydraulics and scour processes associated with contractions each day, but full understanding of hydraulics and sediment transport has not yet been achieved. In the meanwhile, engineers must continue to design and analyze channel contractions. It is recommended that designers continue to advance their methods with the most comprehensive analysis tools practicable, which now includes two-dimensional numerical modeling.

REFERENCES

- Arneson, L.A., Zevenbergen, L.W., Lagasse, P.F., and Clopper, P.E., (2012). "Evaluation of Scour at Bridges," Fifth Edition, Federal Highway Administration, Report FHWA-HIF-12-003, Hydraulic Engineering Circular No. 18, U.S. Department of Transportation, Washington, D.C.
- Chaudhry, M. H. (2008). Open-channel flow. Springer Science Business Media, New York.
- Chow, V. T. (1959). Open-channel hydraulics. McGraw-Hill, New York.
- Chrisohoides, A., Sotiropoulos, F., and Sturm, T. W. (2003). Coherent structures in flat-bed abutment flow: Computational fluid dynamics simulations and experiments. *Journal of Hydraulic Engineering*, 129(3), 177–186.
- FHWA. (2012). Evaluating Scour at Bridges, Federal Highway Admin. Publication FHWA HIF-12-003, Hydraulic Engineering Circular No. 18, Washington D.C. (Authored by Arneson, L.A., Zevenbergen, L.W. Lagasse, P.F. and Clopper, P.E.)
- Formica, G. (1955) Esperienze preliminari sulle perdite di carico nei canali, dovute a cambiamenti di sezione. *L'Energia elettrica*. Milano, Vol.32, No.7, 554-568.
- Henderson, F.M. (1966) Open channel flow. The Macmillan Company, New York.
- Julien, P. Y. (2010). Erosion and sedimentation. Cambridge University Press, Cambridge.
- Koken, M. (2017). Coherent Structures at Different Contraction Ratios Caused by Two Spill-Through Abutments. *Journal of Hydraulic Research*, 49(6), 736–743.
- Lai, Y.G. (2008). SRH-2D Version 2: Theory and User's Manual. U.S. Department of the Interior Bureau of Reclamation Technical Service Center.
- Lai, Y.G. (2010). Two-Dimensional Depth-Averaged Flow Modeling with an Unstructured Hybrid Mesh. *Journal of Hydraulic Engineering*, 136(1), 12-23.
- Lai, Y.G. & Greimann, Blair P. (2010) Predicting contraction scour with a two-dimensional depth-averaged model, *Journal of Hydraulic Research*, 48:3, 383-387.
- Marek, M., Dittrich, A. (2004). 3D numerical calculations of the flow in an open-channel consisting of an expansion and contraction. 6th Intl. Conf. Hydro-Science and Engineering, Brisbane, Australia.

- Kara, S., Stoesser, T., Sturm, T. W., & Mulahasan, S. (2014). Flow dynamics through a submerged bridge opening with overtopping. *Journal of Hydraulic Research*, 53(2), 186-195.
- Rodi, W. (1993). "Turbulence models and their application in hydraulics," 3rd Ed., IAHR Monograph, Balkema, Rotterdam, The Netherlands.
- Sturm, T. W. (2001). Open channel hydraulics. McGraw-Hill, Boston.
- Weise, S. (2002). Verifikation eines zweidimensionalen Feststofftransportmodells anhand von hydraulischen Versuchen. Diplomarbeit. Fachhochschule für Technik, Wirtschaft und Kultur, Leipzig, Germany.

APPENDIX A: SIMULATION RESULTS, DATA SUMMARY TABLE

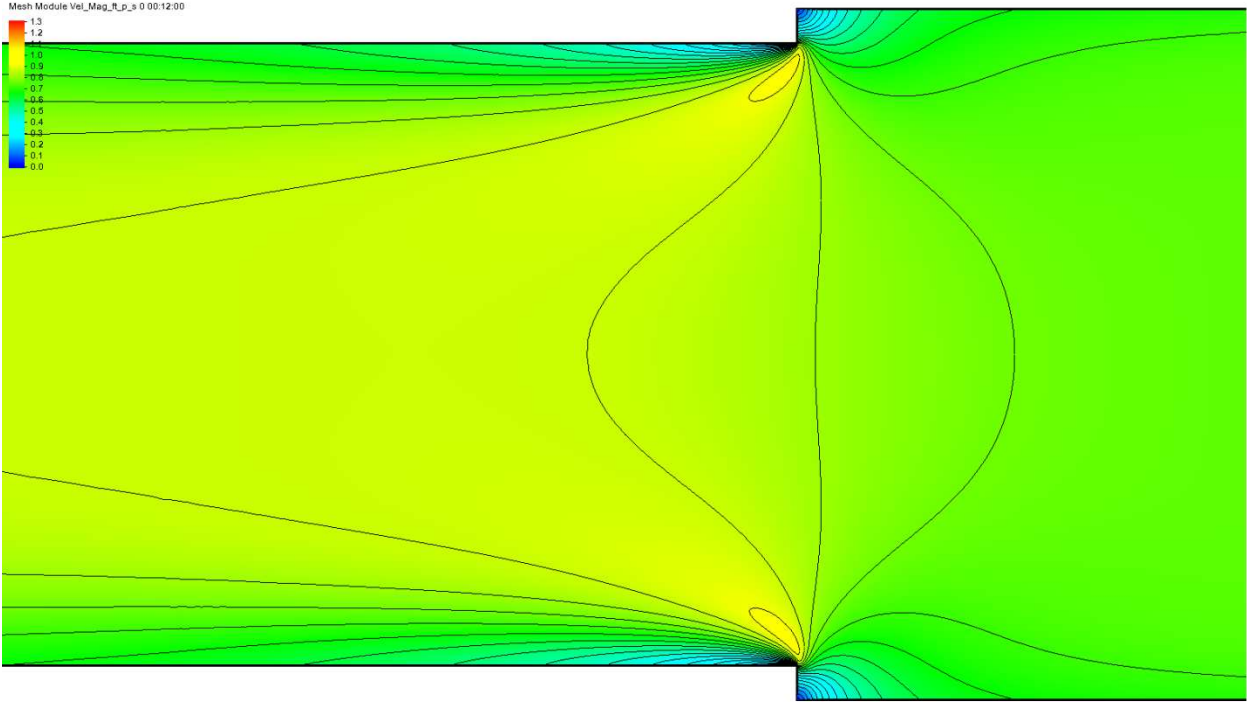
Ex. Set #	W_2/W_1	Shape	n	S	V_{max} m/s	\bar{V}_{max} m/s	X_{max} m	O_{max} m	V_{lat} m/s	W_e m
1	0.125	Abrupt	0.025	0.0003	0.220	0.614	0.014	0.030	0.089	0.305
	0.2	Abrupt	0.025	0.0003	0.300	0.781	0.027	0.122	0.172	0.488
	0.25	Abrupt	0.025	0.0003	0.332	0.846	0.034	0.213	0.214	0.610
	0.3	Abrupt	0.025	0.0003	0.348	0.883	0.040	0.305	0.239	0.732
	0.375	Abrupt	0.025	0.0003	0.355	0.908	0.046	0.427	0.272	0.874
	0.4	Abrupt	0.025	0.0003	0.354	0.910	0.048	0.472	0.274	0.929
	0.5	Abrupt	0.025	0.0003	0.349	0.908	0.052	0.228	0.280	1.128
	0.6	Abrupt	0.025	0.0003	0.344	0.888	0.056	0.199	0.272	1.355
	0.625	Abrupt	0.025	0.0003	0.341	0.882	0.056	0.196	0.265	1.417
	0.7	Abrupt	0.025	0.0003	0.329	0.863	0.057	0.176	0.254	1.603
0.75	Abrupt	0.025	0.0003	0.319	0.849	0.057	0.146	0.242	1.738	
0.8	Abrupt	0.025	0.0003	0.308	0.836	0.056	0.101	0.237	1.882	
0.9	Abrupt	0.025	0.0003	0.281	0.809	0.054	0.030	0.206	2.195	
2	0.25	Abrupt	0.015	0.0003	0.518	1.301	0.000	0.290	0.402	0.577
	0.5	Abrupt	0.015	0.0003	0.553	1.324	0.000	0.397	0.416	1.061
	0.75	Abrupt	0.015	0.0003	0.481	1.206	0.000	0.552	0.347	1.635
3	0.25	Abrupt	0.035	0.0003	0.240	0.630	0.000	0.152	0.133	0.610
	0.5	Abrupt	0.035	0.0003	0.267	0.706	0.000	0.579	0.199	1.191
	0.75	Abrupt	0.035	0.0003	0.242	0.676	0.000	0.058	0.183	1.799
4	0.25	Abrupt	0.025	0.00065	0.464	1.177	0.000	0.229	0.318	0.610
	0.5	Abrupt	0.025	0.00065	0.469	1.206	0.000	0.228	0.371	1.123
	0.75	Abrupt	0.025	0.00065	0.421	1.105	0.000	0.202	0.318	1.717
5	0.25	Abrupt	0.025	0.001	0.557	1.412	0.074	0.259	0.396	0.597
	0.5	Abrupt	0.025	0.001	0.556	1.417	0.104	0.246	0.437	1.113
	0.75	Abrupt	0.025	0.001	0.493	1.282	0.108	0.228	0.371	1.706
6	0.25	45° Half Bevel	0.025	0.0003	0.289	0.842	0.000	0.701	0.144	0.610
	0.375	45° Half Bevel	0.025	0.0003	0.310	0.900	0.000	0.381	0.174	0.914
	0.5	45° Half Bevel	0.025	0.0003	0.329	0.897	0.000	0.305	0.186	1.219
	0.625	45° Half Bevel	0.025	0.0003	0.329	0.873	0.000	0.229	0.186	1.524
	0.75	45° Half Bevel	0.025	0.0003	0.317	0.842	0.000	0.152	0.176	1.829
7	0.25	45° Full Bevel	0.025	0.0003	0.295	0.840	0.000	1.169	0.162	0.610
	0.375	45° Full Bevel	0.025	0.0003	0.315	0.900	0.000	0.762	0.179	0.914
	0.5	45° Full Bevel	0.025	0.0003	0.334	0.897	0.000	0.610	0.192	1.219
	0.625	45° Full Bevel	0.025	0.0003	0.340	0.872	0.000	0.457	0.193	1.524
	0.75	45° Full Bevel	0.025	0.0003	0.329	0.842	0.000	0.305	0.183	1.829

APPENDIX B: SIMULATION RESULTS VELOCITY MAGNITUDE PLOTS

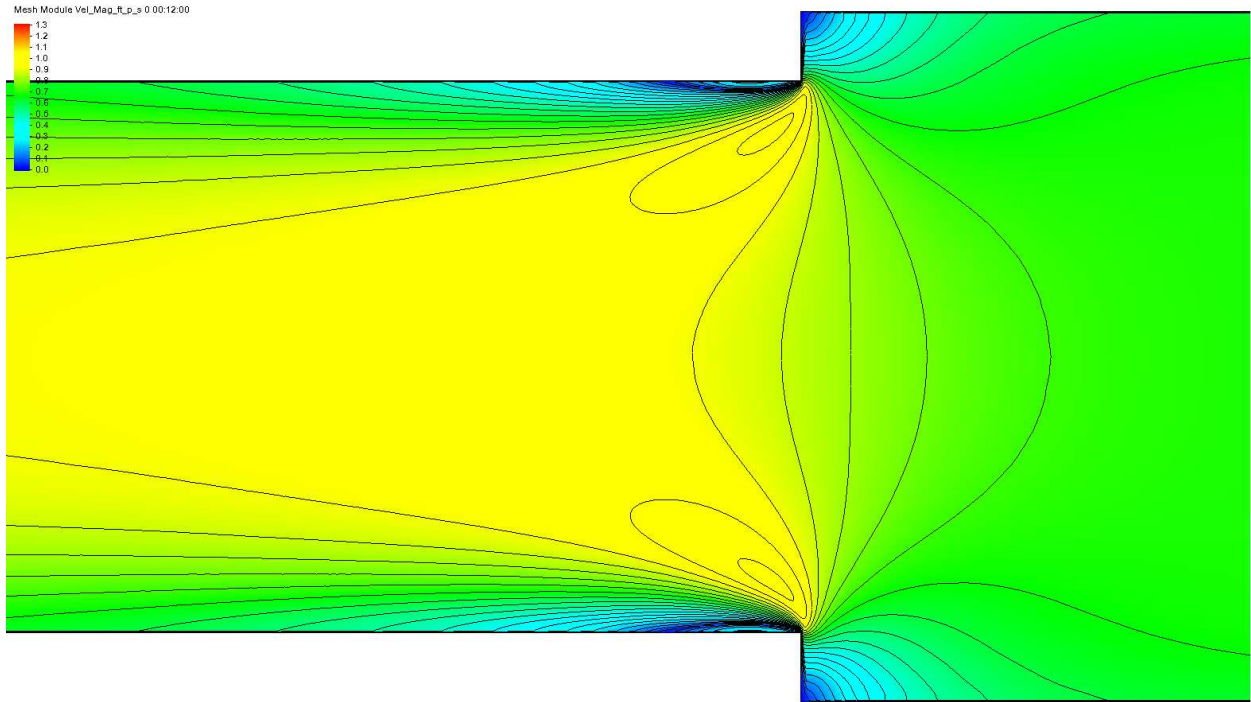
The following velocity magnitude plots present the results from the numerical models.

Experiment Set 1

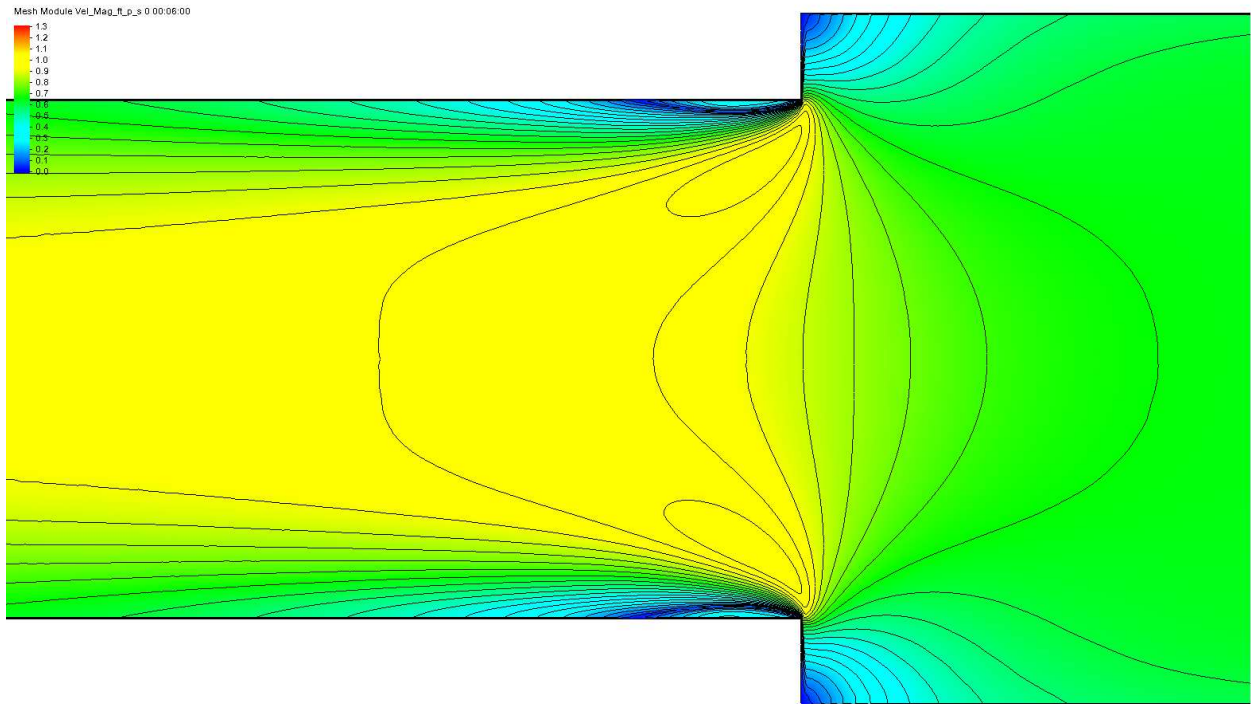
$W2/W1 = 0.9$, $W2 = 7.2\text{ft}$, $Q = 5\text{cfs}$, $S = 0.0003$, $n = 0.025$, Abrupt



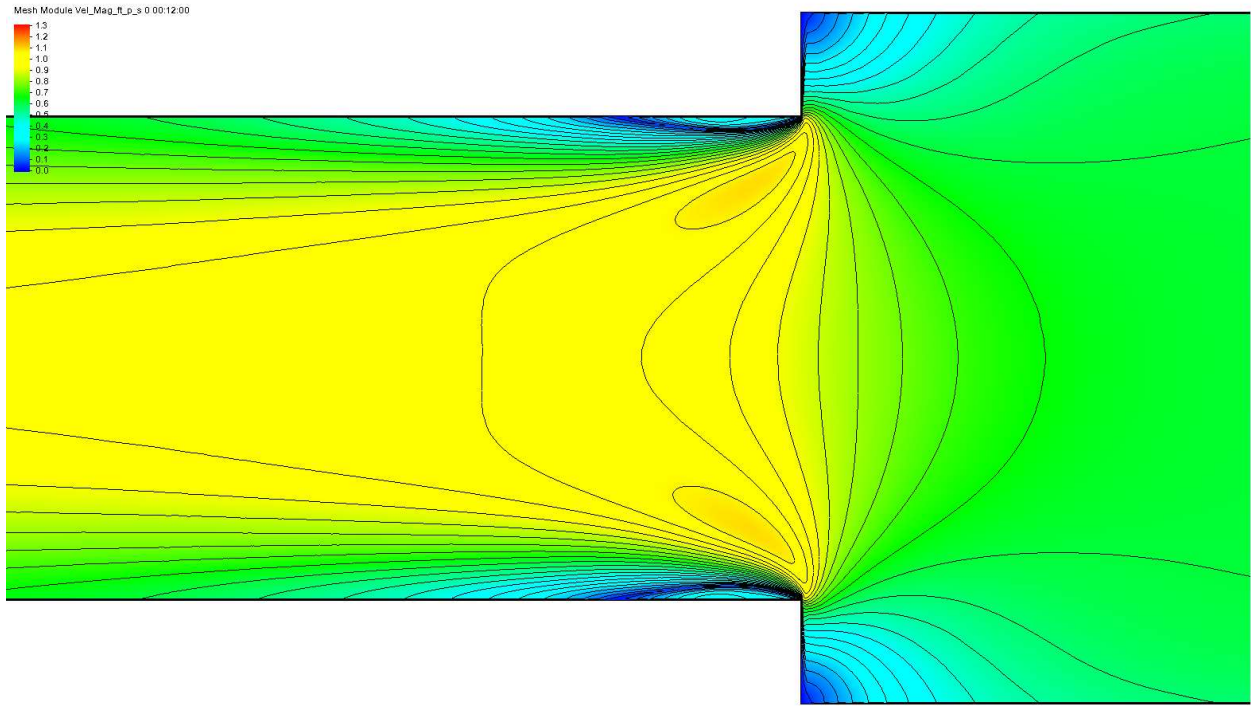
$W2/W1 = 0.8$, $W2 = 6.4\text{ft}$, $Q = 5\text{cfs}$, $S = 0.0003$, $n = 0.025$, Abrupt



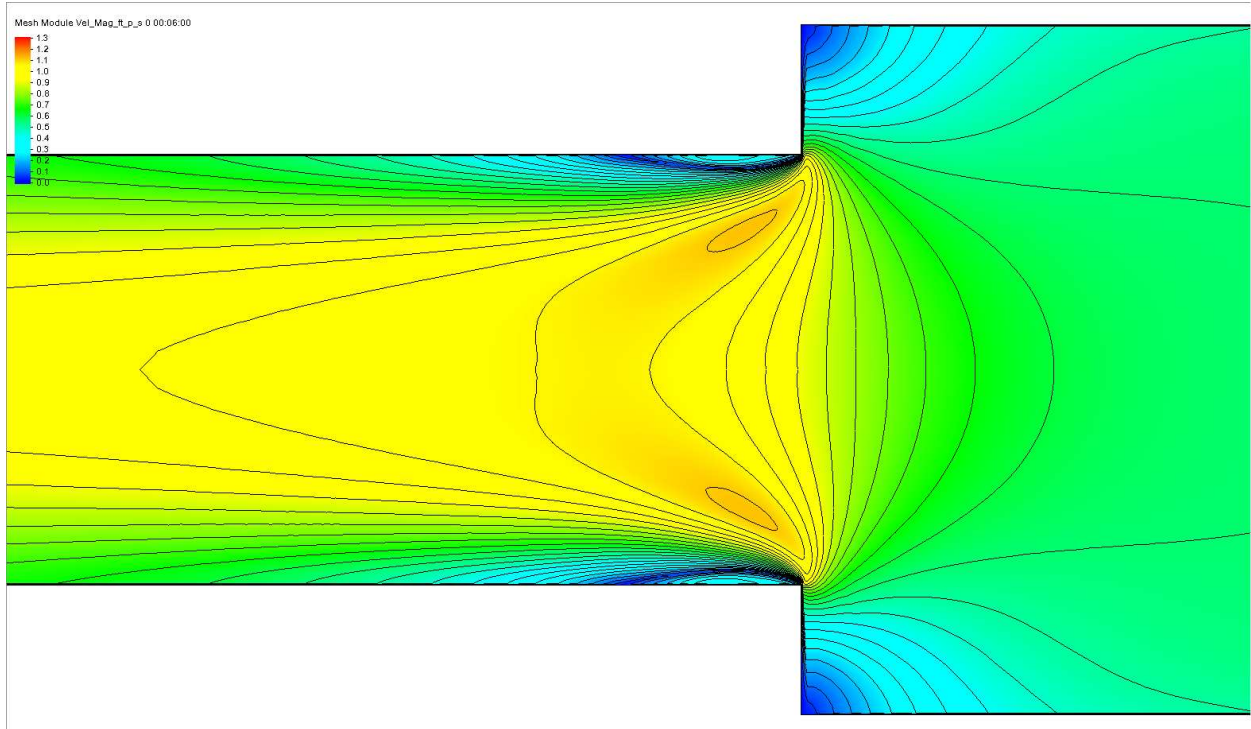
$W2/W1 = 0.75$, $W2 = 6\text{ft}$, $Q = 5\text{cfs}$, $S = 0.0003$, $n = 0.025$, Abrupt



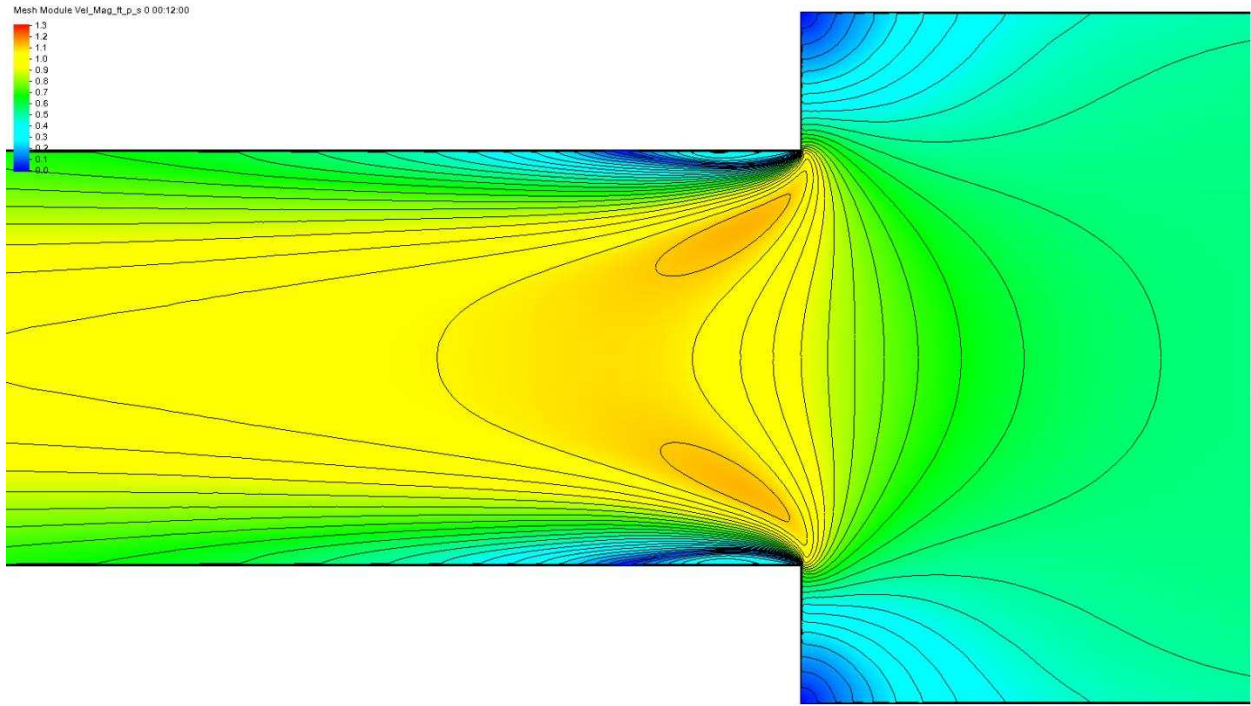
$W2/W1 = 0.7$, $W2 = 5.6\text{ft}$, $Q = 5\text{cfs}$, $S = 0.0003$, $n = 0.025$, Abrupt



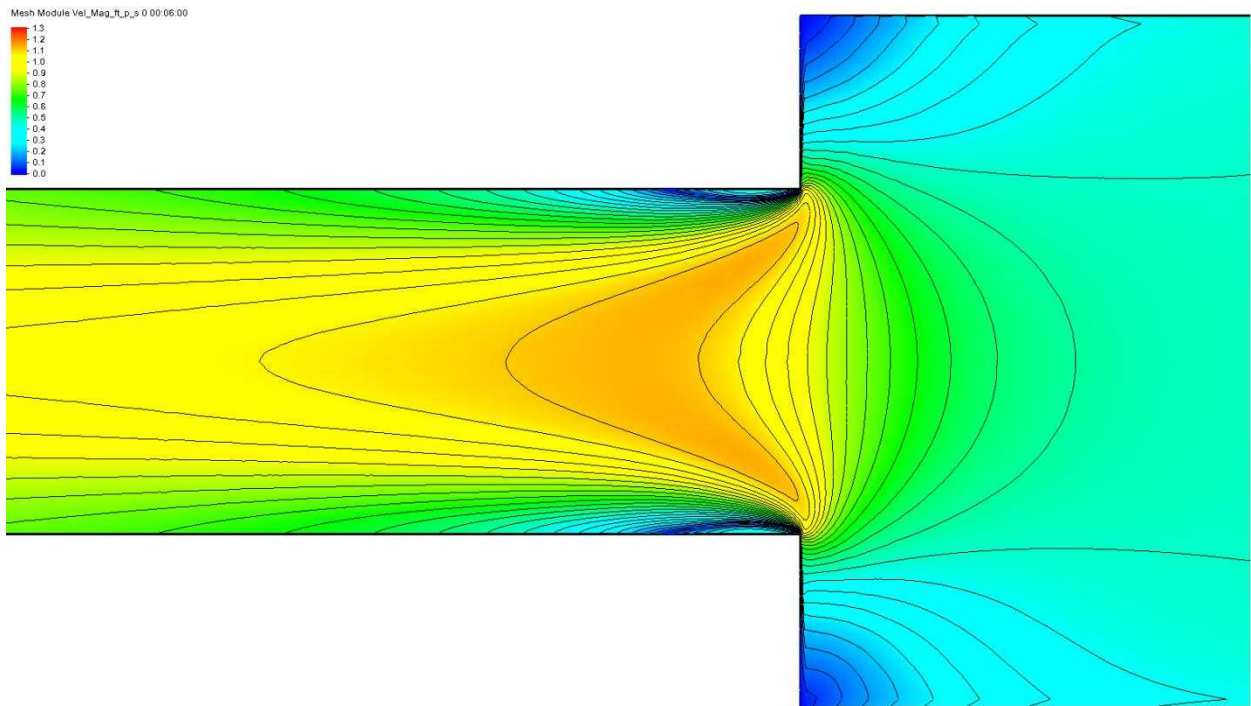
$W2/W1 = 0.625$, $W2 = 5\text{ft}$, $Q = 5\text{cfs}$, $S = 0.0003$, $n = 0.025$, Abrupt



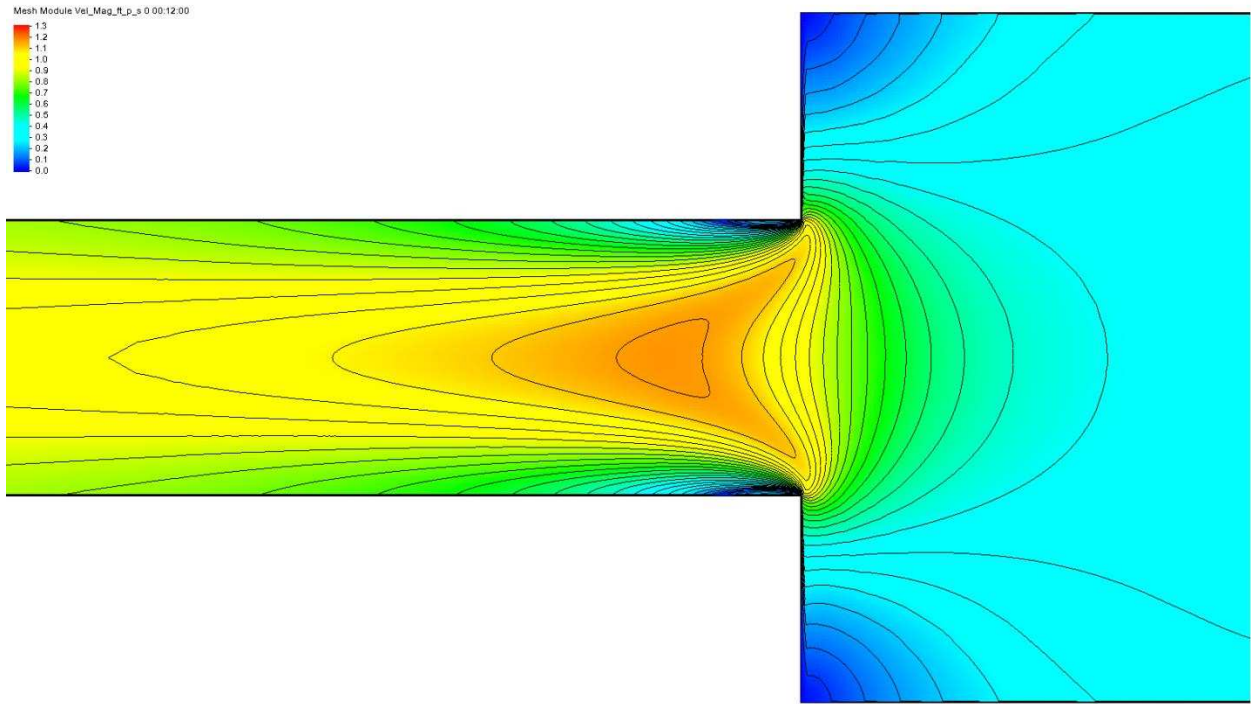
$W2/W1 = 0.6$, $W2 = 4.8\text{ft}$, $Q = 5\text{cfs}$, $S = 0.0003$, $n = 0.025$, Abrupt



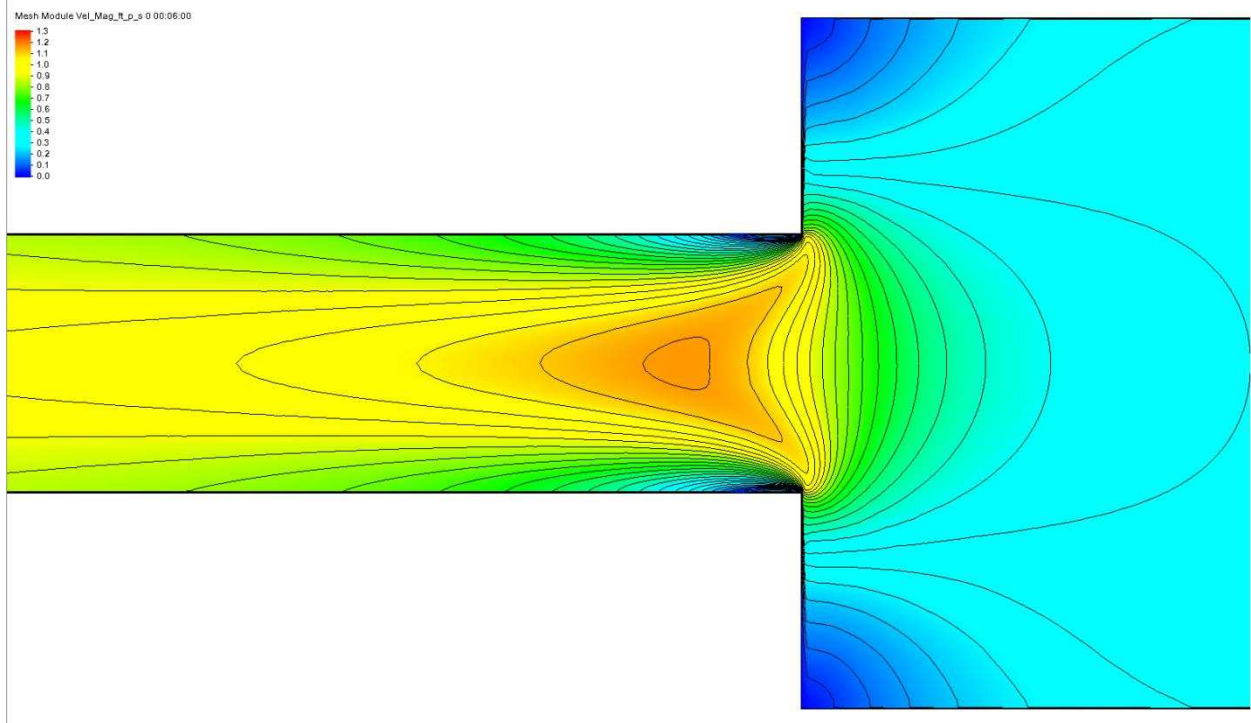
$W2/W1 = 0.5$, $W2 = 4\text{ft}$, $Q = 5\text{cfs}$, $S = 0.0003$, $n = 0.025$, Abrupt



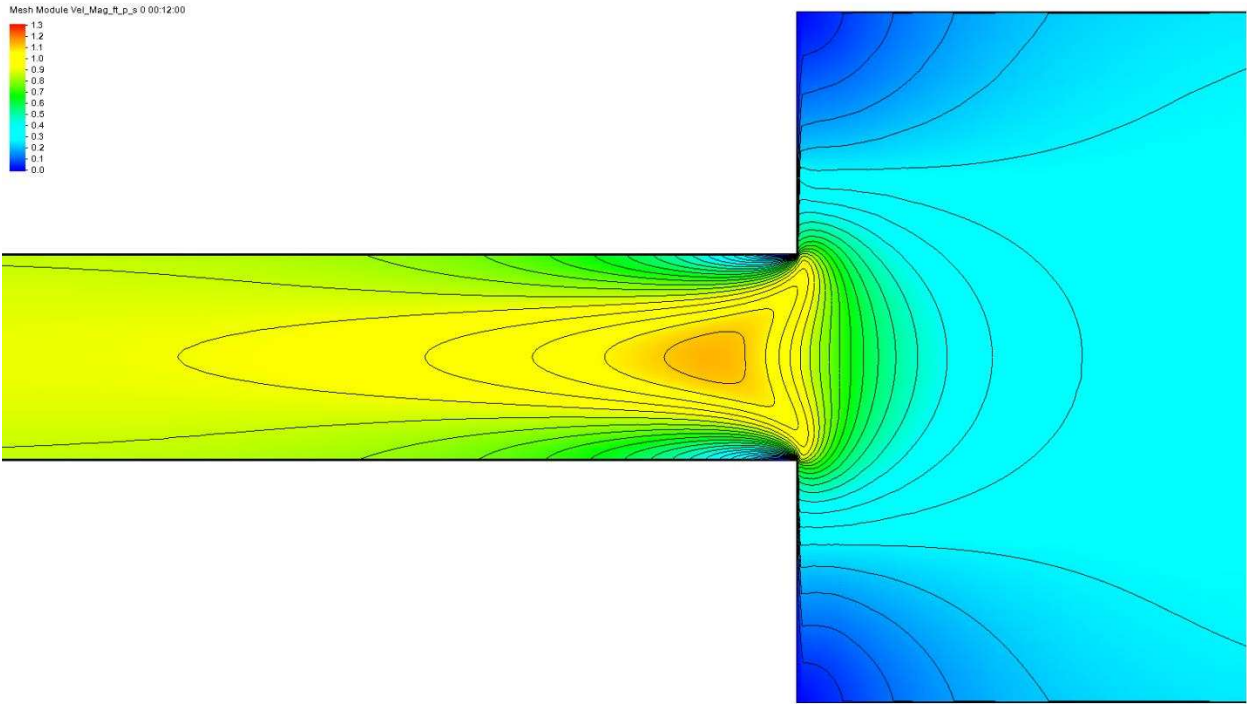
$W2/W1 = 0.4$, $W2 = 3.2\text{ft}$, $Q = 5\text{cfs}$, $S = 0.0003$, $n = 0.025$, Abrupt



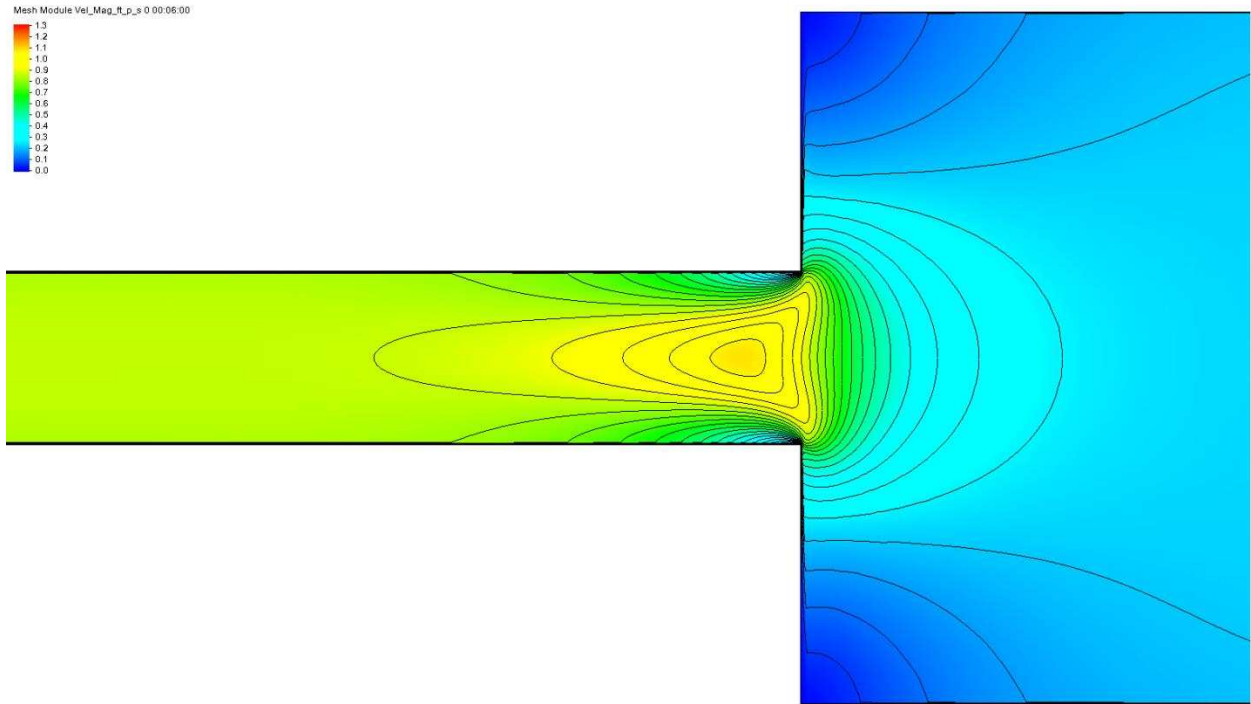
$W2/W1 = 0.375$, $W2 = 3\text{ft}$, $Q = 5\text{cfs}$, $S = 0.0003$, $n = 0.025$, Abrupt



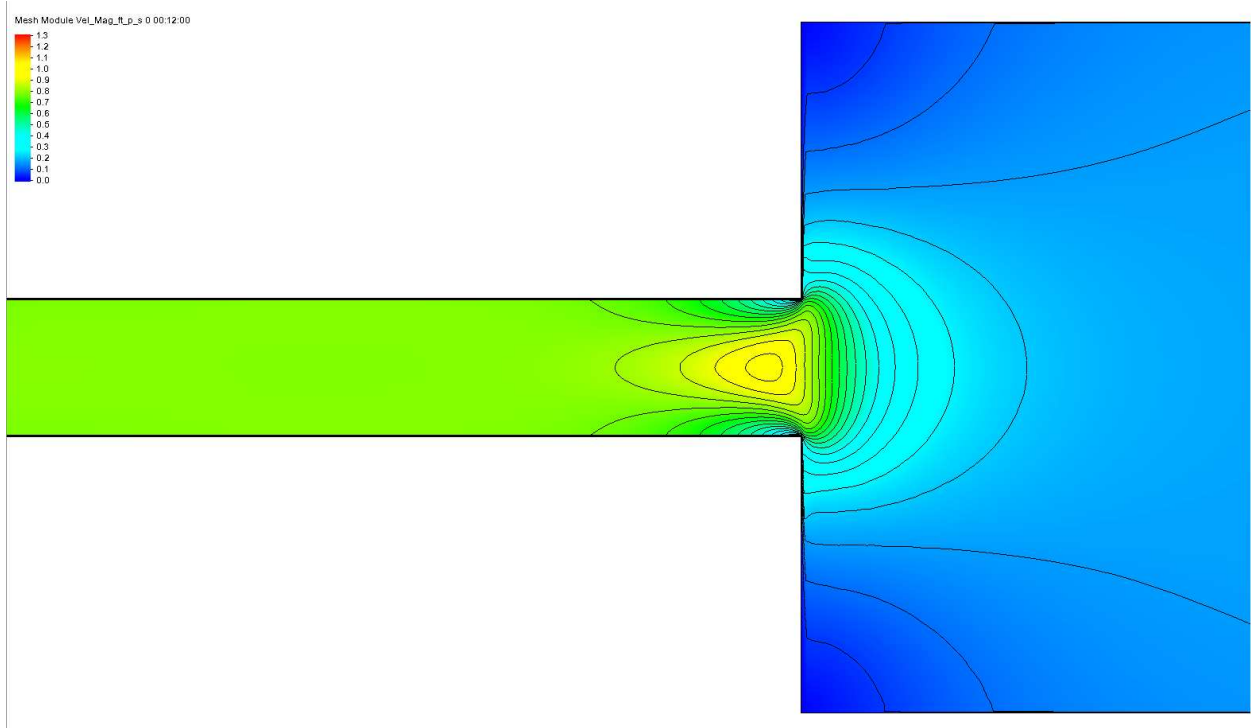
W2/W1= 0.3, W2=2.4ft, Q=5cfs, S=0.0003, n=0.025, Abrupt



$W2/W1 = 0.25$, $W2 = 2\text{ft}$, $Q = 5\text{cfs}$, $S = 0.0003$, $n = 0.025$, Abrupt

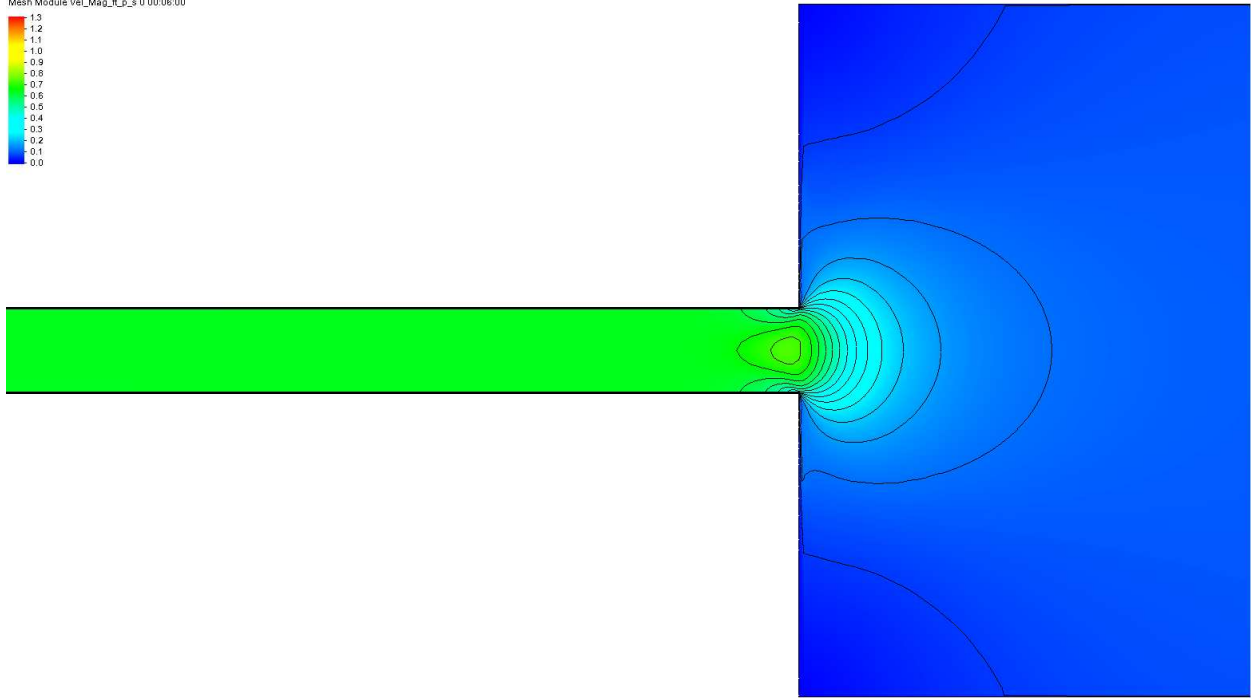
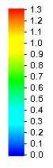


$W2/W1 = 0.2$, $W2 = 1.6\text{ft}$, $Q = 5\text{cfs}$, $S = 0.0003$, $n = 0.025$, Abrupt



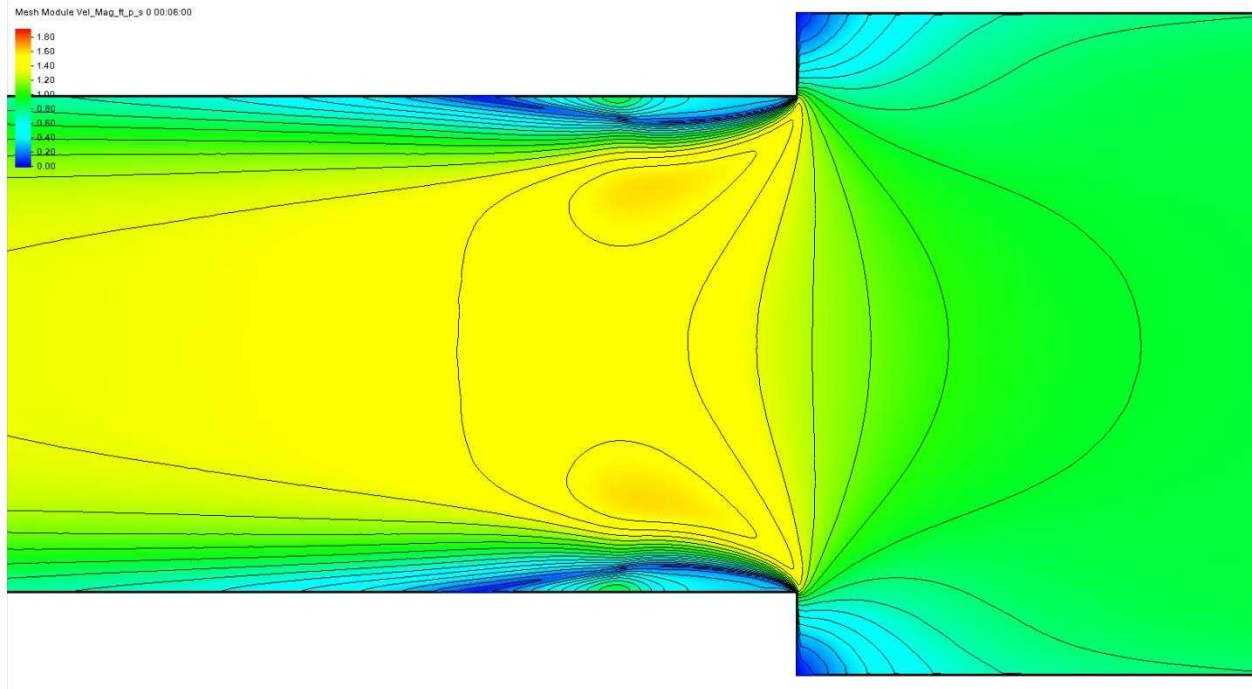
$W2/W1 = 0.125$, $W2 = 1\text{ft}$, $Q = 5\text{cfs}$, $S = 0.0003$, $n = 0.025$, Abrupt

Mesh Module Vel_Mag_T_P_s 0 00:06:00

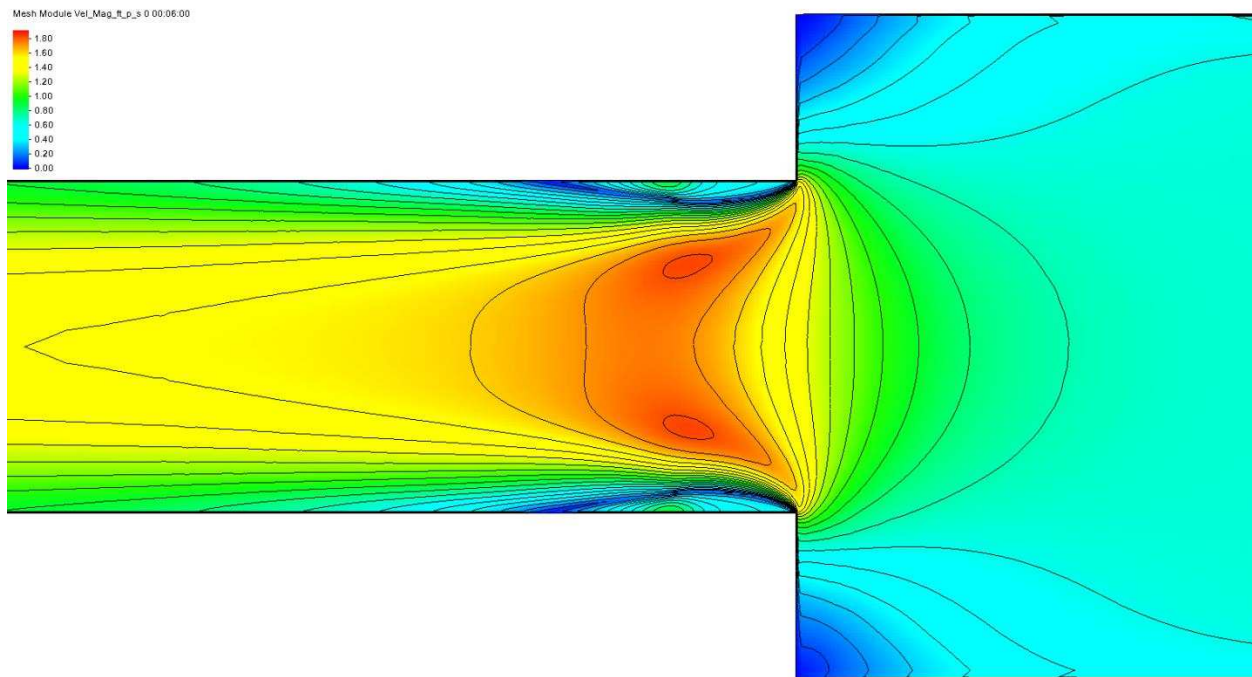


Experiment Set 2

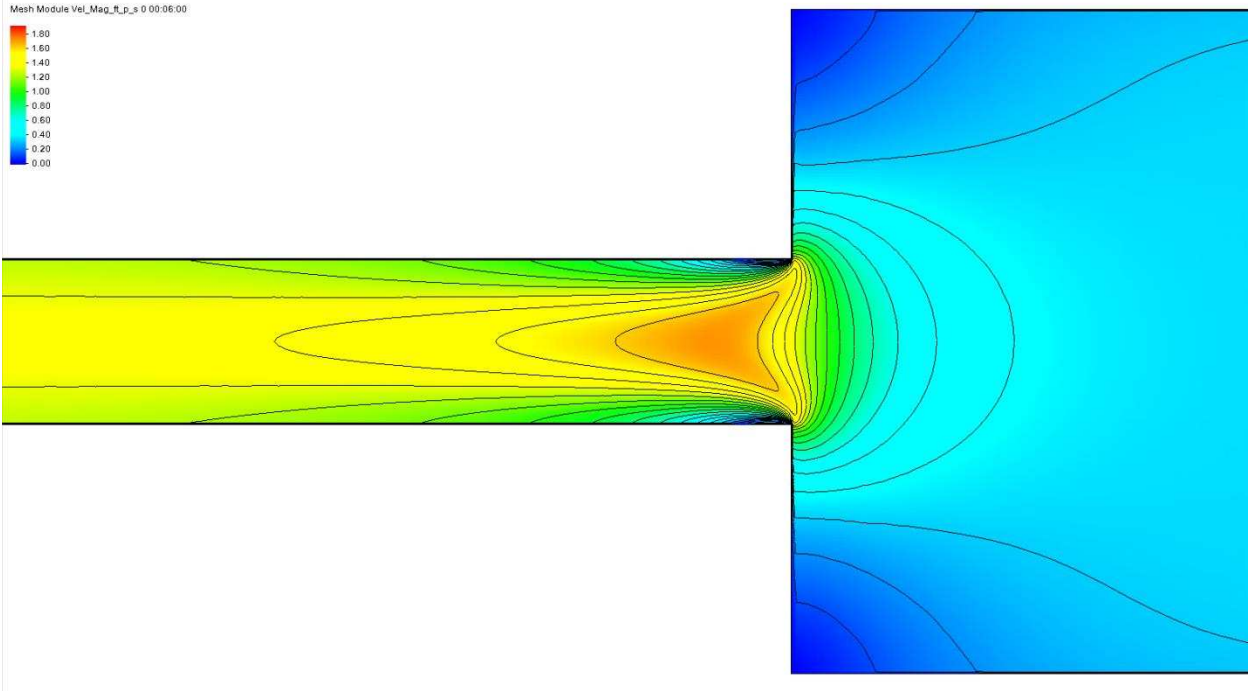
$W2/W1 = 0.75$, $W2 = 6\text{ft}$, $Q = 5\text{ cfs}$, $S = 0.0003$, $n = 0.015$, Abrupt



$W2/W1 = 0.5$, $W2 = 4\text{ft}$, $Q = 5\text{ cfs}$, $S = 0.0003$, $n = 0.015$, Abrupt

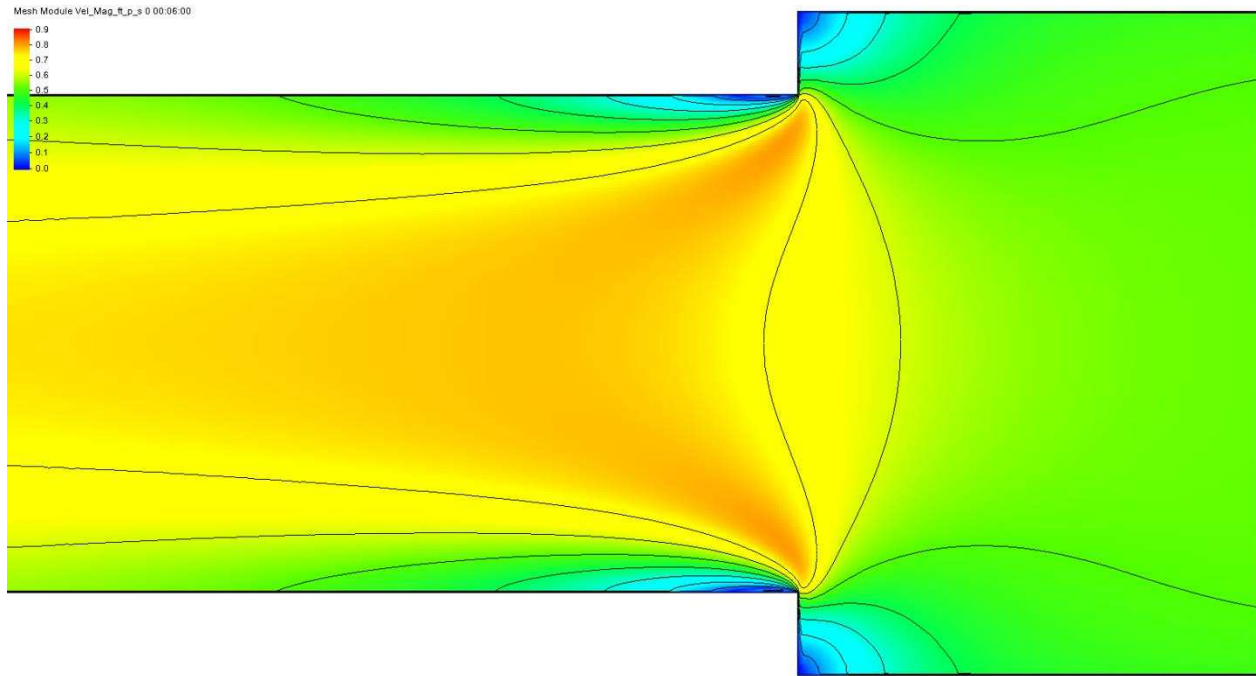


W2/W1= 0.25, W2=2 ft, Q=5 cfs, S=0.0003, n=0.015, Abrupt

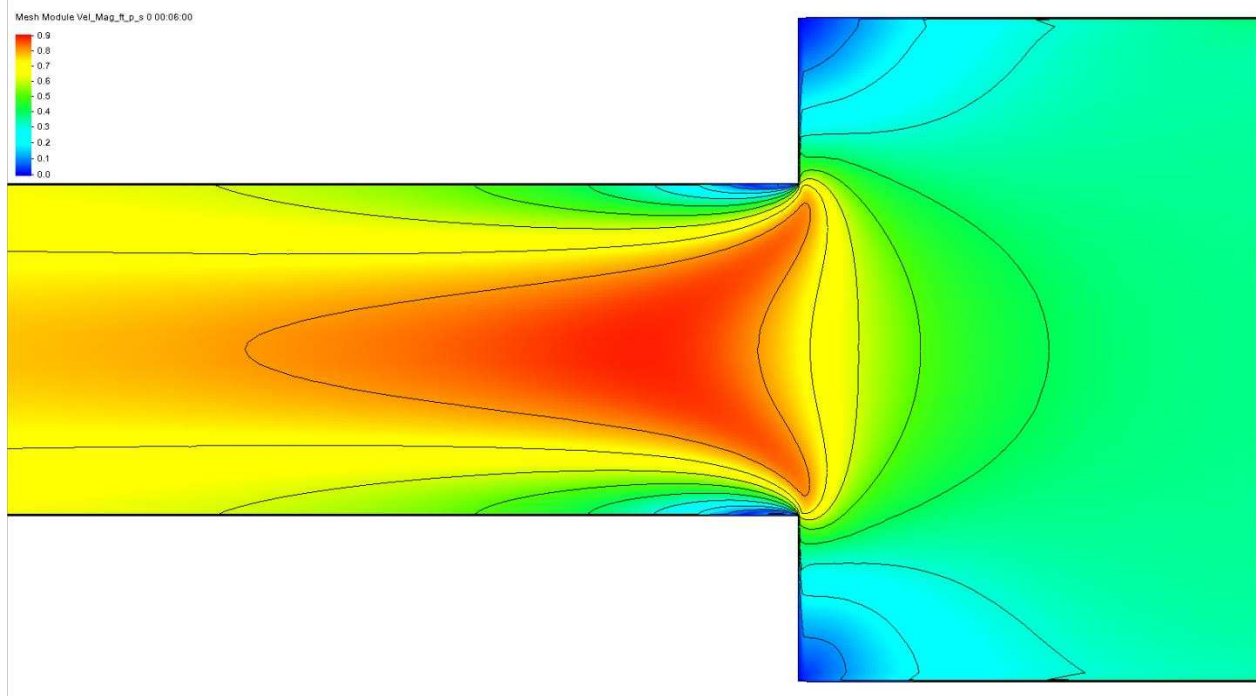


Experiment Set 3

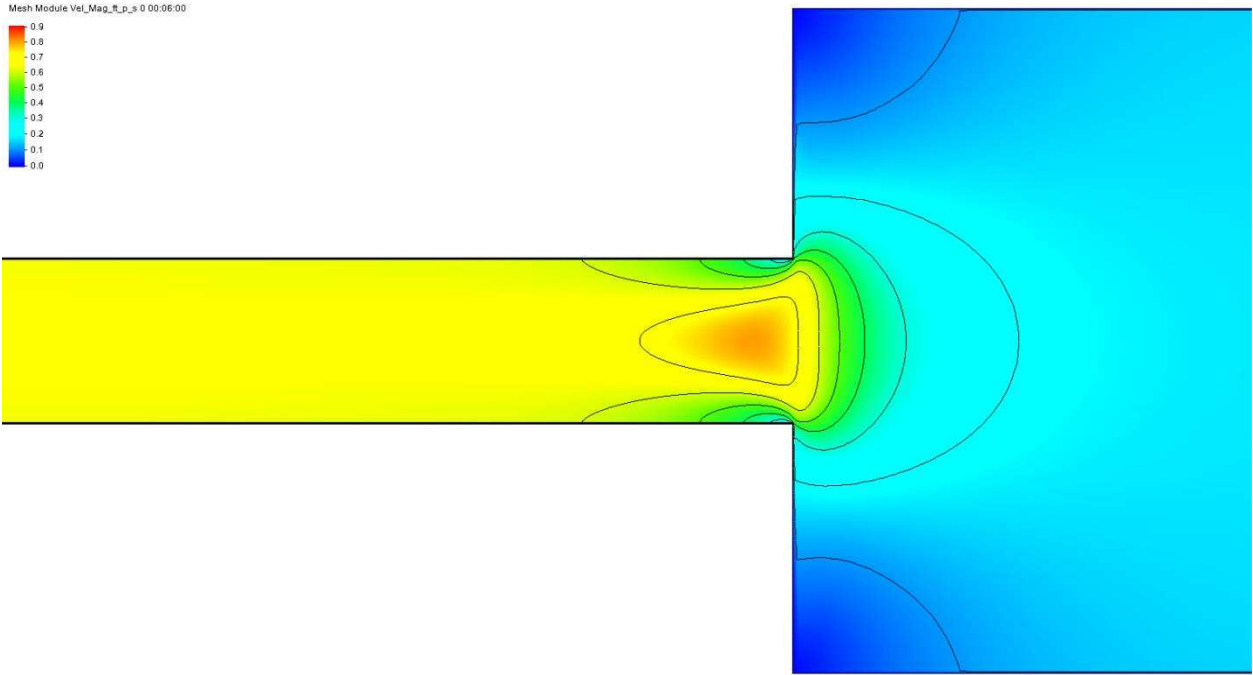
$W2/W1 = 0.75$, $W2 = 6\text{ft}$, $Q = 5\text{cfs}$, $S = 0.0003$, $n = 0.035$, Abrupt



$W2/W1 = 0.5$, $W2 = 4\text{ft}$, $Q = 5\text{cfs}$, $S = 0.0003$, $n = 0.035$, Abrupt

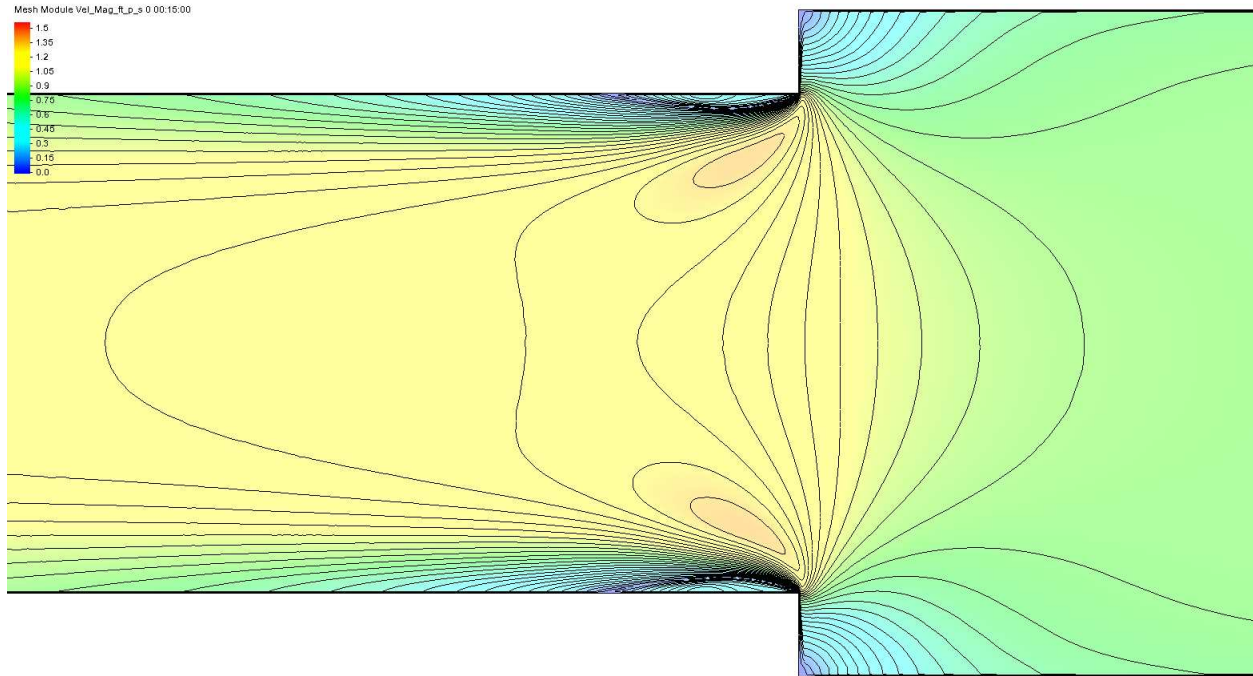


$W2/W1 = 0.25$, $W2 = 2\text{ft}$, $Q = 5\text{cfs}$, $S = 0.0003$, $n = 0.035$, Abrupt

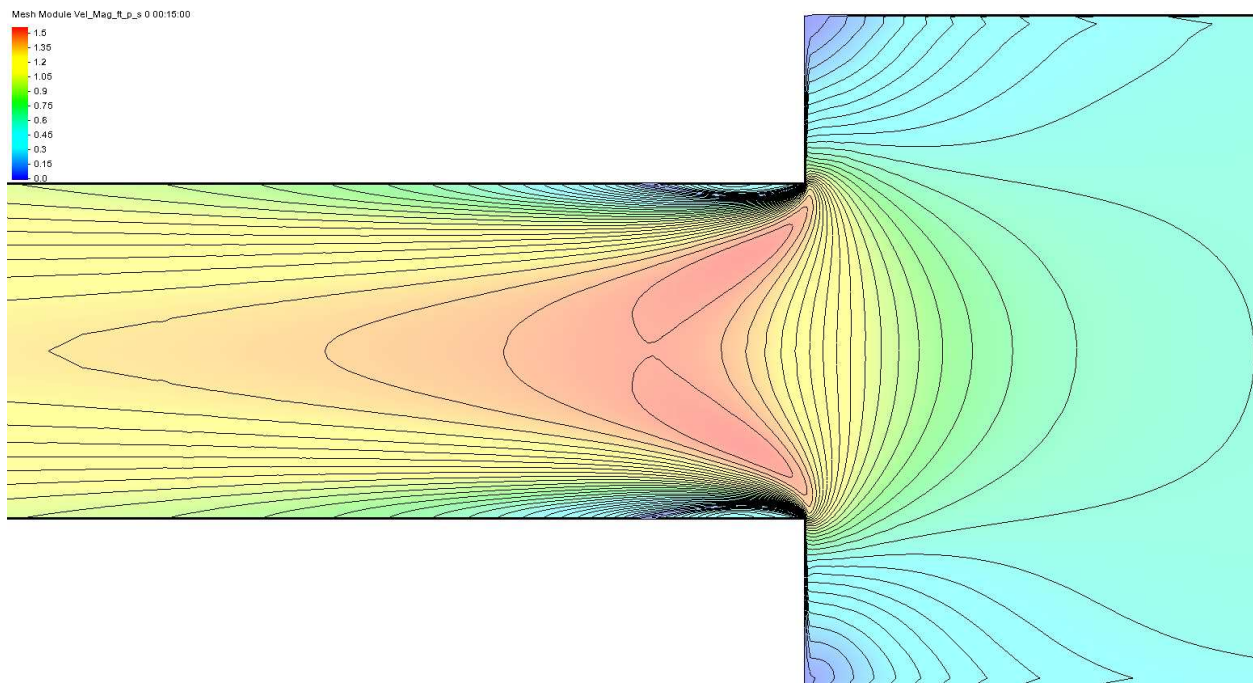


Experiment Set 4

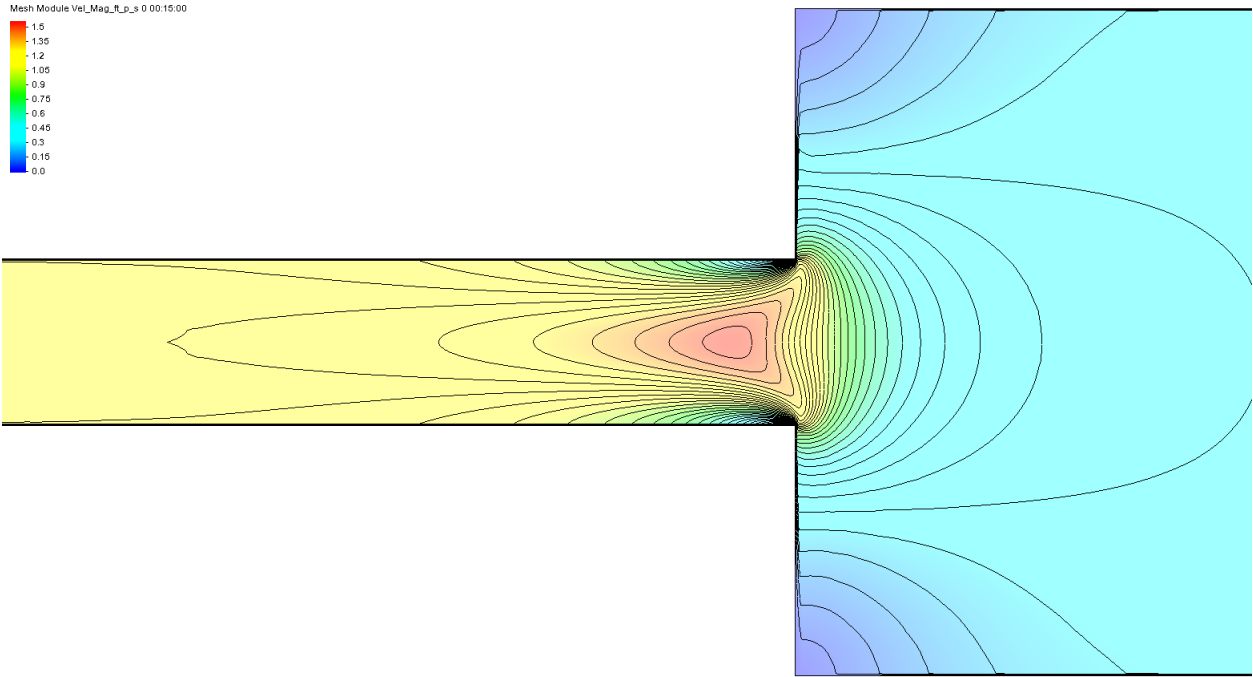
$W2/W1 = 0.75$, $W2 = 6\text{ft}$, $Q = 5\text{cfs}$, $S = 0.00065$, $n = 0.025$, Abrupt



$W2/W1 = 0.5$, $W2 = 1\text{ft}$, $Q = 5\text{cfs}$, $S = 0.00065$, $n = 0.025$, Abrupt

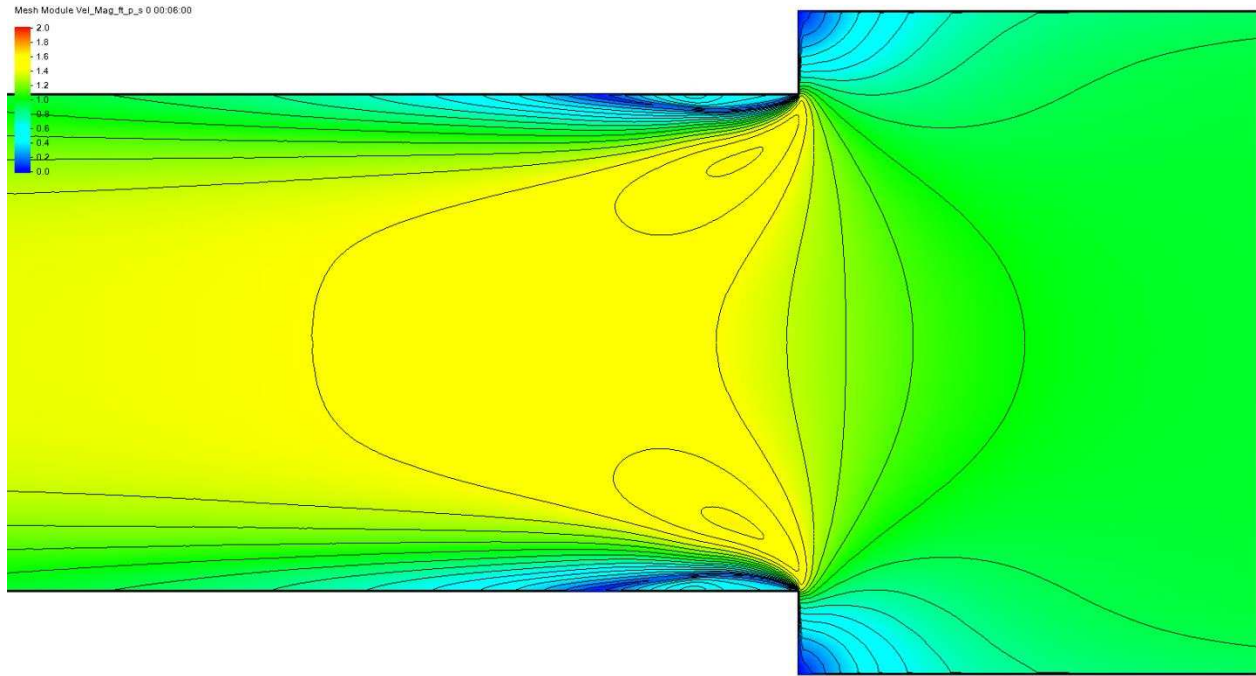


W2/W1= 0.25, W2=2ft, Q=5cfs, S=0.00065, n=0.025, Abrupt

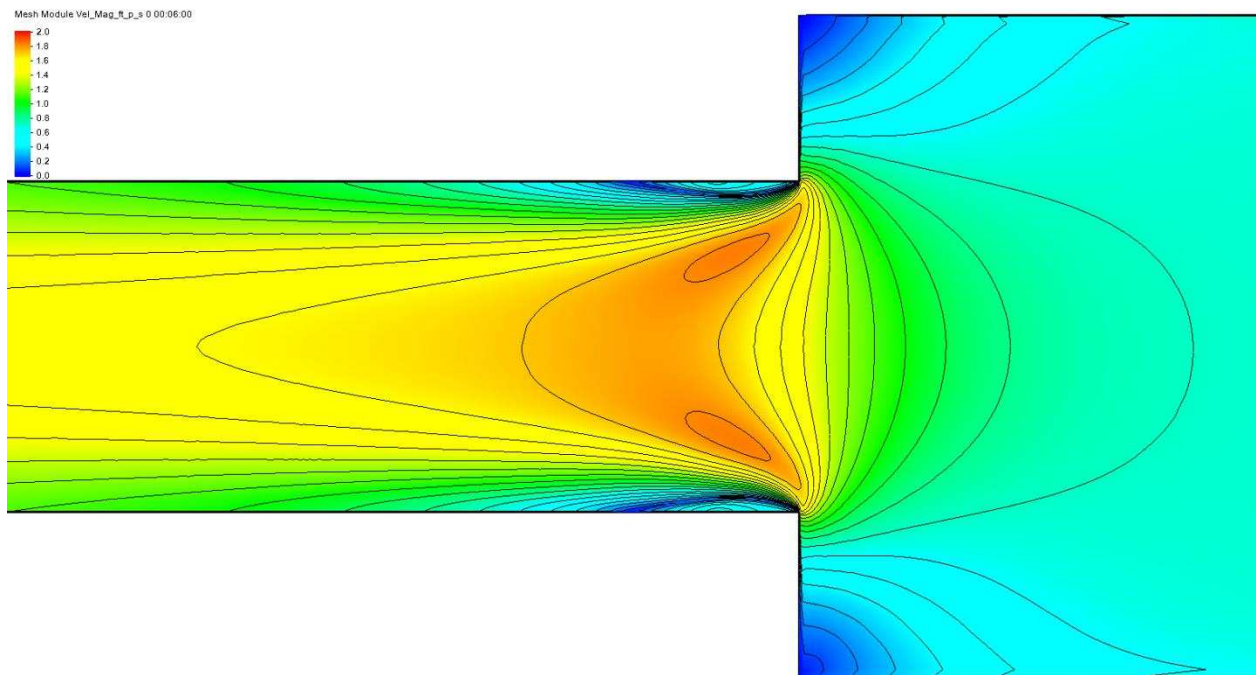


Experiment Set 5

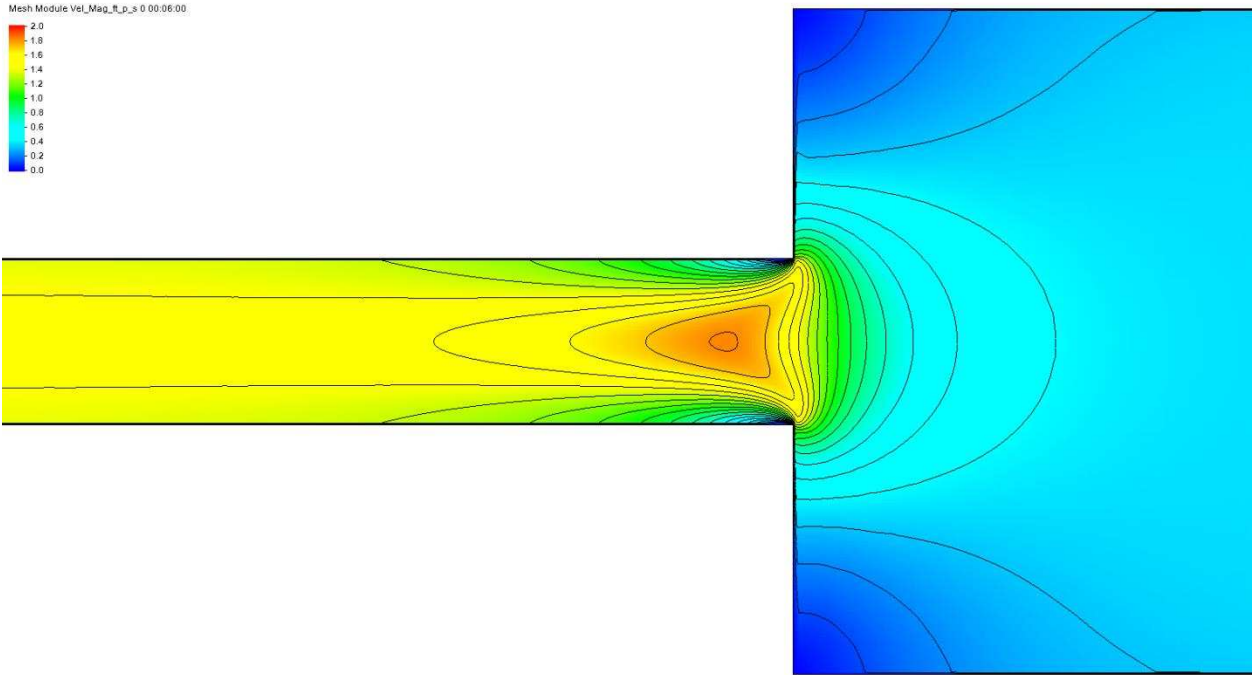
$W2/W1 = 0.75$, $W2=6\text{ft}$, $Q=5\text{cfs}$, $S=0.001$, $n=0.025$, Abrupt



$W2/W1 = 0.5$, $W2=4\text{ft}$, $Q=5\text{cfs}$, $S=0.001$, $n=0.025$, Abrupt

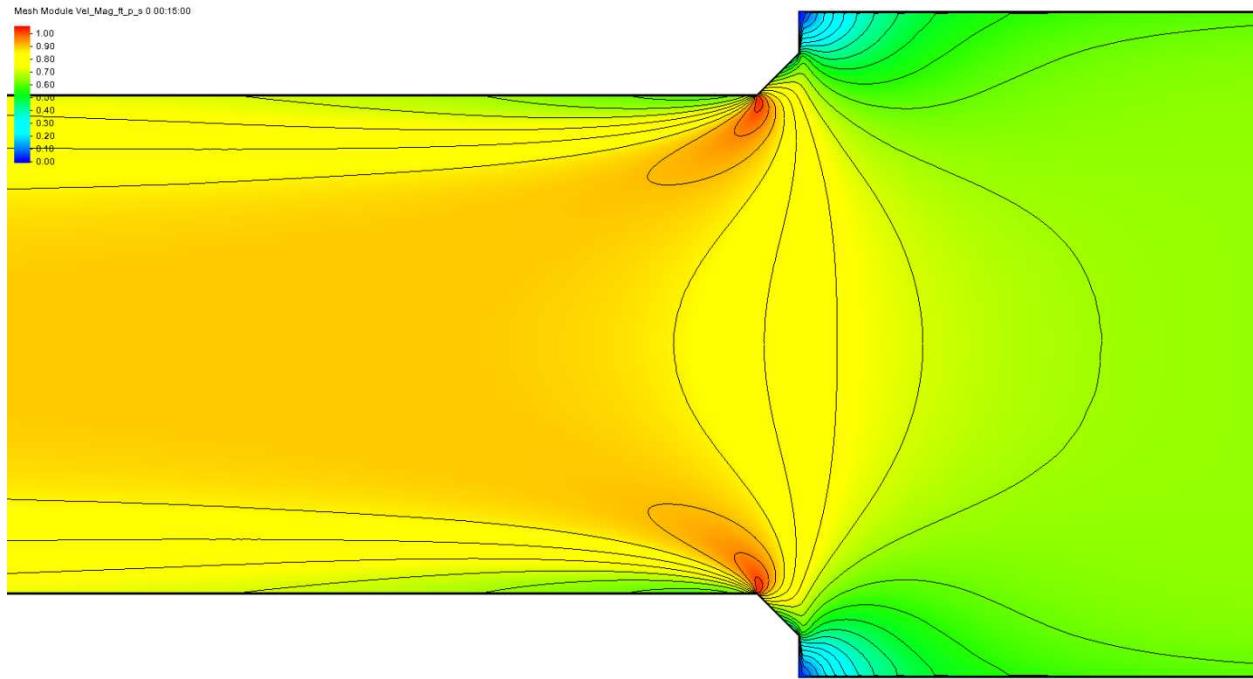


$W2/W1 = 0.25$, $W2 = 2\text{ft}$, $Q = 5\text{cfs}$, $S = 0.001$, $n = 0.025$, Abrupt

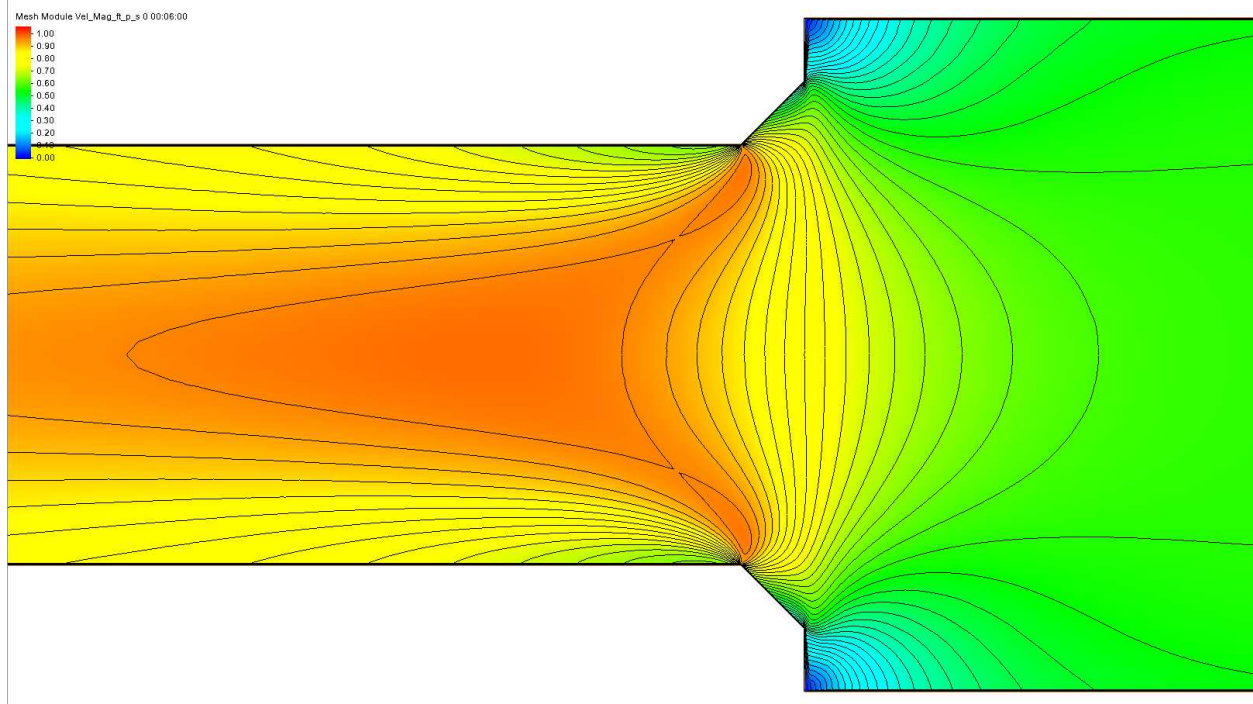


Experiment Set 6

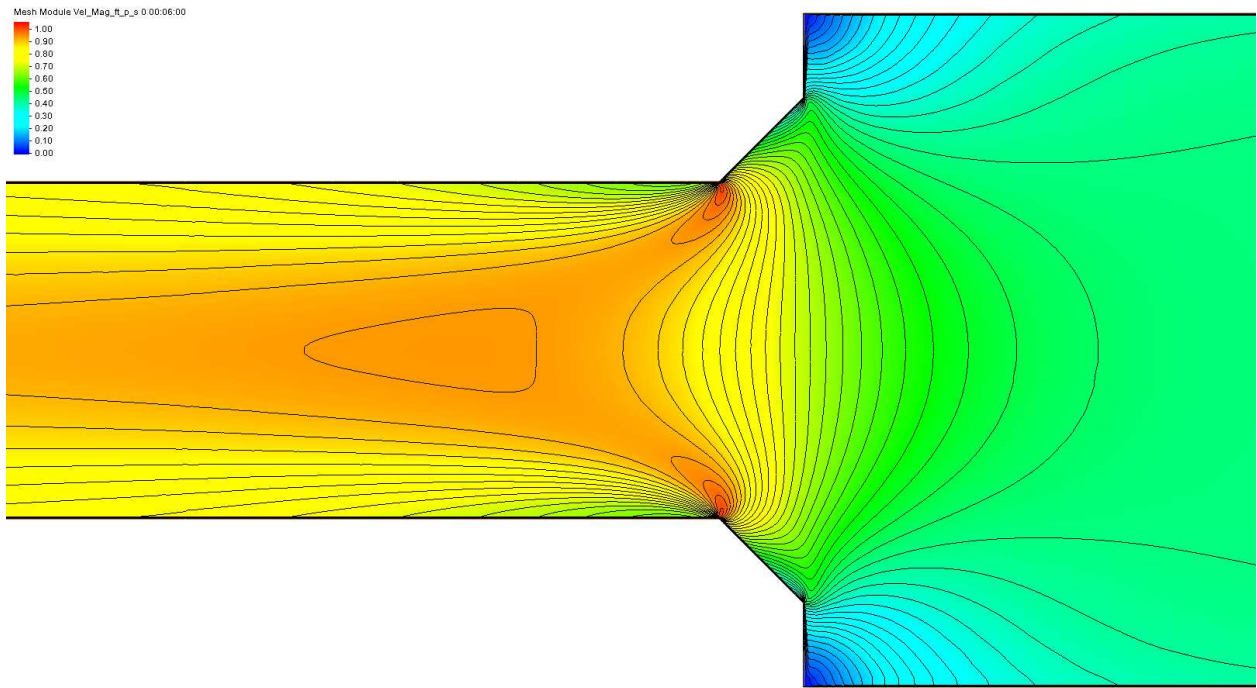
$W2/W1 = 0.75$, $W2 = 6\text{ft}$, $Q = 5\text{cfs}$, $S = 0.0003$, $n = 0.025$, 45° Half Bevel



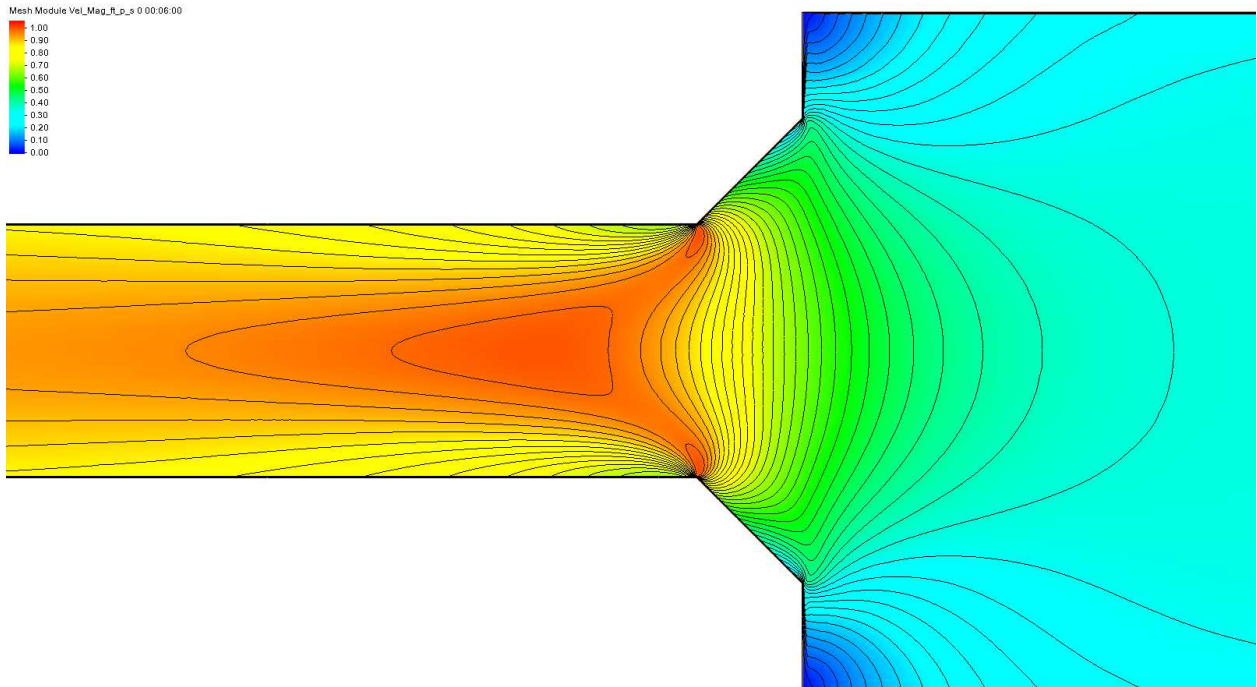
$W2/W1 = 0.625$, $W2 = 5\text{ft}$, $Q = 5\text{cfs}$, $S = 0.0003$, $n = 0.025$, 45° Half Bevel



$W2/W1 = 0.5$, $W2 = 4\text{ft}$, $Q = 5\text{cfs}$, $S = 0.0003$, $n = 0.025$, 45° Half Bevel

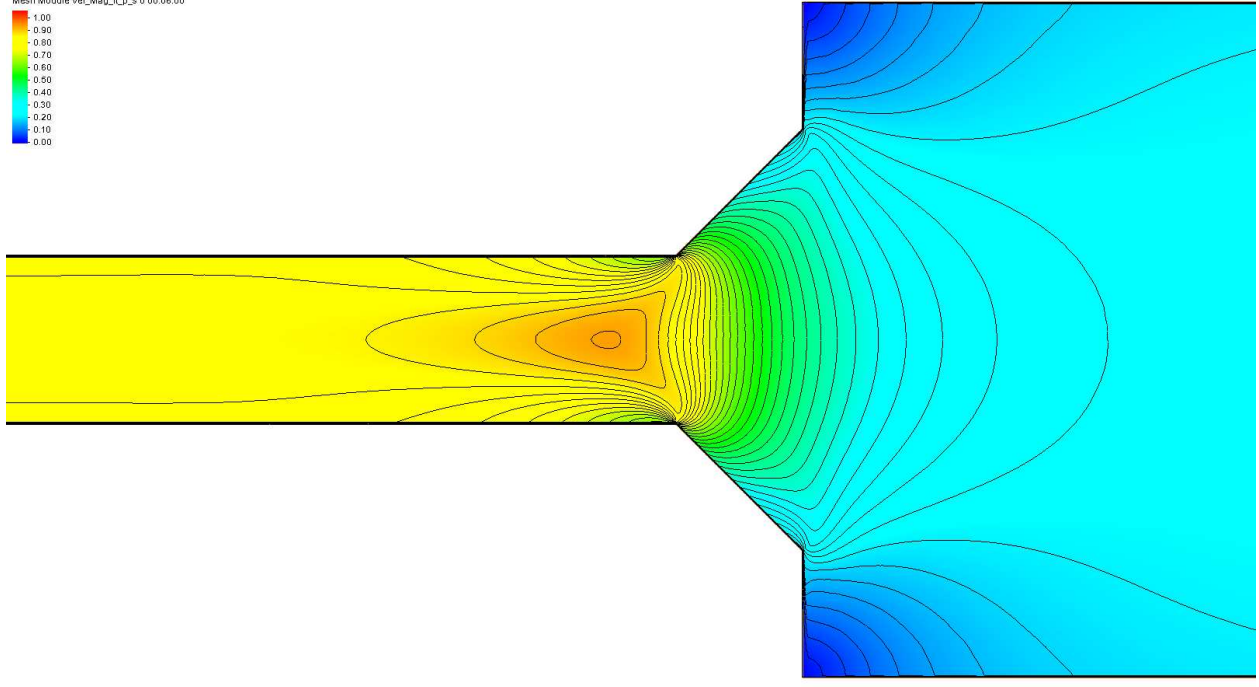
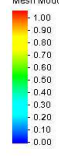


$W2/W1 = 0.375$, $W2 = 3\text{ft}$, $Q = 5\text{cfs}$, $S = 0.0003$, $n = 0.025$, 45° Half Bevel



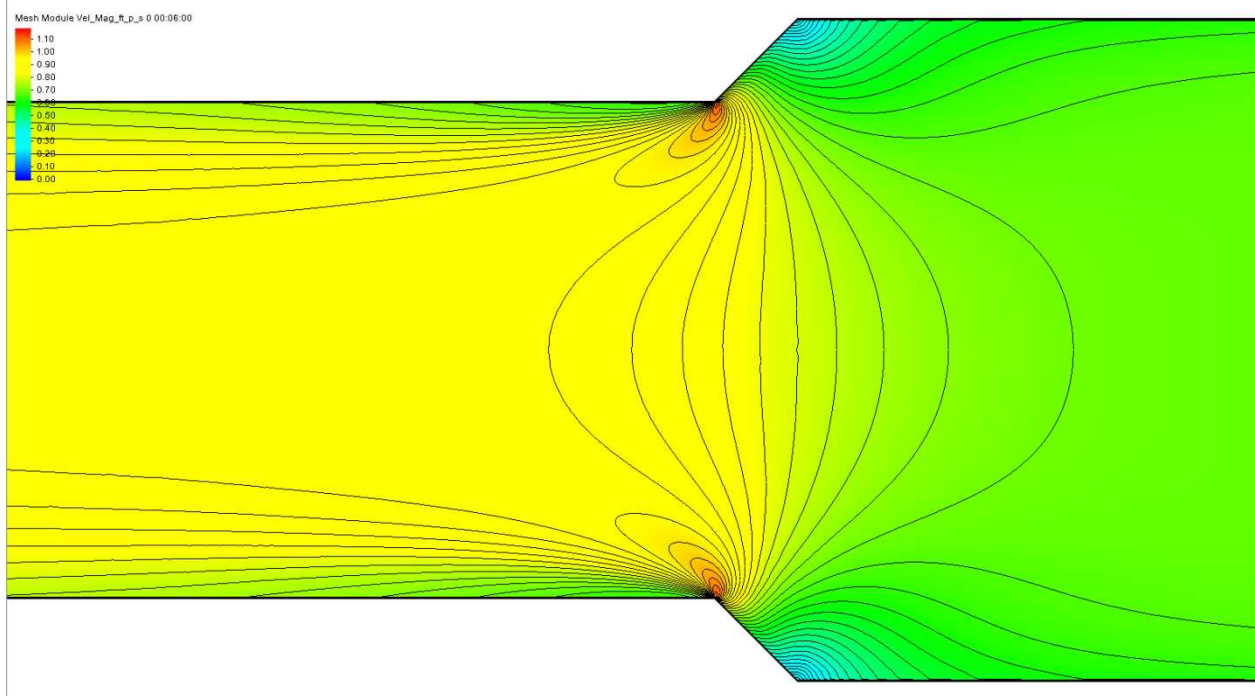
$W2/W1 = 0.25$, $W2 = 2\text{ft}$, $Q = 5\text{cfs}$, $S = 0.0003$, $n = 0.025$, 45° Half Bevel

Mesh Module Vel_Mag_R_p_s 0 00:06:00

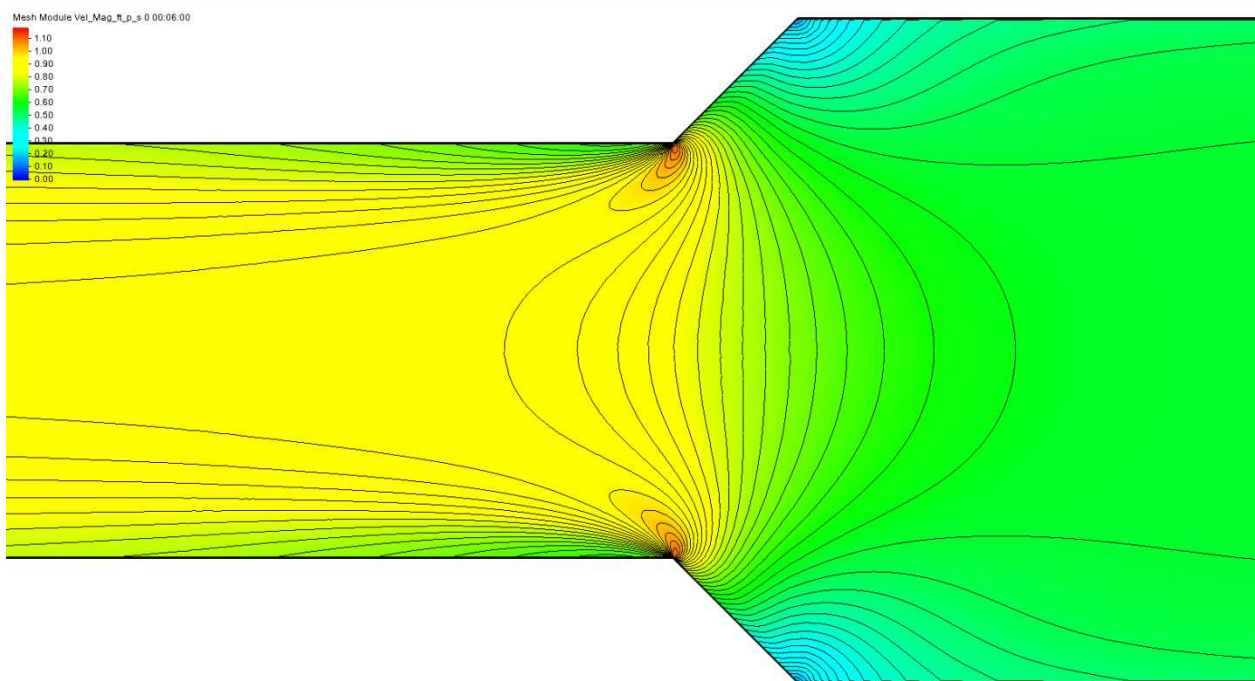


Experiment Set 7

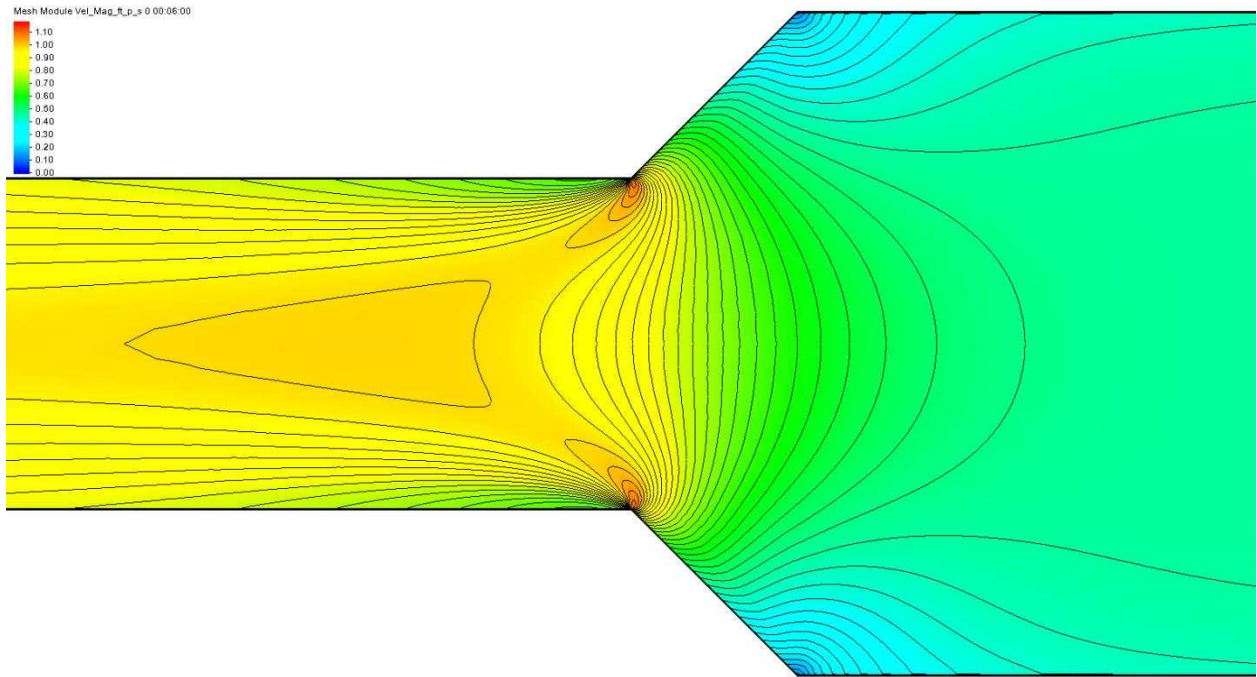
$W2/W1 = 0.75$, $W2 = 6\text{ft}$, $Q = 5\text{cfs}$, $S = 0.0003$, $n = 0.025$, 45° Full Bevel



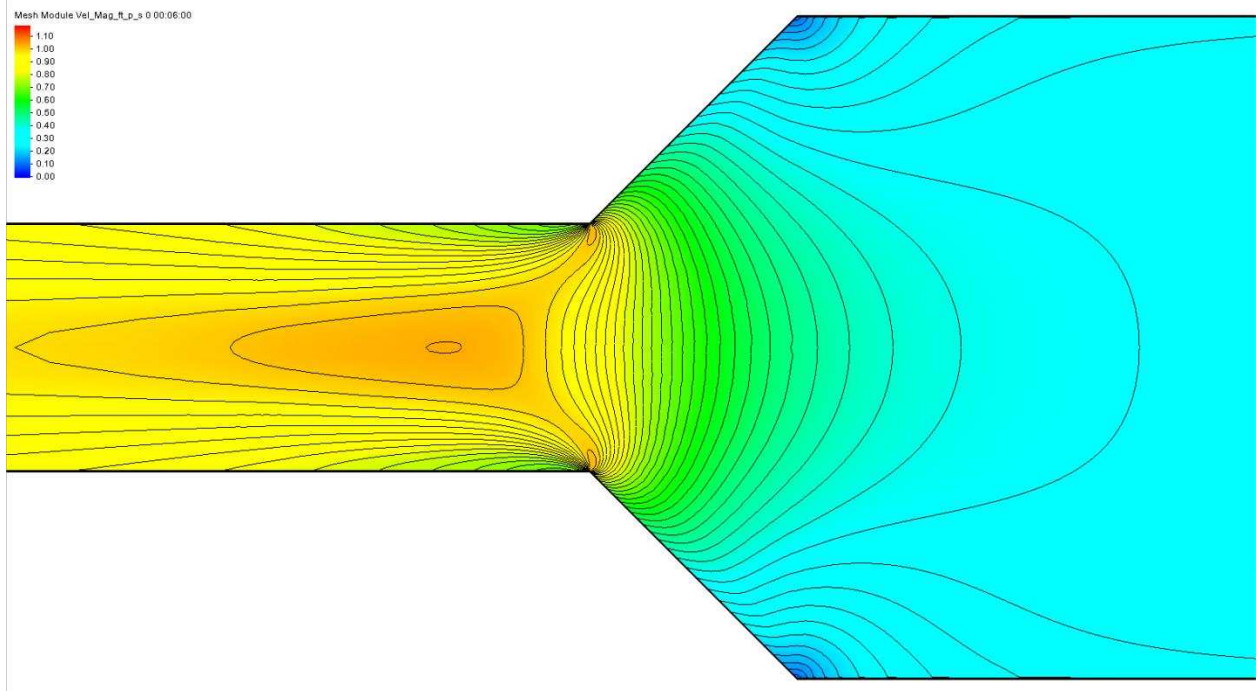
$W2/W1 = 0.625$, $W2 = 5\text{ft}$, $Q = 5\text{cfs}$, $S = 0.0003$, $n = 0.025$, 45° Full Bevel



$W2/W1 = 0.5$, $W2 = 4\text{ft}$, $Q = 5\text{cfs}$, $S = 0.0003$, $n = 0.025$, 45° Full Bevel



$W2/W1 = 0.375$, $W2 = 3\text{ft}$, $Q = 5\text{cfs}$, $S = 0.0003$, $n = 0.025$, 45° Full Bevel



W2/W1= 0.25, W2=2ft, Q=5cfs, S=0.0003, n=0.025, 45° Full Bevel

